Zeitschrift: Helvetica Physica Acta
Band: 64 (1991)
Heft: 6

Vereinsnachrichten: Frühjahrstagung der S.P.G.

Autor: [s.n.]

Helvetica Physica Acta
Vol. 64 (1991)

0018-0238/91/060890-62$1.50+0.20/0

Attenuation and Velocity Change of Ultrasonic Waves due to Thermally Assisted Flux Flow in $(La_{1-x}Sr_x)_2CuO_4$ Ceramics

Y. Horie, T. Miyazaki, T. Fukami*, T. Aomine and L. Rinderer**

Department of Physics, Kyushu University, Fukuoka 812, Japan
* On leave from Department of Physics, Kyushu University, Fukuoka 812, Japan
** Institut de Physique Expérimentale, Université de Lausanne,
CH-1015 Lausanne, Suisse

We measured the temperature T dependence of sound attenuation and sound velocity change in $(La_{1-x}Sr_x)_2CuO_4$ in magnetic fields up to 10 T. The attenuation vs T in magnetic field had a relaxation type peak just below the critical temperature T_c. Sound velocity change vs T also had a clear structure around the same temperature region. These anomalies could be ascribed to the interaction between sound waves and magnetic flux lines in thermally assisted flux flow through the crystal lattice.

Recently, there have appeared many papers which paid much attention to the unusual behaviors of flux line lattice(FLL) of high T_c superconductors in the high magnetic field H and the high temperature T region. In the region FLL seems to be seriously depinned by a large thermal excitation, because the resistive transition in high fields has a long tail, if it originates from the motion of FLL. In order to reveal the origin of such anomalous behavior of FLL, we performed ultrasonic measurements using mechanical resonance method for bulk sintered samples of $(La_{1-x}Sr_x)_2CuO_4$ (LSCO)[1].

According to Pankert's theory[2] based on the model of thermally assisted flux flow (TAFF), sound velocity $V_s(T,H)$ and attenuation coefficient $\alpha(T,H)$ of longitudinal sound waves for $\vec{H} \perp \vec{k}$ ($\vec{k}$: wave vector) can be written as follows:

$$V_s(H)^2 = V_s(0)^2 + \frac{C_{11}}{\rho}\frac{1}{1+X^2}, \quad \alpha(H) = \alpha(0) + \frac{C_{11}}{\rho\omega}\frac{X}{1+X^2}.$$

Here, $X = C_{11}\Gamma k^2/\omega$ where C_{11} is the bulk modulus of FLL, Γ is the relaxation coefficient and ω is the frequency of sound waves. ρ is the mass density of the sample. The results show a peak and a step at $X = 1$ in the plots of V_s and α vs X, respectively. For $\vec{H} \parallel \vec{k}$, however, sound waves do not couple to flux lines(FL's), and no change is expected in both $V_s(H)$ and $\alpha(H)$. Furthermore, since $C_{11}\Gamma$ can be converted to an activation energy $U(H)$ of FL's, $\Delta V_s(T,H)$ and $\Delta\alpha(T,H)$ vs T curves have a step and a peak at a relevant temperature, respectively.

As shown in Fig. 1(a) peaks are observed in $\Delta\alpha(T,H)/\alpha$ vs T curves. However, as shown in Fig. 1(b), while in the normal state an obvious difference was observed in $\Delta V_s(H)/V_s$ vs H, there observed no difference between $\vec{H} \parallel \vec{k}$ and $\vec{H} \perp \vec{k}$ in the superconducting state at 4.2 K. The fact as well as the rich structure in the low T side of the peak in $\Delta\alpha(T,H)/\alpha$ vs T curves conflicts with the results in Pankert's theory. This implies that FL's do not penetrate parallel to the applied $\vec{H}$ inside the sample in the superconducting state.

Here, we modified the theory of Pankert introducing "intrinsic pinning model" proposed by Tachiki and Takahashi[3]. The detail of the modification was given in refs. 1 and 4. Since

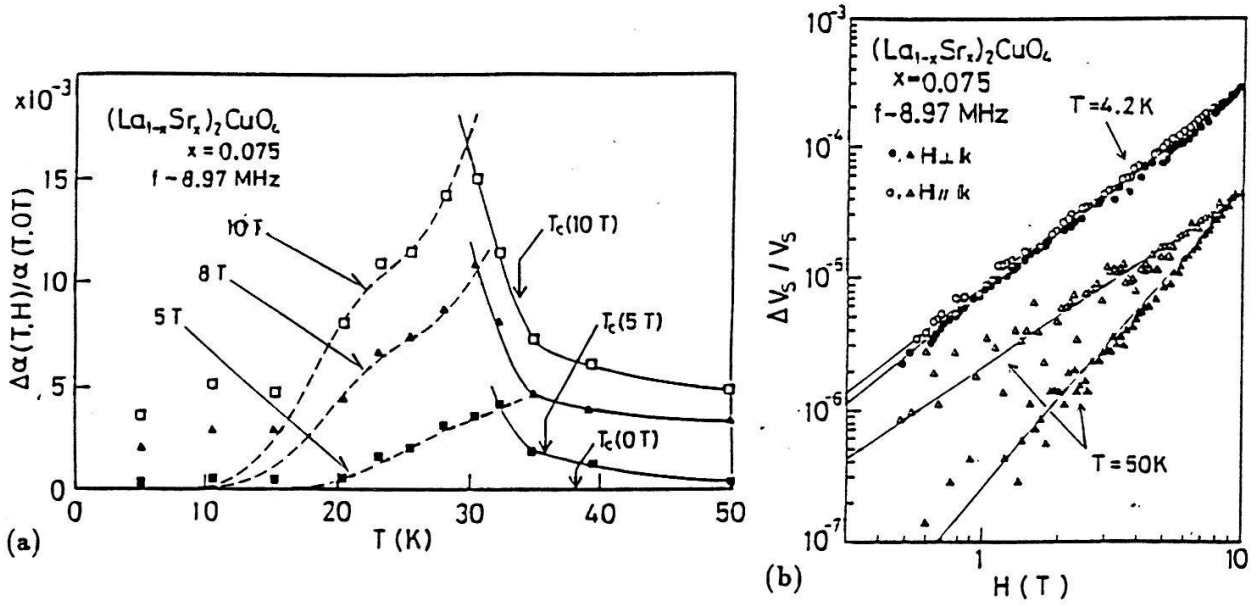

Fig.1 (a) $\Delta\alpha(T,H)/\alpha$ vs T. (b) $\Delta V_s(T,H)/V_s$ vs H for $\vec{H} \perp \vec{k}$ and $\vec{H} \parallel \vec{k}$.

the anisotropy of the coherence lengths along c-axis ξ_c and ab-plane ξ_{ab} is considerably large, and the spacing between a conducting layer [Cu-O_2 plane] and an insulating layer[La-O plane] is comparable to ξ_c, the free energy when FL's penetrate along ab-plane in the insulating layers should be lower than that when FL's cross layers straight. In such case insulating layers themselves become pinning centers. Furthermore, we take into account the anisotropy of Γ and U as Γ_{ij} and U_{ij}, respectively. Here, i and j are the direction to which $\vec{H}$ is applied and FL displaces, respectively. In the intrinsic pinning model U_{ac} should be the largest compared to U_{ab} and $U_{ca}(\sim U_{cb})$, since the energy loss due to the FL displacement is considered to be the maximum.

As shown in the figure $\Delta\alpha(T,H)/\alpha$ vs T curves show rapid decrease with increasing T just below $T_c(H)$, it should be natural to consider that the high temperature part of the contribution of U_{ij} to $\Delta\alpha(T,H)/\alpha$ is cut by the disappearance of superconductivity as shown by solid lines in the figure. This shows that FL's cannot be depinned below $T_c(H)$ for the direction associated with the largest U_{ij}, U_{ac}. This is consistent with that the tail in resistivity $\rho(T,H)$ vs T curve in LSCO is much shorter than Bi-based high T_c superconductors. Therefore, we could determine only the lowest one, U_{ca}, from the swells in the low temperature side of the observed peak as shown by dashed curves in the figure. Thus, we determined $U_{ca} = 190$ K at $H = 10$ T. Also for $V_s(T,H)$ we obtained broad step associated with TAFF. However, we could not get clear results from that, since the effect of the change in entropy is included near T_c. Not only for LSCO but also for high T_c phase Bi-Sr-Ca-Cu-O ceramics, we obtained good agreement with the modified theory[4].

References

[1] Y. Horie, T. Miyazaki and T. Fukami, *to be published in* Physica C (1991).
[2] J. Pankert, Physica C **168** (1990) 335.
[3] M. Tachiki and S. Takahashi, Solid State Commun. **70** (1989) 291; **72** (1989) 1083.
[4] Y. Horie, T. Miyazaki, T. Fukami and A. Youssef, *submitted to* Physica C .

Behaviors of Temperature and Field Dependences of Critical Current Due to Flux Motion in $Bi_2Sr_2CaCu_2O_{8+y}$ Film Prepared by Laser Ablation

Takeshi Fukami*, Takashi Yamamoto**, Yuuji Horie**, Takafumi Aomine** and Leo Rinderer
Institut de Physique Expérimentale, Université de Lausanne, CH-1015 Lausanne, Suisse
(*On leave from Department of Physics, Kyushu University, Fukuoka 812, Japan)
** Department of Physics, Kyushu University, Fukuoka 812, Japan

Abstract: We report the temperature T and magnetic field H dependences of the critical current density J_c for $Bi_2Sr_2CaCu_2O_{8+y}$ (BSCC) films with preferred c- axis orientation. $J_c(T,H)$ versus $1/T$ as a function of H showed abrupt changes below threshold temperatures $T_t(H)$ which decreased with increasing H. Non-linear current I versus voltage V characteristics disappeared around $T_t(H)$ with increasing T. The appearance of $T_t(H)$ is discussed comparing with anomalies observed in ultrasonic measurements.

As has been well known, the critical current density J_c in high T_c oxide superconductors increases as the sample quality is improved. Therefore this fact suggests that the high J_c is an intrinsic property in high T_c superconductors. Here, we report the behaviors of magnetic flux lines through the temperature T and magnetic field H dependences of J_c. The thin films of BSCC were deposited on single crystalline MgO(100) substrates by the laser ablation technique using Ar-F excimer pulse laser. Figure 1 shows J_c versus $1/T$ as a function of H for H//the c-axis. J_c at 20 K in H=0 is about 2.7×10^4 A/cm^2. For H//the basal plane and H//the c-axis, J_c versus $1/T$ curves change slowly in low temperatures, but beyond a temperature J_c decreases drastically. Here a threshold temperature $T_t(H)$ is defined as a cross point of two extrapolated lines from low and high temperatures. Since current I-voltage V characteristics have been reported for H//the basal plane [1], here we report the results for H//the c-axis. Figure 2 shows a representative I -V characteristics as a function of H at 35 K. As long as data are limited in low voltage region, log V versus log I seems

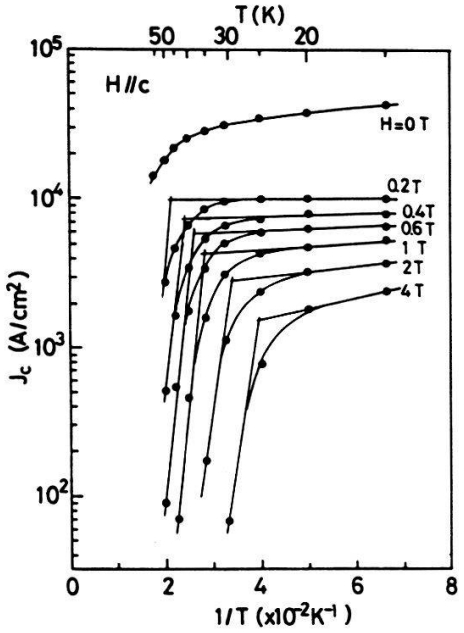

Fig. 1 J_c versus $1/T$ for H//c-axis.

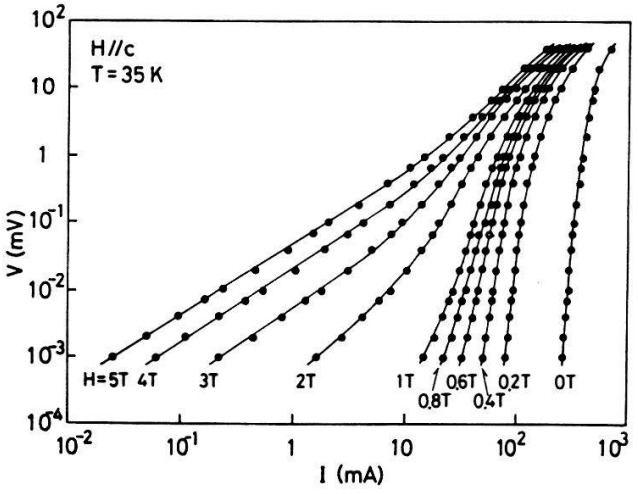

Fig. 2 I-V characteristics for H//c-axis.

linear though the slope changes as field increases. These data can be analyzed using the formula

$$V/V_0 = \{(I - I_{c0})/I_0\}^n. \qquad (1)$$

Here V_0 and I_0 are normalizing factors, and the parameters I_{c0} and n were determined so as to obtain the best fit in low voltage region, thus the plots of n versus H as a function T were obtained. Since for H//the basal plane, the linear region of log I versus log V is limited in narrow region of voltage, the ambiguity in parameters is rather large. Let us define a threshold field as $H_{n,t}(T)$ above which n=1. Figure 3 shows $T_t(H)$, $H_{n,t}(T)$ and others on a T-H plane. A boundary formed by these threshold quantities would be ascribed to the transition from rigid or quasi-rigid flux lattice to the flux flow or depinning state due to the following reasons: (1) The threshold values of $H_{n,t}(T)$ determined from n versus H plots are located near $T_t(H)$, though they shift a little in parallel to higher temperatures. Since n=1 means the linear I-V relation in the mixed state, the change from $n \neq 1$ to n=1 means a beginning of the flux flow state. (2) The threshold values determined from I_{c0} versus T are also consistent with the $T_t(H)$ line mentioned above. Since I_{c0} may be considered an intrinsic critical current, disappearance of I_{c0} can be also considered the disappearance of the rigid flux state.

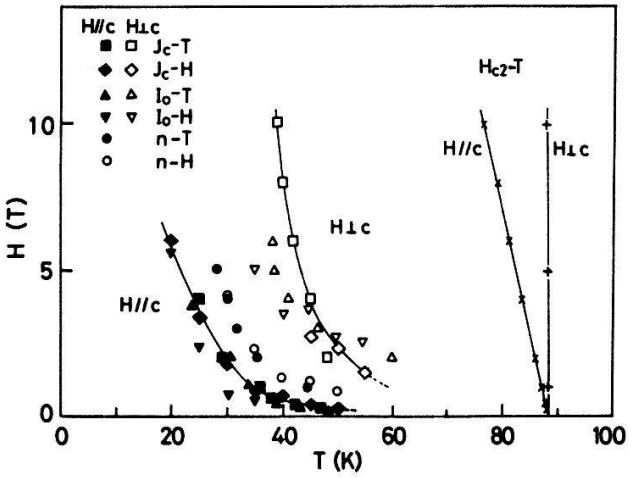

Fig. 3 T-H plots for several threshold quantities.

The depinning line determined by the solid line in Fig.3 is very similar to one obtained from the temperature dependence of the resonance frequency and the dissipation of the mechanical vibration [2]. Since the flux lines are pinned by the crystal lattice, these changes were ascribed to a state change of the flux lattice. By the way, as long as the ultrasonic measurement is carried out within a small amplitude of oscillations, the value of effective current is very small compared with one in resistance measurement. If the Lorentz force in ordinary field is too weak to release the flux lines from their pinning centers, any anomalies would not be observed in the attenuation and sound velocity near the line in Fig.3. However, a relaxation type peak in attenuation coefficient and an abrupt change in sound velocity have been observed in BSCC at about 62 K in H=0.4 T, which seems to be located on the tail of the depinning line in Fig.3 [3]. These are considered to come from a change of the interaction between the crystal and the flux lattice in the thermally assisted flux flow (TAFF) state[3]. Therefore, this result would show that the flux lines can move easily under the weak agitation because the pinning potential of flux lines from the crystal lattice is in very shallow state. In this meaning, this result is consistent with the solid line in Fig.3. But at present it is not clear whether the intermediate region between the solid line and a group of dots and circles is meaningful or not and what state is realizing in the flux lattice. The anomalies in ultrasonic measurements have been also observed near T_c in $(La_{1-x}Sr_x)_2CuO_4$ [4] and $(Bi_{0.85}Pb_{0.15})_2Sr_2Ca_2Cu_3O_{10+y}$ [5]. These were well understood in terms of TAFF.

References

[1] T. Fukami and T. Kamura: Supercon. Sci. Technol. 3 (1990) 467.
[2] P. L. Gammel, L. F. Schneemeyer, J. V. Waszczak and D. J. Bishop: Phys. Rev. Lett. **61** (1988) 1666.
[3] J. Pankert: Physica C **168** (1990) 335.
[4] Y. Horie, T. Miyazaki and T. Fukami: Physica C 175(1991) 93.
[5] Y. Horie, T. Miyazaki, T. Fukami and A.A.A. Youssef : To be published in Physica C (1991).

THERMAL PROCESS EFFECT TO $(Bi_{1-x}Pb_x)_2Sr_2Ca_2Cu_3O_{10+\delta}$ FILMS PREPARED BY RF SPUTTERING WITH COMPOUND POWDER TARGET (II).

Takeshi Fukami*, Edgar Holguin, Hiroshi Nakano** and Leo Rinderer
Institut de Physique Expérimentale, Université de Lausanne, CH-1015 Lausanne
*On leave from Department of Physics, Kyushu University, Fukuoka 812, Japan
** Department of General Education, Nagoya University, Nagoya 464-01, Japan

ABSTRACT

We have examined the effect of thermal process to $(Bi_{1-x}Pb_x)_2Sr_2Ca_2Cu_3O_{10+\delta}$ films prepared by RF sputtering with compound powder target, which was prepared only by mixing raw powders at the ratio of Bi:Pb:Sr:Ca:Cu=2:1:2:2:3. The process temperature and time are very important. We could obtain films containing 110 K phase more than 90% by processing together with a sintered bulk sample of the bismuth system with x = 0.2 for 10 h at 860±1C.

1. INTRODUCTION

Three distinct superconducting phases may coexist in bulk ceramics of the Bi-Sr-Ca-Cu-O system. Phase 1 is the original 20 K phase discovered by Michel et al* and has the composition $Bi_2Sr_2CuO_y$. With the addition of calcium its Tc raises to over 100 K, but two new different superconducting phases are formed. Phase 2 has the composition $Bi_2Sr_2CaCu_2O_y$ with a T_c ~ 80 K. Finally, phase 3 has the composition $Bi_2Sr_2Ca_2Cu_3O_y$ and is expected to have a T_c ~ 110 K.

We report here the results of a study of the d.c. electrical resistivity R and critical current J_c of Pb-substituted films from the Bi-Sr-Ca-Cu-O system. The films of a few μm thickness were prepared by R.F. sputtering. X-ray powder diffraction was used for the determination of the ratio 110 K - phase to 80 K - phase.

2. SAMPLE PREPARATION

The target was prepared only by mixing raw powders at the ratio of Bi:Pb:Sr:Ca:Cu=2:1:2:2:3. The films prepared by R.F. sputtering were deposited in 0.1 mtorr Ar atmosphere on MgO single crystals kept at 600°C, and then thermally processed together with a sintered ceramic of nominal composition $Bi_{1.6}\ Pb_{0.4}\ Sr_2Ca_2Cu_3O_{10+\delta}$ during several hours. The ceramics used for the annealing of films were obtained by solid-state reaction using powders of Bi_2O_3, $CaCO_3$, PbO, $SrCO_3$ and CuO with a purity better than 99.9 %.

* *C. Michel, M. Hervieu, M.M. Borel, A. Grandin, F. Deslandes, J. Provost and B. Raveau, Z. Phys. B68, 412 (1987).*

3. RESULTS, DISCUSSION AND CONCLUSION

The temperature dependences of R and J_c were measured using a four-probe method. Contact leads were made with gold wires bonded to the surface of the film with a conductive silver paste. The figure shows the normalized R/R_{max} versus temperature curves made from room temperature to the offset of the transition using a slow cooling rate. These curves are very sensitive to the thermal process temperature and follow the usual linear trend down to the onset of the temperature transition, which is close to 120 K for all the films. In general, the lower part of the curves presents the two steps corresponding to the 110 K and 80 K superconducting phases and a typical "tail" which prevents the resistivity from dropping to zero, as we would have obtained by extrapolating the rest of the curve. However, a narrow superconducting transition at the maximum T_c (offset) - 103 K is observed when T = 860°C and the annealing time is around 10h. The ratio of the 110 K-phase to 80 K-phase estimated from the intensities of the (002)-lines in the corresponding X-ray powder diffractogram is roughly 9:1. The J_c curve of this sample (see insert) can be fitted between the functions $(1-T/T_c)^{1/2}$ and $(1-T/T_c)$.

Annealing temperature

dependence of Bi 110K

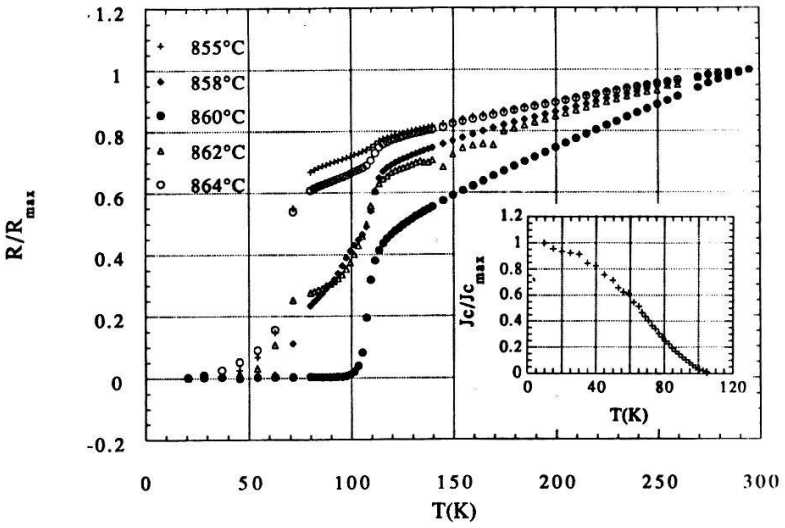

The results show that the loss of the initial Pb concentration in the film during the annealing can be compensated by the sintered ceramic. This element increases and stabilizes the 110 K phase.

ACKNOWLEDGEMENTS - The authors wish to thank Dr. K. Schenk, V. Soares and H. Castro, and M. Ede for their assistance with the X-ray powder diffractometer, computer and typing the manuscript, respectively. The work has been financially supported by the Swiss National Science Foundation.

Temperature Dependence of Activation Energy in Flux Creep in High T_c Oxide Superconductors

Takeshi Fukami*, Vitorvani Soares and Leo Rinderer

Institut de Physique Expérimentale, Université de Lausanne,
CH-1015 Lausanne, Suisse
(* On leave from Department of Physics, Kyushu University, Fukuoka 812, Japan)

Abstract: *The temperature dependence of the activation energy of magnetic flux lines from pinning centers was estimated using the intrinsic pinning model by Tachiki and Takahashi. We could obtain good coincidence between the estimation and experimental values using reasonable parameters obtained by experiments. The temperature dependence of activation energy is dependent mainly on the relative size of the coherence length to the inter-distance between CuO_2 conduction planes.*

The wide resistive transition of oxide superconductors in magnetic field H is a serious problem for practical applications, but its wide transition and anisotropy are physically interesting subjects. For $Bi_2Sr_2CaCu_2O_{8+y}$ (BSCC) films with the c-axis orientation prepared by the laser ablation technique using Ar-F excimer laser, the temperature dependence of resistivity $\rho(T)$ was measured as a function of H [1,2]. For these films, a strong anisotropy was observed between $\boldsymbol{H}$//c-axis and $\boldsymbol{H}$//the basal plane. Namely, the width for H//c-axis is wider than that in H//the basal plane. The beginning of abrupt dropping of $\rho(T)$ versus T curves, however, seems not to shift with increasing H for both cases of $\boldsymbol{H}$// c-axis and $\boldsymbol{H}$ //the basal plane. These curves have been analyzed using the formula

$$\rho(T,H) = \rho(0) \exp[-U_0(H)(1-t)^n/k_BT]. \qquad (1)$$

Here, $U_0(H)$, t and n are an activation energy at T=0 K, the reduced temperature $t=T/T_c(H)$ with a critical temperature $T_c(H)$ and a constant exponent, respectively. Generally, $\rho(0)$, $U_0(H)$, $T_c(H)$ and n should be determined so as to obtain the best fit to experimental results. This formula can be deduced by approximating the Anderson-Kim formula on the basis of flux creep model [3]. The best fits were obtained for n=1 and the field dependence of $U_0(H)$ were obtained for $\boldsymbol{H}$//c-axis and $\boldsymbol{H}$ // the basal plane [2].

Similarly, for $(Nd_{1-x}Ce_x)_2CuO_4$ (NCC) films, Suzuki and Hikita measured the temperature dependence of the resistivity in magnetic field and obtained n=3 for $\boldsymbol{H}$//c-axis and n=2 for $\boldsymbol{H}$// the basal plane [4]. For $YBa_2Cu_3O_{7-\delta}$ (YBC), there are many investigations concerning the flux creep, and, generally, the exponent obtained is n=1.5. Thus, for many investigations $\log[\rho(T,H)]$ versus $U_0(H)(1-t)^n/T$ had good linearity but the values of the exponent were different for each compound. These experiments have been done under the condition of the current vector $\boldsymbol{J}$ perpendicular to $\boldsymbol{H}$, which produce the Lorentz force JB on the magnetic flux lines in the mixed state. Therefore, Anderson-Kim theory can be adopted and the above analyses for the experimental results are reasonable.

Here, limiting the analysis only for $\boldsymbol{H}$//the basal plane we estimate the exponent in terms of the intrinsic pinning model for flux pinning given by Tachiki and Takahashi [5,6] and we explain the difference of the values of the exponent n for the different oxide superconductors.

According to Tachiki and Takahashi, the potential energy for one flux line trapped in a layer parallel to the basal plane of the high T_c oxide superconductor can be represented by

$$U(z_0)=(H_c^2/4\pi) \int dxdz[1+\delta\cos(2\pi z/a_c)]^2 \operatorname{sech}^2[(x/\xi_{ab})^2+\{(z-z_0)/\xi_c\}^2]^{1/2}. \qquad (2)$$

Here $H_c(T)$ is the thermodynamic critical field, δ a parameter which represents an amplitude of the spatial variation of the order parameter along the c-axis, a_c the inter-distance between CuO_2 conduction planes, $\xi_{ab}(T)$ and $\xi_c(T)$ the coherence lengths for the cases of $\boldsymbol{H}$//c-axis and

H//the basal plane, respectively. Furthermore, it is assumed that the magnetic flux line exists along *y*-axis at $(0,0,z_0)$. The important value here is the potential difference $\Delta U(T)$ between the top of the potential and its valley. Thus we take the difference between the potential at CuO_2 plane and the insulating plane which is taken at the intermediate point between CuO_2 planes. Parameters for calculation were found from experimental data. Figure 1 shows $\log[4\pi\Delta U(T)/H^2_c(0)]$ versus $\log[1-t]$ as a function of $\xi_c(0)$ for BSCC with δ=0.6. Figure 2 shows the $\log[4\pi\Delta U(T)/H^2_c(0)]$ versus $\log[1-t]$ for BSCC ($\xi_c(0)/a_c$ =0.065), YBC ($\xi_c(0)/a_c$ = 0.21) and NCC ($\xi_c(0)/a_c$=0.38) with δ=0.6. From these calculations, we can obtain the following results;

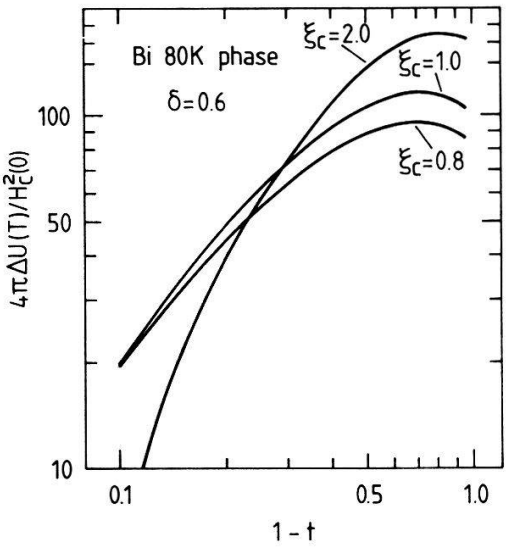

Fig.1 Temperature dependence of $\Delta U(T)$ as a function of $\xi_c(0)$.

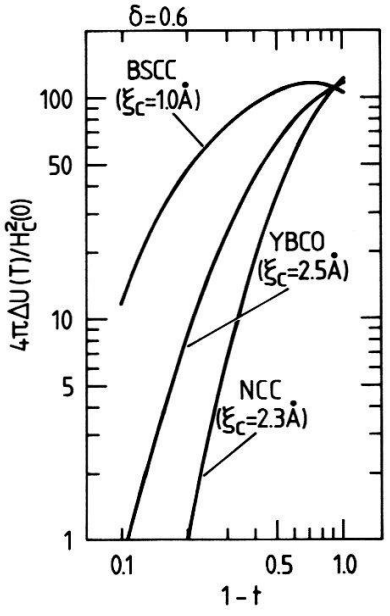

Fig. 2 Temperature dependence of $\Delta U(T)$ for BSCC, YBC and NCC.

(1) Although log $[\Delta U(T)]$ versus log $[1-t]$ curves are not linear, they seem to have n=1 for BSCC with $\xi_c(0)$=1.0 Å at the intermediate region between t=0.1 and t =0.7 which is the same as the experimental one.

(2) The slope becomes weaker as the $\xi_c(0)$ decreases for BSCC. But it seems difficult to reproduce the value of n=0 obtained for a single crystalline BSCC by Palstra et al.[7].

(3) The exponent is scarcely dependent on δ, which affects the absolute value of $\Delta U(T)$.

(4) We can explain the different values of n depending on $\xi_c(0)/a_c$ within the reasonable parameters obtained from experiments.

References

[1] T. Fukami, T. Kamura, A.A.A.Youssef, Y. Horie and S. Mase: Physica C **159** (1989) 422.
[2] T. Fukami, T. Kamura, A.A.A.Youssef, Y. Horie and S. Mase: Physica C **160** (1989) 391.
[3] P. W. Anderson and Y. B. Kim: Rev. Mod. Phys. **36** (1964) 39.
[4] M. Suzuki and M. Hikita: Phys. Rev. **B 41** (1990) 9566.
[5] M. Tachiki and S.Takahashi: Solid State Commun. **70** (1989) 291.
[6] M. Tachiki and S.Takahashi: Solid State Commun. **70** (1989) 1083.
[7] T. T. M. Palstra, B, Batlogg, L. F. Schneemeyer and J. V. Waszczak: Phys. Rev.Lett. **61**(1988) 1662.

ELASTIC PROPERTIES OF PuTe SINGLE CRYSTALS AND $NiSi_2$ FILMS DETERMINED BY BRILLOUIN SCATTERING

M.MENDIK, H.v.KÄNEL, P.WACHTER, Lab. für Festkörperphysik,ETHZ,8093 Zürich

Abstract

Surface acoustic waves (SAW's) on single crystals PuTe(100) and $NiSi_2$ films grown on Si(111) are investigated by Brillouin scattering (BS). The angular dependence of the SAW velocity (angular dispersion) was measured and used to determine Poisson's ratio.

Introduction

The existence of a surface causes interference of shear and compressional bulk waves at the crystal–air interface and is therefore the origin of SAW's. These corrugations, propagating at the surface, are the dominating mechanism for light scattering in opaque media. In contrast to the conventional ultrasonic techniques BS allows contactless measurements and samples excitations in the GHz range which permits investigations of ultrathin films. The angular dispersion of SAW's on cubic crystals has been used to compute the whole elastic tensor [1] and to derive Poisson's ratio.

Experimental

Since the development of the (3+3) tandem interferometer by Sandercock [2], BS has become a versatile tool to determine the elastic and magnetic properties of single crystals and thin films. We used the TM polarized λ=514 nm line of an Ar laser as the excitation radiation source with an incident power of 20–60 mW. The backscattered light was analyzed by a (3+3) tandem interferometer. By varying the incident angle θ it is possible to control the length of the phonon k vector whereas rotating the sample around the normal (θ fixed at 70°) permits to select the direction of the SAW momentum in the sample plane. $NiSi_2$ films (thicknesses h=1100Å,7000Å) have been grown on Si(111) by MBE [3] and retain the symmetry of the substrate. For h=7000Å the SAW's on $NiSi_2$ are completely decoupled from the substrate and sample the layer material alone. The synthesis of the Pu monochalcogenides (PuX, X=Te,Se,S) is described in [4]. In order to obtain the whole elastic tensor we applied the Levenberg–Marquardt procedure to perform a least squares fit of the measured phase velocities.

Measurements

PuTe(100): The interest in the elastic properties of the rocksalt structure Pu chalcogenides is based on the question whether they are intermediate valent [5]. Typical features for intermediate valency are a soft bulk modulus, a negative Poisson's ratio and a negative C_{12}. This indicates a shrinking of the whole crystal in all directions on application of uniaxial pressure. The angular dispersion of the SAW's of PuTe(100), measured from [001] (Fig.1), shows an elastically isotropic behavior which restricts the anisotropy constant η ($= 2C_{44}/(C_{11}-C_{12})$): $\eta \leq 1$ [6] (measurement error: 1–2.5%). Using the fitting procedure described above we obtained the elastic constants (ρ=10.2 gr/ccm) and derived thus Poisson's ratio ν=–0.11±(0.04) which tends to be negative.

Fig.1

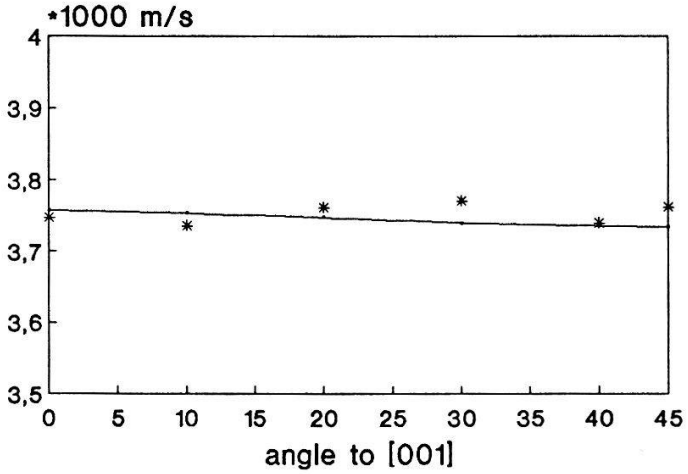

$NiSi_2(111)$: The crystal structure of $NiSi_2$ is the cubic fluorite, with a lattice constant of 5.41Å. Fig.2 shows the angular dispersion of $NiSi_2(111)$ (h=7000Å) which is anisotropic. The angle is measured from [110] (measurement error: 1%). In contrast to the (100) oriented surface we have computed two different sets of elastic constants which describe the experimental results reasonably well. With ρ= 4.81gr/ccm we obtained ν=0.42±(0.02).

Fig.2

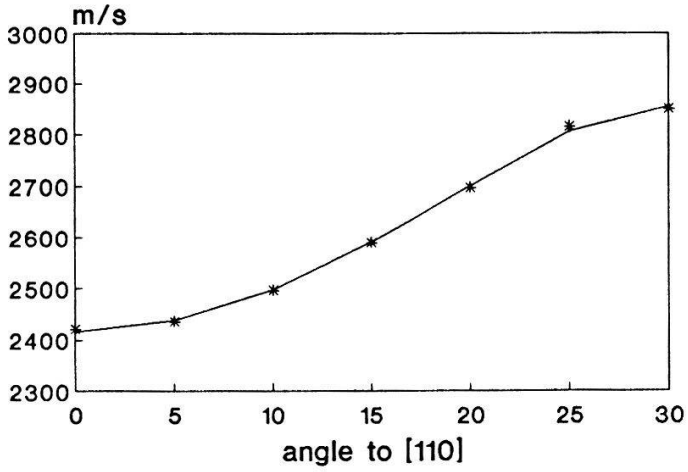

References

[1] M.W.Elmiger,Surface and Interface Analysis,14,18(1982)
[2] J.R.Sandercock in"Light Scattering in solids II",p.173,Springer(1982)
[3] H.von Känel,T.Graf,J.Henz,M.Ospelt and P.Wachter,J.Cryst.Growth,81,470(1987)
[4] J.C.Spirlet and O.Vogt,"Handbook on the physics and chemistry of the actinides",eds.A.J.Freeman,G.H.Lander,Elsevier Science Publ.BV,(1984),p.79–151
[5] P.Wachter,F.Marabelli,B.Bucher,Phys.Rev.B,in print
[6] G.W.Farnell in"Physical Acoustics", VI,p.109;Ed.: Mason,Academic Press (1970)

Adsorption of Homocysteine on Titanium Surfaces

Martin Schmidt
Université de Lausanne, Institut de physique expérimentale, CH- 1015 Lausanne

Cells can adhere on surfaces of medical devices made of titanium or Ti alloys; this is due to adsorption of organic molecules. For a better understanding of this process, adsorption of amino acids from aqueous solutions on Ti was monitored by XPS. The results for homocysteine are discussed. The adsorption process is interpreted as ligand exchange reaction.

As a consequence of biocompatibility of medical titanium devices, soft tissue can adhere strongly to the surface. Especially for medical applications it is desirable to know the type of interaction between implant surface and organism. Amino acids therefore were chosen as model substances for controlled adsorption experiments because they are building blocks of many organic structures and determine their interfacial properties.

In contact with air or water Ti forms an amphoteric oxide layer by hydroxylation as shown schematically in fig. 1a. The hydrogen of the acidic OH group is exchangeable for cations at pH>6, the basic OH is exchangeable for anions at pH<6 [1]. The ionic properties of amino acids also are pH dependent. They form zwitterions: the carboxylic group is deprotonated at pH>2, the amino group protonated at pH<9 [2]. Thus for both the TiO_2 surface and the amino acid, the pH at which adsorption from an aqueous solution occurs leads to conclusions as to what group can be involved in the adsorption reactions.

Fig. 1

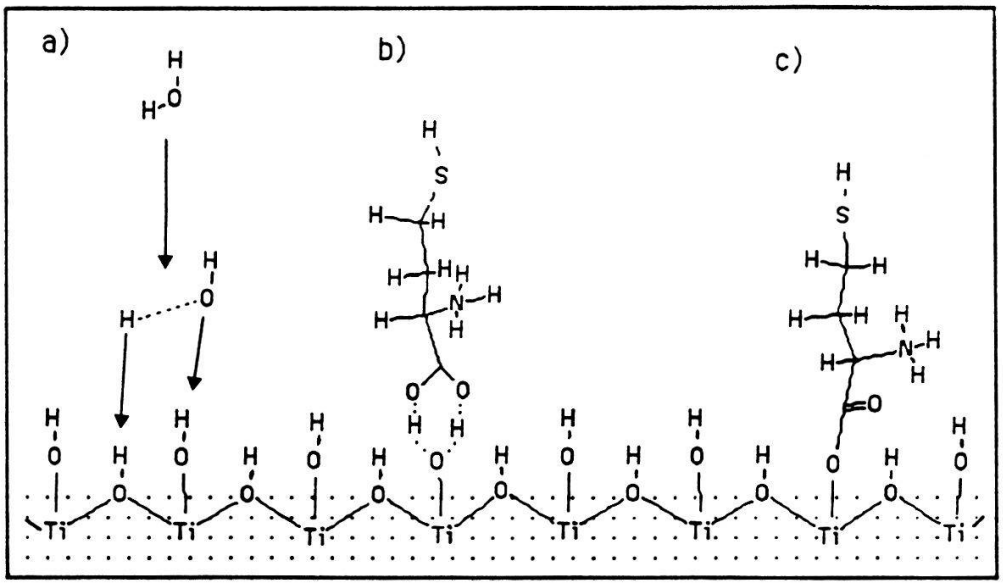

Several possible adsorption reactions have been proposed [3]. Two applicable cases are shown in fig. 1 for homocysteine on hydroxylated TiO_2. Fig. 1b shows one example of an electrostatic interaction based on proton transfer, fig. 1c a ligand exchange reaction. The latter should result in stronger binding and in specific (adsorbate dependent) adsorption [3]. Both mechanisms, however, lead to almost identical orientations of the adsorbed molecules.

About 300Å thick Ti layers were evaporated on glass platelets which were immersed for 10 to 15 hours in 10 mM NaCl/10 mM amino acid solutions of pH 2 to 11. The samples then were rinsed several times in 10 mM NaCl and pure water, spin dried, and transferred immediately to the vacuum system. The rinsing of the sample is expected to desorb those molecules which are not firmly attached to the TiO_2 surface. X- ray photoelectron spectroscopy (XPS) was used for surface analysis (Leybold EA 10, Mg$K\alpha$, electron take- off angle 20°)[4].

In photoelectron spectra amino acids can be identified by their O 1s, C 1s, and N 1s signals; for detailed analysis curve fits are necessary. Homocysteine additionally shows a S 2p peak. Amino acids in general adsorb specifically on TiO_2; this also was found for other adsorbates [3,5]. The examined amino acids preferentially adsorb from acidic solutions, e. g. homocysteine at pH 2 to 5. At this pH both the amino group (pos. charged) and the carboxylic group (neg. charged) are reactive, but on the TiO_2 mainly the basic OH group located on a Ti cation is available. Thus it is concluded that adsorption happens by ligand exchange: the basic OH on the Ti cation is replaced by the deprotonated, singly bound oxygen of the carboxylic group forming a carboxylate (fig. 1c). This corresponds to the adsorption mechanism which was found for carboxylic acids on TiO_2 powder [3,6]. The reaction is expected to compete with adsorption of chloride ions

from the salt solution and carbon dioxide from air. No Cl signal is detected by XPS, but there is evidence of bicarbonate formation when CO_2 reacts with the remaining basic OH groups.

The Ti 2p binding energy (BE) of 458.5 eV indicates TiO_2. A S 2p BE of 162.7 eV stands for a SH group and excludes a metal- sulphur bond [7,8]. The O1s, C 1s, and N 1s peaks are treated by curve fitting routines. Some details are summarized for pH 2 to 5; asterisks mark adsorption dependent signals that decrease or vanish at higher pH:

term	measured BE (eV)	width (eV)	probable chem. species	Ref.
O1	529.8	1.4	oxide	[9]
O2	530.5	1.4	acidic surface OH	[9]
O3	531.7	1.4	-C=O	[10]
O4 *	532.9	1.4	-C-O-X (X≠H)	[8]
C1 *	284.6	1.8	-C=C-, -C-C-, $-CH_2$	[8,10]
C2 *	286.0	1.9	-C-H-R	[8]
C3 *	288.3	1.9	-C=O, -C-O-, $-HCO_3$	[8,10]
N2 *	399.5	1.9	$-NH_2$	[8]
N3 *	401.4	1.9	$-NH_3$	[8]

O4 is interpreted as the singly bound O of the carboxyl group being attached directly to the Ti cation, O3 as the doubly bound O (fig. 1c). The appearance of two distinguishable carboxylic O 1s signals indicates that the strongly adsorbed molecules are not adsorbed as zwitterions. This does not exclude the existence of weaker bound zwitterionic species (e.g. fig. 1b) which might be desorbed by rinsing or by UHV. The amino group signals N2 and N3 have approximately equal intensities. The appearance of species N2 is not expected for low pH and might be the result of co- adsorption of cationic impurities being part of the homocystein powder.

If as many sites as possible are occupied on the TiO_2 the adsorbed homocysteine molecules should rather have an oriented ("standing") position than a random one. The S signal should be less attenuated than the O and C signals from the carboxylic group (O3, O4, C3) and the N signal from the amino group (N=N2+N3). Because the C3 signal arises from both the carboxylic group and bicarbonates, C3 has to be corrected; this is done by comparing O4 and O3 to determine the amount of bicarbonates. The following table summarizes some theoretical and experimental (averaged) peak ratios (after consideration of ionization cross sections) obtained from measurements at pH 2 to 5.

peak ratios	calculated		measured
	random	oriented	*(corrected)*
O4 : S	1.0	0.4	0.4
N : S	1.0	0.6	0.7
C3 : S	1.0	0.5	0.9 *(0.5)*
O4 : N	1.0	0.6	0.5
C3 : N	1.0	0.9	1.2 *(0.7)*
C3 : O4	1.0	1.3	2.5 *(1.4)*

It can be concluded that the pH for adsorption, the XPS binding energies, and the agreement between expected and measured line intensity ratios indicate a ligand exchange mechanism as the most probable adsorption reaction for homocysteine on TiO_2. This results in a relatively strong chemical bond with some covalent character. These or similar reactions can be important steps for the integration of Ti or Ti alloy implants in the human body.

The author thanks Prof. S. G. Steinemann for his wise, critical remarks during helpful discussions.

[1] H. P. Boehm, Angew. Chem. **12** (1966) 617
[2] A. L. Lehninger, Biochemistry, Worth Publishers (1975) ch. 4
[3] R. Flaig- Baumann, M. Herrmann, H. P. Boehm, Z. anorg. allg. Chem. **372** (1970) 296
[4] M. Schmidt, S. G. Steinemann, Fresenius Z. Anal. Chem. (1991) in print
[5] H. P. Boehm, Disc. Faraday Soc. **52** (1971) 264
[6] A. V. Kiselev, A. V. Uvarov, Surface Sci. **6** (1967) 399 ; I. T. Smith, Nature **201** (1964) 67
[7] C. R. Cothern et al., Anal. Chem. **48** (1976) 162
[8] D. T. Clark, J. Peeling, L. Colling, Biochim. Biophys. Acta **453** (1976) 533
[9] T. K. Sham, M. S. Lazarus, Chem. Phys. Letters **68** (1979) 426
[10] A. P. Pijpers, R. J. Meier, J. Electron Spect. Rel. Phenomena **43** (1987) 131

Cross section of adsorbed NO on Pt(111) to thermal He scattering

M. Croci, B. Calpini and R. Monot

Institut de Physique Expérimentale, Ecole Polytechnique Fédérale de Lausanne, PHB-Ecublens, 1015 Lausanne, Switzerland

The specularly reflected intensity of a He beam on a Pt (111) surface has been measured as a function of exposure to NO. The exponential attenuation is interpreted as due to randomly distributed adsorbed NO with a scattering cross section $\Sigma = (160 \pm 20)$ Å^2.

The specularly reflected intensity of a hypersonic helium beam is very sensitive to the crystalline quality and the cleanliness of a surface [1]. This property can be used to monitor the amount of adsorbed molecules on a metallic single crystal surface like NO on Pt (111). In the case of adsorbed molecules randomly distributed, the relative specular beam intensity is a measure of the proportion of the surface free of adsorbates [2]. If σ is the surface unit cell which is supposed to correspond to one atomic site, and if Σ is the cross section of the adsorbed molecules, the relative specular intensity is given by

$$\frac{I}{I_0} = (1-\theta)^{\alpha} \cong \exp(-\alpha\theta) \qquad (1)$$

where $\alpha = \Sigma/\sigma$.

The molecular beam experimental setup is described in detail elsewhere [3]. The base pressure in the analysis chamber is in the low 10^{-10} mbar range. Before measurements, the sample is cleaned by successive cycles of Ar ion bombardment, heat treatment and exposure to 10^{-6} mbar of O_2 at 600 °C. The surface is considered ready for the adsorption study when the specular He reflection intensity does not increase anymore by additional cleaning cycles. A He beam (63 meV) characterized by a relatively low speed ratio of about 15 is found perfectly convenient.

Fig. 1 shows the relative intensity of the specular He beam as a function of NO exposure at 300 K (NO purity 99.9). The angle of incidence is 40°. Absolute pressure calibration has been made using a spinning rotor viscosity gauge (Leybold Viscovac) and a partial pressure mass spectrometer (Leybold Quadruvac). The exponential attenuation is in agreement with equation (1) and corresponds to $\alpha = 24 \pm 3$ i.e. $\Sigma \cong 160 \pm 20$ Å. This very large value for the cross section is due to the long

range van der Waals forces between the He atoms and the Pt surface. Published results [2] of similar measurements with CO on Pt (111) show also a large value of the cross section $\Sigma_{CO} \cong 125$ Å. We found for CO under identical conditions as with NO, $\Sigma_{CO} \cong (100 \pm 20)$ Å^2.

These measurements have been made with a crystal prepared in the laboratory of prof. G. Comsa, Kernforschungsanlage, Jülich. The help of R. David in early experiments is warmly acknowledged.

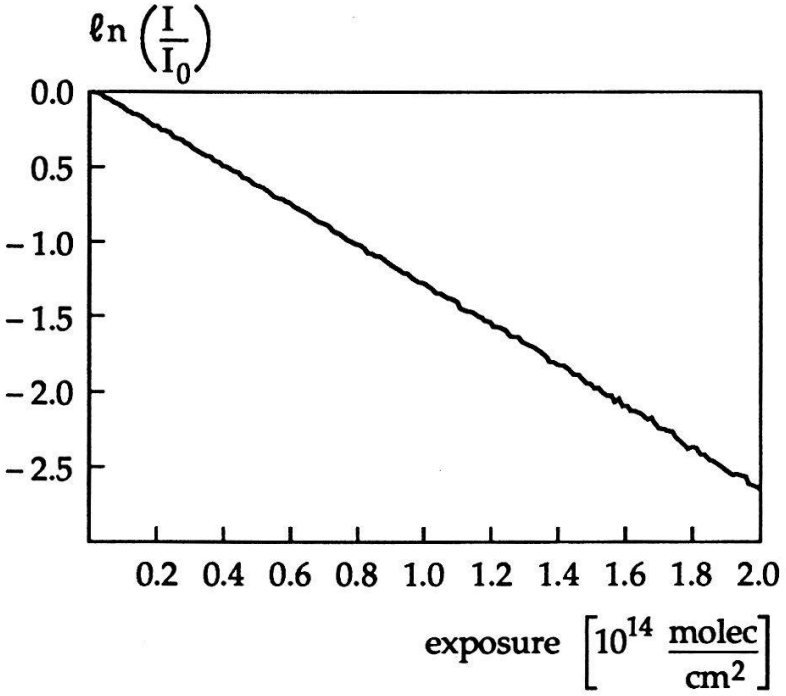

Fig. 1 : Relative specular He beam intensity as a function of NO exposure to Pt (111) surface at 300 K.

References :

[1] B. Poelsema, G. Comsa, Scattering of Thermal Energy Atoms, STMP 115, Springer-Verlag (1989).

[2] B. Poelsema, R.L. Palmer, G. Comsa, Surface Science **136**, 1 (1984).

[3] B. Calpini, M. Croci, R. David, R. Monot, to be published.
B. Calpini, PHD Thesis, EPFL, no. 896 (1990).

Dc size effects in Cd wires and surface structure by SEM

J. Romero*, T. Fleischer and R. Huguenin

Institut de Physique Exprimentale, Université de Lausanne, BSP, CH-1015 Lausanne

* Present address : PMOD/WRC, Dorfstrasse 33, 7260 Davos-Dorf

Abstract: *We present results on the dc electrical resistivity $\rho(d,T)$ of thin Cd wires. In our samples the bulk mean free path $\ell_\infty(T)$ is of the order of the sample diameter d and the conduction electrons undergo multiple scattering at the sample surface. So, chemical treatments yielding a polished or rough surface influence strongly $\rho(d,T)$. Our results are compared with results obtained on thin Cd plates. A scanning electron microscopy (SEM) analysis of the sample surface after the chemical treatments is also carried out.*

In a recent paper on size effects in the dc electrical resistivity of Cd, van der Maas and Huguenin [1] have shown that it is possible to change reproducibly the surface condition of the samples, leading to a change of $\rho(d,T)$ qualitatively described by the surface scattering model of Soffer [2]. One essential feature of this model is that the specularity parameter p giving the probability of a specular reflection at the sample surface is angle-dependent : $p=exp(-(4\pi r)^2 cos^2\theta)$ where θ is the angle between the surface normal and the trajectory of the incident electron and $r=h/\lambda$ the roughness parameter (h : root mean square of the asperities on the surface and λ the Fermi wavelength of the electron in Cd).

Our goal is to test in wires and in a different range of $\kappa=d/\ell$ the results of van der Maas and Huguenin [1] on $\rho(d,T)$ in thin plates with samples cut in the same monocrystal and hence having the same purity and value of the bulk parameters of the resistivity and to which the same surface treatments are applied. We also observe the sample surface after the chemical treatments with SEM in order to get insight on the geometrical roughness. Such an analysis was already carried out on thin Al plates where the state of the surface was analysed and correlated with dc resistivity measurements [3].

Initially the *6N* purity sample *(RRR=18000)* had a square cross section which became quasi-circular with diameter d after a few treatments. It had a tuning fork geometry with the current flowing perpendicularly to the c axis. The experimental setup used for the dc measurements between *1.15* and *9 K* and the procedures used to change the specularity state of the surface are presented in [1]. These chemical etching and polishing procedures thinned the bulk initial sample and yielded the successive samples with smaller diameters.

The parameters of $\rho(d,T)$ are obtained by fitting $\rho_0(d)=\rho(d;T=1.15K)$ as a function of d with Soffer theory as shown in *Fig.1*, yielding $\rho_\infty=3.49\pm0.04$ $p\Omega m$, $\ell_\infty=305\pm5$ μm and $\rho\ell=1.06\pm0.03$ $f\Omega m^2$. This last value is in contrast with that obtained in [1] which is 2.0 ± 0.1 $f\Omega m^2$, and with that of the free electron model *0.62* $f\Omega m^2$. As Cd is an anisotropic metal and is certainly not well described by a free electron model, the discrepancy with this last value is not surprising. However, the difference between plates and wires is not explained although it has already been reported by Aleksandrov [4] who gave *1.8* and *2.1* $f\Omega m^2$ for wires and *4.3* $f\Omega m^2$ for plates. There is ended no obvious reason why the wire geometry should emphasise more the free electron character than in plates. The value found for $\rho\ell$ is also obtained at all temperatures between *1.15* and *9 K* in a "Nordheim plot" in which the polished and etched states of the surface are close for thick samples and yield unambiguously the values of ρ_∞ and $\rho\ell$ respectively as ordinate at the origin and as *4/3* of the slope of the straight line.

The values of the roughness parameter r found in our polished and etched samples are very close (polished : $r=0.21$, etched : $r=0.23$) which is in contrast with the values obtained in [1] (polished : $r=0.8$; etched : $r>3$). These values

are, in any case, not unambiguously determined because variations of more than *50%* are possible with a fit to the temperature dependent part of $\rho(d,T)$ which is only in qualitative agreement. Notwithstanding, even with a small difference in r the polished and etched states can be separated and accounted for by Soffer theory at least qualitatively. This shows in one hand that the scattering of the conduction electrons at the metal surface is fairly specular but in the other hand that a slight difference in the surface state is sufficient to produce detectable changes in $\rho(d,T)$. Furthermore, the rms of the asperities deduced from $r=0.2$ corresponds (with $\lambda = 4.5$ Å) to a geometrical mean roughness at the atomic scale of *~1 Å*, which is not detectable by our SEM resolution.

The resolution of our SEM pictures is of *500 Å*. This is at least 2 orders of magnitude larger than the value of the geometrical roughness deduced from r. The roughness seen in the SEM pictures for the etched surfaces varies between *2500* and *5000 Å* and that of the polished samples can not be distinguished at the limit of our resolution, i.e. *500 Å*. The exposition to air does not seem to have an influence on $\rho(d,T)$ once the surface is prepared as shows the fact that the same values are obtained immediately after preparation or days later. The optical aspect of the rough states is mat and that of the polished states very shiny.

The conclusions are that the surface treatments affect reproducibly $\rho(d,T)$ which is accounted for by these simple size effects theory. A correspondence between the geometrical roughness of the sample surface as observed by SEM and the specularity parameter p can be established although the value of the rms of the asperities deduced from r is at least two orders of magnitude smaller than the geometrical roughness of the surface as observed by SEM.

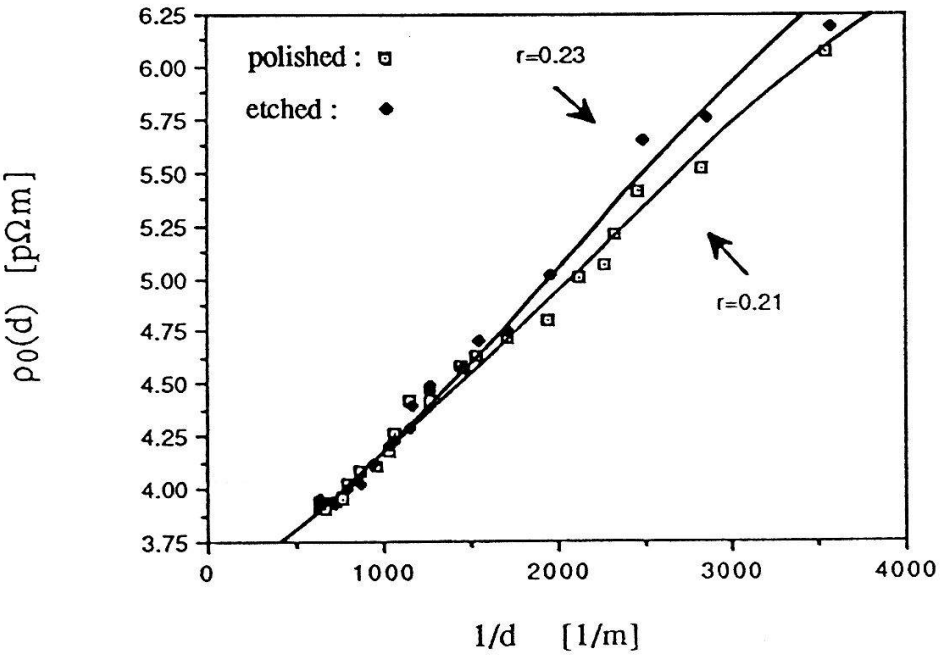

Figure 1. Nordheim plot : $\rho_0(d)=\rho(d;T=1.15K)$ as a function of the diameter d. The curves are Soffer theory with the parameters indicated in the text.

Acknowledgements: G. Burri for the SEM analysis and the Swiss National Science Foundation for financial support are gratefully acknowledged.

References:

[1] van der Maas, J. and Huguenin, R., J. Phys. : Condens. Mat. **2** (1990) 8137-59
[2] Soffer, S. B., J. Appl. Phys. **38** (1967) 1710-15
[3] Romero, J., Schmidt, M., Steinemann, S. and Huguenin, R., Helvetica Physica Acta **63** (1990) 811-2
[4] Aleksandrov, B. N., JETP **16** (1963) 286-94

Structure of the stable decagonal Al-Mn-Pd quasicrystal

C. Beeli and H.-U. Nissen
Laboratory of Solid State Physics, ETH Zürich, 8093 Zürich, Switzerland

In the Al-Mn-Pd system a stable face-centred icosahedral ($Al_{70}Mn_9Pd_{21}$) as well as a stable decagonal ($Al_{70}Mn_{17}Pd_{13}$) quasicrystal phase exist. This decagonal quasicrystal structure is compared to the structure of other decagonal quasicrystals.

The Al-Mn-Pd system is the first system in which a stable face-centred icosahedral as well as a stable decagonal quasicrystal phase exist [1]. The icosahedral Al-Mn-Pd quasicrystal shows a very pronounced chemical ordering [2] and seems to be stable in the whole temperature range from 800 °C down to 500 °C [3]. It is the purpose of this study to clarify the atomic structure of the decagonal Al-Mn-Pd quasicrystal.

An as-cast alloy of $Al_{70}Mn_{17}Pd_{13}$ composition has been annealed for 48 hours at 800 °C. Inside the cavities of the specimen single quasicrystals of dimensions up to 0.5 mm and diameters of 0.1 mm have been found. These single quasicrystals will be used for single crystal X-ray diffraction studies and a structure analysis analogous to that of decagonal Al-Cu-Co quasicrystals [4] is planned.

Figure 1a presents a typical 10-fold electron diffraction pattern with very sharp diffraction spots and no diffuse scattering intensity. Metastable decagonal Al-Mn quasicrystals show strong diffuse scattering in the 10-fold diffraction pattern [5]. The electron diffraction pattern shown in Fig. 1b shows 2-fold symmetry. The diffuse streaks of intensity perpendicular to the 10-fold axis should be extinct as a result of the 10_5 screw axis symmetry element of the decagonal structure and a truly quasiperiodic decagonal structure would thus not show any diffuse scattering at these positions. The occurence of this diffuse scattering intensity is interpreted as due to the random-tiling-like structure of the quasicrystal suggested previously [1,6]. The high-resolution image shown in Fig. 1c reveals structural details inside the individual tiling units of the random-tiling-like structure with tiling units of 21 Å edge length [1]. By contrast, the structure of decagonal Al-Mn quasicrystals is a random-tiling structure with an edge length of only 6.5 Å [5]. The much larger size of the basic structural units reflects the almost perfect decagonal atomic order of stable decagonal Al-Mn-Pd quasicrystals. The image contrast is very similar to the decagonal structure of Al-Cu-Co quasicrystals projected along the 10-fold axis [4]. An attempt to verify these similarities by electron microscopic image contrast simulations is under way.

References

[1] C. Beeli, H.-U. Nissen and J. Robadey, Phil. Mag. Lett. **63**, 87-95 (1991)

[2] A.P. Tsai, A. Inoue, Y. Yokoyama and T. Masumoto, Phil. Mag. Lett. **61**, 9 (1990)

[3] C. Beeli, P. Wildisen and H.-U. Nissen, submitted to Phil. Mag. Lett. (1991)

[4] W. Steurer and K.H. Kuo, Acta Cryst **B46**, 703 (1990)

[5] K. Hiraga, JEOL NEWS Vol. **25E** No. 1, 11 (1987)

[6] C.L. Henley, J. Phys. A: Math. Gen. **21**, 1649 (1988)

Fig.1. (a) 10-fold diffraction pattern, (b) 2-fold diffraction pattern and (c) high-resolution micrograph of the stable decagonal Al-Mn-Pd quasicrystal in a 10-fold projection.

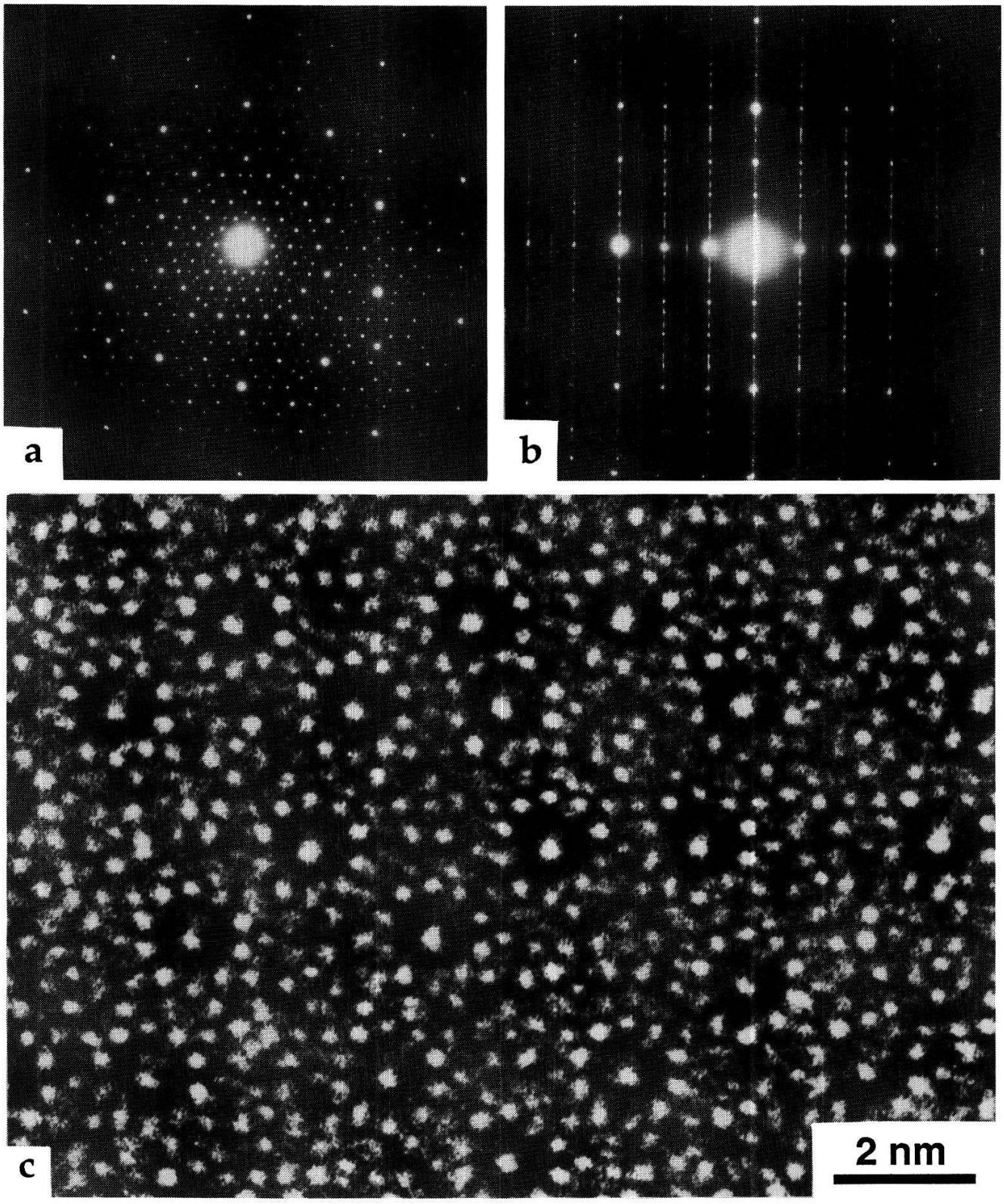

Electronic Structure of Hydrogen Passivated/Activated Centers in Semiconductors

Dj. M. Maric and P. F. Meier
Physik-Institut der Universität Zürich-Irchel, CH-8057 Zürich

A variety of experimental data on hydrogen-impurity pairs in semiconductors shows that besides passivating the electrical activity of some impurities, H atoms also induce electrical activity in others. We report *ab-initio* Hartree-Fock cluster calculations for the (B,H) and (C,H) pairs in Si and Ge, and for the (Si,H) pair in Ge. The stable and metastable configurations, potential energy hypersurface and electronic structures are obtained. From the calculated wavefunctions, in the case of the (B,H) pair, the electric field gradients at the quadrupolar nuclei are estimated, and thereby the quadrupole resonance frequencies in the possible μLCR experiment. In the case of (C,H) and (Si,H) pairs, the distribution of the spin density is obtained and the possible μSR experiment is discussed.

Experiments carried out over the past decade have shown that hydrogen has a profound effect on the electrical properties of semiconductors [1]. Besides isolated atomic states, mostly studied by μSR experiments (Mu and Mu* states) [2], H also builds complexes with other impurities leading to the passivation of both shallow acceptors (B, Al, Ga) and donors (P, As), as well as to the activation of the normally electrically inactive impurities (substitutional C and Si in Ge). Generally, three different sites of the hydrogen relative to the impurity are discussed, namely bond-centred (BC), antibonding to the defect or antibonding to an adjacent host atom.

By means of *ab-initio* Hartree-Fock cluster calculations we have investigated the microscopic structure of these complexes. The geometries of all configurations were optimised preserving the C_{3v} symmetry and using the polarised double-zeta basis sets for the valence orbitals, and *ab-initio* pseudopotentials for the core orbitals.

The H passivated B in Si is the most studied passivation complex. The preferred location of the proton close to the center of a relaxed B-Si bond is supported by infrared and Raman spectroscopy, as well as by the theoretical results of various computational methods, e.g. *ab-initio* (Hartree-Fock) [3:a,b], local density functional [3:c,d] and semiempirical (MNDO) [3:e]. Table 1 shows the obtained lowest energy configurations of Si:(B,H).

dist. (Å)	this work	Ref. 3a	Ref. 3b	Ref. 3c	Ref. 3d	Ref. 3e
displ.(B)	0.473	large	0.472	0.47	0.42	0.50
displ.(Si)	0.162	small	0.144	-	0.24	0.27
B-H	1.534	1.59	1.484	-	1.36	1.68
Si-H	1.486	1.46	1.484	1.63	1.65	1.43

Table 1: Calculated equilibrium geometries for Si:(B,H). The H atom resides close to the BC site of the relaxed Si-B bond. The displacements of the neighbouring Si and B atoms (outward, as measured from their ideal lattice positions) and their distances to the H atom are given.

The elements of the electric field gradient tensor were then calculated from the wavefunction describing this equilibrium structure. From the value, $V_{zz} = -0.376\,a.u.$ ($1\,\text{a.u.} = 0.972\,\text{V/cm}^2$), at the B nucleus the quadrupole resonance frequency can be predicted which will be useful for future quadrupole resonance spectroscopic experiments.

For the (B,H) pair in Ge, we obtain a similar microscopic structure to Si:(B,H). The lowest energy configuration is BC, but the potential energy hypersurface for H is about 20% more flat than in the Si crystal. This is in agreement with the experimental result that the (B,H) pair is less stable in Ge than Si.

The preliminary calculations for (C,H) and (Si,H) pairs in Ge and the (C,H) pair in Si predict the resulting complex rather similar to Mu*, though the calculations suggest a more lop–sided wavefunction. The spin density distribution for the (C,H) pair in Si is compared to the Mu* state in pure Si, as shown in Fig. 1. In the Si:(C,H) case most of the spin density is placed on the C atom, and some also on the proton. This implies a contact interaction for the proton - or, equivalently, for a muon in its position - which is rather greater than for Mu* in pure Si. Based on this, an additional muonium state can be anticipated, resembling Mu* but with a significantly modified hyperfine tensor, relative to the undoped material.

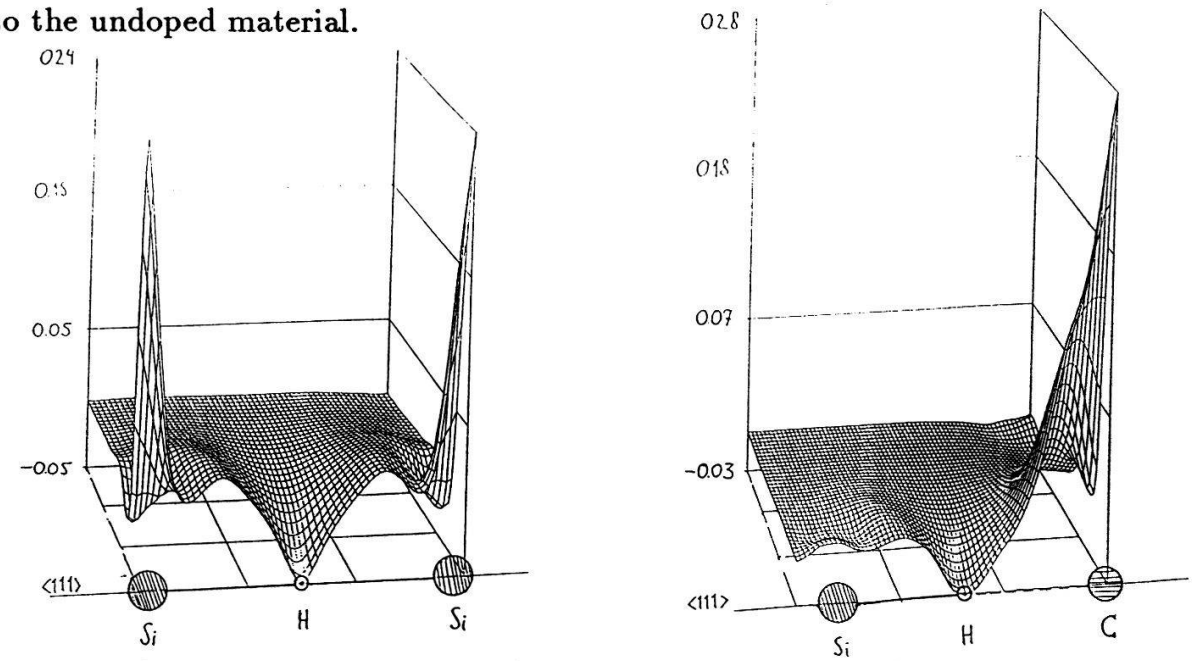

Figure 1: Spin density distribution (in atomic units). Left: H (or muonium) near the center of the relaxed Si–Si bond in the undoped silicon (Mu* state). Right: H close to the BC site of the relaxed Si–C bond (in C doped silicon).

References

[1] *Hydrogen in Semiconductors*,
Ed. J.I. Pankove and N.M. Johnson, (Academic Press, New York, 1990).

[2] B. D. Patterson, Rev. Mod. Phys. **60**, 69 (1988).

[3] (a): A.A. Bonapasta, A. Lapiccirella, N. Tomassini, M. Capizzi, Phys. Rev. **B36**, 6228 (1987);
(b): S.K. Estreicher, L. Throckmorton, D.S. Marynick, Phys. Rev. **B39**, 13241 (1989);
(c): K.J. Chang and D.J. Chadi, Phys. Rev. Lett. **60**, 1422 (1988);
(d): P.J.H. Denteneer, C.G. Van de Walle, S.T. Pantelides, Phys. Rev. **B39**, 10809 (1989);
(e): G.G. DeLeo and W.B. Fowler, Phys. Rev. **B31**, 6861 (1985).

Simulation of Cooling Rates in Supercooled Metal Droplets

Vitorvani Soares, Driss Houch, Erich Meyer*, and Léo Rinderer
Institute of Experimental Physics, University of Lausanne
CH-1015 Lausanne, Switzerland
*Institute of Physics - UFRJ, RJ-20945 Rio de Janeiro, Brazil

The evolution towards equilibrium of liquid metal droplets, taken out of equilibrium by rapid quenching before dendritic crystal growth, is discussed by simulating the cooling rate during the non-equilibrium process. The results are compared to the experimental data and we have investigated the possibility of a non-isothermal nucleation mechanism.

1. Introduction.

There is a significant range of temperature, under the melting point of the materials, over which the liquid state can exist in metastable equilibrium, and this amount of supercooling that the materials can sustain is an important parameter to the improvement of its physical properties. Many studies of supercooled liquid metals have been realized, and the dendritic crystal growth technique, coupled with a stereophotographic system, has been an effective method to the analysis of supercooled liquid metals with high melting point, revealing not only the cooling but also the liquid-solid phase transition.[1]

We attempt here a simple simulation of the cooling rate of these rapid quenched liquid droplets using heat transfer theory and we extend the experimental study of its thermodynamic properties to the region of supercooling. In our model, we assume that the droplet is a submillimeter sphere with radius R, density $\rho(T)$, specific heat $c_p(T)$, and emittance $\varepsilon(T)$. Under the rapid quenching processing, the high melting point metal droplets are cooled by radiation and the exchanging of energy with a helium gas at temperature T_o surrounding them. The form of the energy equation is, then, given by

$$-\rho c_p(R/3)(dT/dt) = \varepsilon\sigma T^4 + h(T - T_o), \qquad (1)$$

where σ is the Stefan-Boltzmann's constant, and h is the heat transfer coefficient, which is given by the equation $2Rh/k_f=2.0 + 0.6Re^{1/2}Pr^{1/3}$.[2] k_f, Re and Pr define, here, the thermal conductivity, the Reynolds and Prandtl number, respectively, for the helium gas. Our detailed calculations is based on these numbers and on the tabulated data of ρ, c_p, and ε for the solid phase.[3,4,5]

2. Results, Discussion, and Conclusion.

The measured and simulated cooling for a tungsten droplet is represented in the Figure. Over the temperature range of measurements, these coolings can be fitted adequately to a linear expression. We can

observe that the slope of the simulated calculation curve is greater than that to the supercooled liquid. Since the right side of eq. (1) is essentially given by the thermodynamic properties of the gas, this behavior of the slopes results from the heat capacity difference between the supercooled liquid and the crystalline solid. Our results suggest that the supercooled liquid has, then, heat capacity larger than that for the solid, which is in agreement with similar behavior observed on the undercooled liquid metals with low melting point.[6] More yet, they characterize a lower diffusivity inside the liquid than that inside the solid. Therefore, any heat produced during the rapid crystallization process remains essentially within the nucleus, inducing a non-isothermal process.

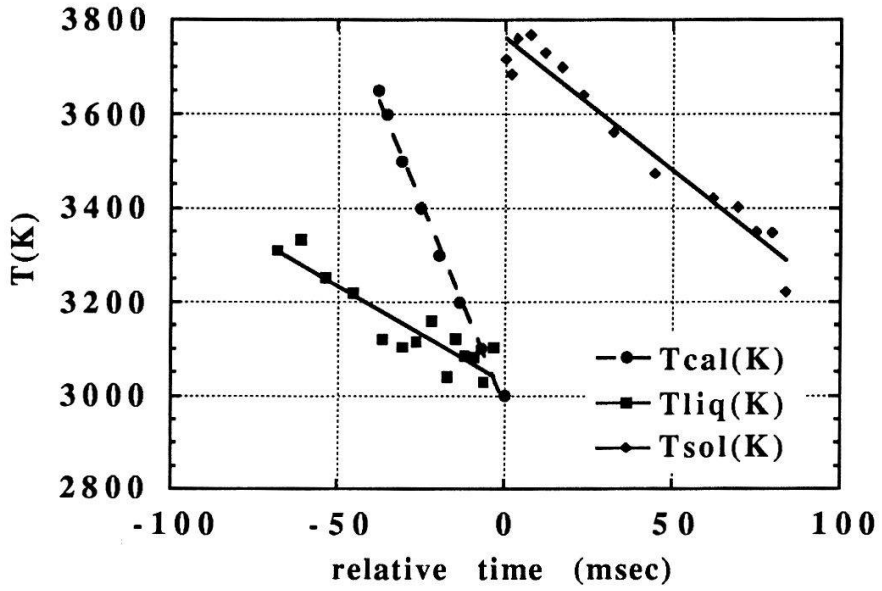

The FNRS (Switzerland) and CNPq (Brazil) are acknowledged for financial support.

References

[1] V. Soares, E. Meyer, and L. Rinderer, Helv. Phys. Acta, **63** (1990) 515

[2] R. B. Bird, W. E. Stwart, and E. N. Lightfoot, Transport Phenomena (Wiley, New York,1960)

[3] R. Hultgren, P. D. Desai, D. T. Hawkins, M. Gleiser, K. K. Kelley and D. D. Wagman, Selected Values of Thermodynamic Properties of the Elements (ASM, Metals Park, Ohio, 1973)

[4] R. C Weast (ed.), CRC - Handbook of Chemistry and Physics, 70th ed. (The Chemical Rubber Co., Cleveland, Ohio, 1989-90)

[5] Y. S. Touloukian, R. K. Kirby, R. E. Taylor, and P. D. Desai (eds.), TPRC Data Series, Thermal Expansion, metallic elements and alloys, Vol. 12 (IFI, Plenum, New York, 1975)

[6] J. H. Perepezko and J. S. Paik, J. of Non-Crystall. Sol., **61&62**(1984)113

An Analogy between Surface Waves on Helium II and Antiferromagnetism

Daniel A. Weiss, Max-Planck-Institut für Strömungsforschung, D-W-3400 Göttingen, Germany
Peter W. Egolf, Swiss Federal Laboratories for Materials Testing and Research CH-8600 Dübendorf, Switzerland

For a superfluid with a free surface driven from thermal equilibrium by standing waves of second sound a Hamiltonian surface description has been obtained, showing striking analogies to a Hamiltonian of antiferromagnetic systems; and indeed a (dynamical) phase transition can be observed on the free boundary of the cryogenic fluid.

The Landau-Olsen-system [1] essentially consists of superfluid helium II with a free surface. Standing waves of second sound in the bulk force surface patterns to develop on the free boundary of the fluid [2]. Such a system, in a harmonic approximation and for monochromatic second sound excitations, can be described by the following Lagrangian density [3]

$$\mathcal{L} = \rho_1 \frac{\partial \phi_1}{\partial t} - \frac{1}{2}\rho_1 (\mathrm{grad}\phi_1)^2 + \frac{1}{2}\left(\frac{\omega_2}{c_2}\right)^2 \phi_2^2 - \frac{1}{2}\rho_2 (\mathrm{grad}\phi_2)^2 - \rho_1 g x_3 \qquad (1), \text{ where}$$

$$\vec{v} = -\,\mathrm{grad}\,\phi_1\,, \quad \vec{v}_n - \vec{v} = -\,\mathrm{grad}\,\phi_2\,, \quad \rho_1 \equiv \rho\,, \quad \rho_2 \equiv \frac{\rho_n}{\rho_s}\rho \qquad (2).$$

The gravitational field is assumed to be directed along the $-x_3$-axis of a rectangular coordinate system. The Lagrangian density contains the angular frequency ω_2 and the speed of second sound c_2. The density of the normal component is ρ_n and that of the superfluid component is ρ_s.

A Legendre transformation yields the Hamiltonian density [4]

$$\mathcal{H} = \frac{1}{2}\rho_1 (\mathrm{grad}\phi_1)^2 - \frac{1}{2}\left(\frac{\omega_2}{c_2}\right)^2 \phi_2^2 + \frac{1}{2}\rho_2 (\mathrm{grad}\phi_2)^2 + \rho_1 g x_3 \qquad (3).$$

To obtain the corresponding Hamilton function, this density has to be integrated over the whole domain containing superfluid. Let us assume that ρ_1 and ρ_2 are constants. By applying variational methods to the Lagrangian density (1) it is possible to derive equations of motion and boundary conditions of the system, which are also given in reference [3]. Making use of these equations and introducing Greens functions [4], one can derive the following non-local Hamiltonian

$$H = -\frac{1}{2}\rho_1 \int dx\, dy\, G_1(x,\eta(x);\, y,\eta(y)) \frac{\partial \eta}{\partial t}(x) \frac{\partial \eta}{\partial t}(y) - \frac{1}{2}\rho_2 \int_{D\times D} d\vec{\sigma}_x\, d\vec{\sigma}_y\, G_2(\vec{x},\vec{y}) \cdot$$

$$\frac{\partial \phi_2}{\partial n}(\vec{x}) \frac{\partial \phi_2}{\partial n}(\vec{y}) + \frac{1}{2}\rho_1 g \int dx\, \eta^2(x) + \mathrm{const} \qquad (4).$$

Here $x=(x_1,x_2)$ and $dx=dx_1dx_2$; η is the vertical elevation of the free liquid surface from its equilibrium position, occurring when there is no second sound excitation. D denotes the boundaries with entropy fluxes crossing them to or from the liquid, i.e. the surface of the second sound generator immersed into the fluid.

The form of equation (4) is similar to that of a Hamiltonian function of magnetic systems [5]

$$H_{magn} = \sum_{R,\,R`} J(R,R`)\; s(R)\; s(R`) \qquad (5).$$

In our case the interactions are of long range, the potential G_1 is mainly a 3d-Coulomb-potential; the 2d-Fourier-transform of this is essentially $1/k$ [6]. G_1 is negative and therefore establishes an analogy to antiferromagnetic systems in thermodynamic equilibrium.

In reference [7] a nondimensional number, the Landau number, has been introduced, which is proportional to the square of the heating power of the second sound generator. Therefore it defines a stress number and control parameter of the system. When it is increased beyond a critical value La_c, stationary surface patterns, with elevation η_{stat}, are accompanied by oscillating surface structures, described by η_{osc}

$$\eta(t,x_1,x_2) = \eta_{stat}(x_1,x_2) + \eta_{osc}(t,x_1,x_2) \qquad (6).$$

Therefore, above La_c the symmetry in time is broken. The amplitude of η_{osc} yields an order parameter to describe this nonequilibrium phase transition [8].

And just as in an antiferromagnetic system in a vanishing external field, where the total magnetization is zero beneath and beyond the Néel temperature T_N, we have in the vicinity of La_c for any given Landau number

$$0 = \int dx_1dx_2\,\eta \quad \Rightarrow \quad 0 = \frac{d}{dt}\int dx_1dx_2\,\eta = \int dx_1dx_2\,\frac{\partial\eta}{\partial t} \qquad (7).$$

These equations correspond to mass conservation in the cavity containing superfluid ^{4}He.

References

[1] P.W. Egolf, 1990, PhD thesis, ETHZ, number 9290
[2] J.L. Olsen, 1985, J. Low Temp. Phys. **61**, 17
[3] P.W. Egolf, 1989, Helv. Phys. Acta, **62**, 219
[4] D.A. Weiss, 1989, diploma thesis, ETHZ, unpublished
[5] G.W. Krey, 1980, Phasenübergänge und kritische Phänomene, Vieweg Braunschweig/Wiesbaden
[6] D. M. Milder, 1977, J. Fluid Mech., **83**, 159
[7] P.W. Egolf and S. Di Nardo, 1991, Proc. of the 19th Int. Conf. on Low Temp Physics, Physica B **169**, 517
[8] P.W. Egolf, J.L. Olsen, B. Röhricht and D.A. Weiss, 1991, Proc. of the 19th Int. Conf. on Low Temp Physics, Physica B **169**, 217

General principles for the formation of spatial patterns in lasers and laser hydrodynamics

M. Brambilla[‡,•], L. A. Lugiato[•], V. Penna[†] and F. Prati[‡,•]

‡ Physik-Institut der Universität, CH-8057 Zürich
• Dip. di Fisica, Università di Milano, Milan, Italy
† Dip. di Fisica, Politecnico di Torino, Turin, Italy

We formulate a variational principle for the formation of stationary spatial patterns in a laser and we reshape the dynamical equations of the laser in the form of 'laser hydrodynamical equations' for a compressible fluid, similar to the law of mass conservation and to the Bernoulli equation.

The case of a frequency-degenerate family of modes. Variational principle for pattern selection.

We consider a ring laser with spherical mirrors and we assume that the electric field is a linear combination of the Gauss-Laguerre modes $A_{pl}(\rho,\varphi)$ belonging to a frequency-degenerate family $2p+|l|=q$ [1]

$$F(\rho,\varphi,\tau)=\sum_{pl}^{2p+|l|=q} f_{pl}(\tau)A_{pl}(\rho,\varphi) \quad , \tag{1}$$

If we now introduce the functional

$$V=\int_0^{2\pi} d\varphi \int_0^{\infty} d\rho\ \rho\Big[|F(\rho,\varphi)|^2-2Cln(1+|F(\rho,\varphi)|^2)\Big] \quad , \tag{2}$$

it is possible to show [2] that the dynamical equations for the modal amplitudes f_{pl} can be written in the form

$$\frac{df_{pl}}{d\tau}=-\frac{\partial V}{\partial f_{pl}^{*}} \quad . \tag{3}$$

Hence the stable stationary solutions of the system correspond to the local minima of the functional V, which therefore plays the role of a generalized free energy in this system which lies far from thermal equilibrium [3].

Laser hydrodynamics.

In this section we go beyond the case of a single degenerate family of modes and we let the electric field be a linear combination of all the transverse modes of the cavity. In this case the equation that governs the dynamical evolution of the electric field is [4]

$$\frac{\partial F}{\partial\tau}=-\Big[1-ia\Big(\frac{1}{4}\nabla_{\perp}^2-\rho^2+1\Big)\Big]F+2C\frac{(1-i\Delta)F}{1+\Delta^2+|F|^2} \tag{4}$$

where a is the detuning between two adjacent families of transverse modes and Δ is the atomic detuning. In order to reformulate Eq. (4) in the form of 'hydrodynamical equations' we put $F = |F|e^{i\Phi}$ and we introduce a 'mass density' $\sigma = |F|^2$ and a 'velocity' $\mathbf{v} = \frac{a}{2}\nabla\,\Phi$. With some algebraic manipulations, Eq. (4) and its complex conjugate can be cast in the form

$$\frac{\partial\sigma}{\partial\tau} + \nabla\cdot(\sigma\mathbf{v}) = 2\sigma\left[\frac{2C}{1+\Delta^2+\sigma} - 1\right] \tag{5}$$

$$\frac{\partial\Phi}{\partial\tau} = -\frac{a}{4}|\nabla\,\Phi|^2 + a\left[\frac{\nabla^2\sqrt{\sigma}}{4\sqrt{\sigma}} + 1 - \rho^2\right] - \frac{2C\Delta}{1+\Delta^2+\sigma} \tag{6}$$

We can compare Eqs. (5) and (6) with the fundamental equations of hydrodynamics, that are the equation of continuity for the mass density σ

$$\frac{\partial\sigma}{\partial\tau} + \nabla\cdot(\sigma\mathbf{v}) = 0 \tag{7}$$

and the Bernoulli equation for the velocity potential Φ

$$\frac{\partial\Phi}{\partial\tau} = -\frac{q}{4\pi}|\nabla\,\Phi|^2 + \mathcal{P}\frac{2\pi}{q} \tag{8}$$

which involves a pressure term $\mathcal{P}$ and a term q which is related to the vorticity of the fluid [2]. From the comparison between these two pairs of equations we can conclude that in the optical case the total 'mass' is not conserved because of the presence of the two dissipative terms that appear in the r.h.s. of Eq. (5), while the analogy with Bernoulli equation is complete if we put $q = \pi a$ and define a 'pressure'

$$\mathcal{P} = \frac{a^2}{2}\left[\frac{\nabla^2\sqrt{\sigma}}{4\sqrt{\sigma}} + 1 - \rho^2\right] - \frac{a}{2}\frac{2C\Delta}{1+\Delta^2+\sigma} \quad . \tag{9}$$

In this way we have established a formal analogy between lasers and hydrodynamics, in the sense that all the relevant physical quantities that describe a fluid, i.e. mass density, velocity and pressure, can be derived from the modulus and the phase of the electric field emitted by a laser.

References

[1] M. Brambilla, F. Prati, L. A. Lugiato and F. Battipede, preceding contribution to this volume

[2] M. Brambilla, L. A. Lugiato, V. Penna, F. Prati, C. Tamm and C. O. Weiss, Phys. Rev. **A**, to appear

[3] H. Haken , *"Synergetics: an Introduction"*, Springer-Verlag Berlin 1977

[4] L.A. Lugiato, G.L. Oppo, J. R.Tredicce and L.M. Narducci in Feature issue on *"Transverse Effects in Nonlinear Optical Systems"* N. B. Abraham and W. J. Firth eds. , Journ. Opt. Soc. Am. B June 1990

Multistability and Phase Singularities in Transverse Laser Patterns

M. Brambilla[‡,•], F. Prati[‡,•], L. A. Lugiato[•] and F. Battipede[•]

‡ Physik-Institut der Universität, CH-8057 Zürich

• Dip. di Fisica, Università di Milano, Milan, Italy

We analyze the interaction and the competition of a set of transverse cavity modes. The laser exhibits coexistence among different stationary spatial patterns . These structures display the presence of *phase singularities* analogous to the vortex structures known in such fields as, for example, hydrodynamics, superconductivity, superfluidity. These singularities are arranged in the form of regular *arrays* , and the equiphase lines of the field exhibit a notable similarity to the field lines of the electrostatic field generated by a correspoding set of point charges.

We have investigated the structure of the transverse profile of the field in the case of a homogeneously broadened 2-level active medium in a ring cavity with spherical mirrors. In this case the intrinsic cylindrical symmetry suggests the Gauss-Laguerre basis as a natural choice of eigenmode basis for the e.m. field in the cavity . According to the geometry of the cavity , the modes gather in frequency degenerate families, because the frequency of the modes depends on the combination $q = 2p + |l|$; so that each frequency degenerate family is composed by $q + 1$ modes. In order to simplify the model we considered a ring laser in which the atomic line is tuned to one of the families, and suppose that all other families are far enough from resonance to experience loss larger than gain, so that only the tuned family will contribute to the emission.

Under this approximation, we have expanded the slowly varying envelope of the electric field on the Gauss-Laguerre basis, only considering the contributions of the modes belonging to the active family $2p + |l| = q$. This ansatz is then introduced in the Maxwell Bloch equations including diffraction (see Ref. 1) which govern the dynamics of this system.

We found that there are different stationary transverse spatial patterns for the field intensity at steady state which are in general a linear combination of modes; we demonstrated that the coefficients of this combination minimize a generalized free energy (see Ref. 2).

By varying the pump parameter we have found transitions between patterns , corresponding to the spontaneous breaking of the cylindrical symmetry. We point that all of these configurations have been observed experimentally at P.T.B. in Braunschweig, in close correspondance with the theoretical predictions [3].

Some of the different configurations arise in overlapping regions of the parameter space, thus realizing the phenomenon of *spatial multistability* . If we consider the field pattern, taking into account phase relations, we discover cases of tristability for $2p + |l| = 2$, up to

eight coexisting patterns for $2p + |l| = 3$.
The stationary patterns display points in which both the real and the imaginary part of the electric field vanish simultaneously, and such that circulation of the phase gradient of the electric field on a closed loop around one of these points, yields a phase change by an integer multiple of 2π. The existence of these *phase singularity points* is evident both in the theory and in the experimental observations [3]. The behaviour of the electric field around each of these points exhibits many similarities with that of the optical vortices, recently discovered [4] in the framework of the model of Ref. 5. In our problem, the singularities arise from the combination of few modes instead of several modes. In our case the singularities occur at fixed points, arranged in the form of regular arrays (" phase singularities crystals") and the gradient of the phase of the electric field clearly shows a vortex structure, and in fact the gradient of the field phase plays the same role of the velocity field in hydrodynamics [2].

References

[1] L.A. Lugiato, F. Prati, L.M. Narducci and G.L. Oppo, Opt. Comm. **69**, 387 (1989)

[2] M. Brambilla, F. Battipede, L. A. Lugiato, V. Penna, F. Prati, C. Tamm and C. O. Weiss, *"Transverse Laser Patterns : I. Phase Singularity Crystals"*, Phys. Rev. A , to appear.

[3] C. Tamm and C. O. Weiss, Feature issue on *"Transverse Effects in Nonlinear Optical Systems"* N. B. Abraham and W. J. Firth eds. , Journ. Opt. Soc. Am. B , June 1990

[4] L.A. Lugiato, C. Oldano and L.M. Narducci, Journ. Opt. Soc. Am. B **5** 879 (1988)

[5] P. Coullet, L. Gil and F. Rocca, Opt. Comm. **73**, 403 (1989)

Bistability in the laser cooling of atomic beams

G. Broggi°, M. Brambilla°•, F. Casagrande•, L.A. Lugiato•

° Physik-Institut der Universität, Zürich; • Dip. di Fisica dell' Università, Milano (I)

We study the resonant interaction of a beam of two-level atoms with two counter-propagating frequency-chirped lasers, showing that the bistable response of the atomic deceleration to the sweeping rate gives origin to a double-peaked pseudo-stationary (PS) velocity distribution that lasts for a time interval which is orders of magnitude longer than the relaxation time to the PS state. Essentially the same response is predicted for a single laser interacting with two atomic transitions.

The very high coherence and brightness of laser sources allows to exploit the mechanical force exerted by light pressure on quasi-resonant neutral atoms to obtain a drastic compression of the velocity distribution of the sample atoms (*laser cooling*): this achievement has massively contributed to the progress of many branches of physics as surface theory, high-resolution spectroscopy etc. [1].

Here we consider a sample of two-level atoms (of mass m, velocity $\vec{v}$, transition frequency ω_a and natural linewidth Γ) travelling along the positive z-direction, and two counter-propagating laser beams of (quasi-resonant) frequencies $\omega_1 \lesssim \omega_0 \lesssim \omega_a$ and scaled intensities $I_{0,1} \equiv (\mathcal{I}/\mathcal{I}_S)_{0,1} \ll 1$ ($\mathcal{I}_S$ being the atomic saturation intensity). The atomic centre of mass is decelerated by the radiation pressure force due to the fluorescence cycles with the absorptions of counter-propagating photons and the spontaneous emission of randomly directed photons. The average radiation pressure $\vec{F}$ on one atom can be calculated as the sum of the average force from each laser; within our approximations one obtains: $\vec{F} = \sum_{i=0}^{1} \vec{F}_i \simeq \vec{u}_z \hbar(\omega_a/c)(\Gamma/2) \sum_{i=0}^{1} I_i / [1 + (4/\Gamma^2)(\omega_i - \omega_a + kv_z)^2]$. The force $\vec{F}$ is effective only close to resonance: therefore, the laser frequency must be chirped (in our case linearly, choosing $\omega_i(t) = \omega_i + \dot{\omega} t \simeq \omega_i - k\dot{v}_z t$), so as to compensate for the Doppler effect. Introducing dimensionless variables and parameters, switching to a (non-inertial) reference frame moving at a velocity depending on the chirping rate, and using the same symbols as in [2], one obtains:

$$\frac{dv'}{d\tau'} = e' - \frac{1-\eta'}{1+(v'+\delta)^2} - \frac{1+\eta'}{1+(v'-\delta)^2} \equiv K(v'), \tag{1}$$

where the scaled velocity v' is proportional to the overall detuning from resonance with included Doppler effect and laser frequency chirping, τ' and e' are dimensionless time and chirping rate, respectively, and η' and δ are laser intensity and frequency difference. At steady-state v' is therefore the solution of a three parameter quartic equation which, for suitable ranges of η' and δ, admits four real solutions whose stability is such that v' is a *bistable* function of the control parameter e'. The system dynamics can be conveniently described by introducing a potential U such that $dv'/d\tau' = -dU/dv'$. Again for suitable parameter ranges (e.g., in the case of ^{133}Cs, for $\eta' = 0.8$, $\delta = 1.5$, and $e' = 0.8$) the two minima (maxima) A,C (B,D) correspond to the stable (unstable) solutions of the steady-

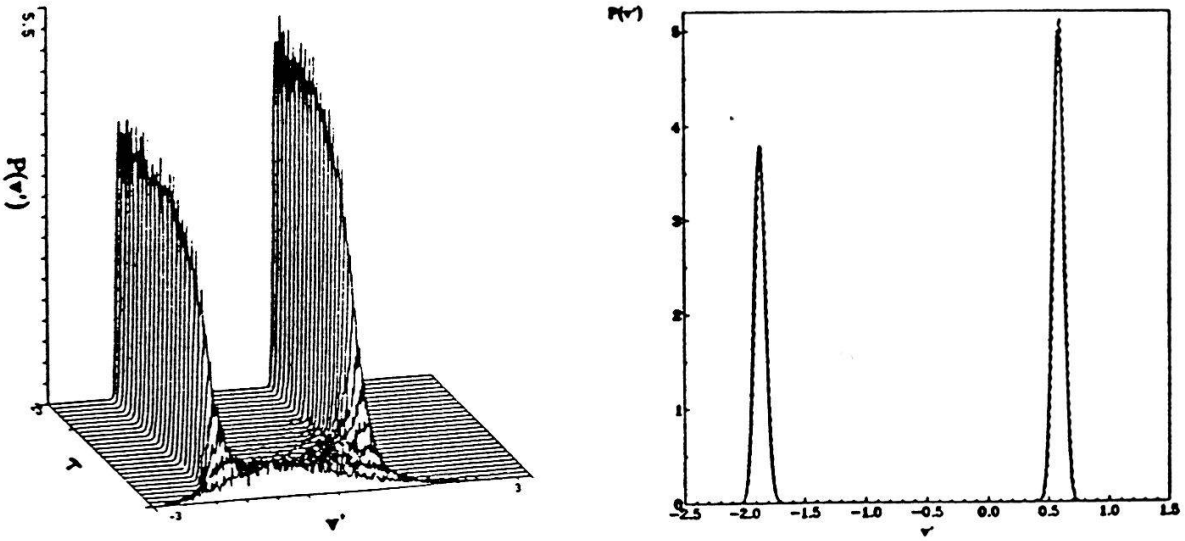

Figure 1: Velocity distribution of a ^{133}Cs atomic beam. a) Evolution from the initial Maxwellian distribution to the double-peaked configuration, as obtained from Langevin simulations. b) Comparison between the numerical result (solid line) and the approximated distribution (dashed line) obtained from the linearisation of the model FPE.

state equation, while $U(v') \to -\infty$ as $v' \to +\infty$, i.e., the potential has no lower bound (i.e., atoms with $v' > v'_D$ cannot be laser-cooled).

We now consider the fluctuations originated by the random nature of both the direction and the number per unit time of spontaneously emitted photons and write the Fokker-Planck equation (FPE) for the evolution of the atomic velocity distribution $P(v', \tau')$:

$$\frac{\partial P(v',\tau')}{\partial \tau'} = -\frac{\partial}{\partial v'}\left[K(v')P(v',\tau')\right] + q\frac{\partial^2}{\partial v'^2}\left[D(v')P(v',\tau')\right], \qquad (2)$$

where $D(v') = e' - K(v')$, $q = (7/5)(\hbar k^2)/(m\Gamma)$ (e.g., for ^{133}Cs, $q = 1.3 \times 10^{-3}$) and the two lasers have been assumed to be uncorrelated. The FPE (2) does not admit a stationary solution, as a consequence of the structure of the potential $U(v')$: in fact, fluctuations make the atoms escape from the potential wells by tunnelling to the region of uncontrollable velocity $v' \geq v'_D$. However, there exist two very different time-scales in the dynamics of the atomic distribution, i.e., a faster time scale for the evolution from the initial Maxwellian to the PS double-peaked distribution, and an extremely slower one for the escape, which depends exponentially on $1/q \gg 1$. One can approximate the two-peaked PS distribution by a weighted linear combination of the Gaussian solutions $G_A(v'), G_C(v')$ of the FPE (2) linearised around the two minima at $v' = v'_{A,C}$: $P(v') = \mathcal{N}_A G_A(v') + \mathcal{N}_C G_C(v')$. This procedure will be discussed in detail in a future work. In fig. 1b this approximated analytic distribution is compared with the results of the numeric simulation of the cooling of ^{133}Cs, obtained by performing Langevin stochastic integrations (8704 realisations; $\tau' = 500$, histograms on 600 bins). The time evolution from the initial Maxwellian distribution to the PS configuration is finally illustrated in fig. 1a (same parameter values).

References

[1] Special Issue on *Laser Cooling and Trapping of Atoms*, J.Opt.Soc.Am.B **6** (1989)

[2] A.Aspect, R.Bonifacio, F.Casagrande and L.A.Lugiato, Europhys.Lett. **7**, 499 (1988)

EXTENDED BLOCH-TYPE NMR-LASER MODEL

L. FLEPP, R. HOLZNER, E. BRUN, F. WALDNER
Physik-Institut der Universität Zürich, CH-8001 Zürich
M. FINARDI, R. BADII
Paul-Scherrer Institut, LUS, 5232 Villigen PSI

ABSTRACT: The conventional Bloch–type equations do not correctly describe the interplay of noise and coherence which affects all facets of the regular and chaotic NMR laser response. Therefore, a search for improved laser equations was considered as essential to a better comparision of theory and experiment. The result was a break-through: extended Bloch-type laser (EBL) equations with greatly improved forecasting power are now avaible to quantitatively model the NMR laser behavior also in the presence of stochastic noise.

1. EBL–MODEL

In order to obtain dynamic NMR laser equations in the rotating (u,v,z) frame approximation, we follow the treatment of Ref.[1] with two significant alterations, however. First, to include Nyquist noise in the NMR coil, we add stochastic driving terms $B_{uu}(t)$ and $B_{vn}(t)$ (Langevin terms) to the coherent field equations. Second, we argue that the observed spin-dephasing or spin-memory loss may not be purely exponential. Thus, the transverse decay rate $\gamma_\perp$ must be changed accordingly. Therefore, we replace $\gamma_\perp$ by $\gamma_\perp(1+\alpha M_t)$ thus taking into account lowest-order nonexponential dephasing which is proportional to the amplitude M_t of the rotating nuclear magnetization. With these assumptions we obtain modified laser equations of the form

$$\begin{aligned} \dot{m} &= -\left[\gamma_\perp\left(1+\alpha\sqrt{mm^*}\right)+i\Delta\omega_a\right]m - isbM_z \\ \dot{M}_z &= -\gamma_{||}(M_z - M_e) + \frac{ig}{2}(mb^* - m^*b) \\ \dot{b} &= -(k+i\Delta\omega_c)(b - b_n(t))\,. \end{aligned} \tag{1}$$

We call them extended Bloch–type laser (EBL) equations for the free running NMR laser (FRL). They are the starting set of nonlinear differential equations for laser variants: the parametrically modulated laser (PML), the laser with injected signal (LIS), the laser with phase-locked feedback (LPF), the laser with delayed feedback (LDF), etc.

2. EBL–MODEL TESTED

The laser transient after Q-switching shown in Ref.[2] provided a first confirmation of the validity of the above approach although limited to a short time-interval and to a single-parameter choice. In order to extend our analysis we investigated the Q-modulated laser with $Q(t)=Q(1+A\cos\omega t)$. Fig. 1 compares experimental and simulated 2d-embeddings of a chaotic time series. Fig. 2 depicts the bifurcation structure by means of phase diagrams in the ω-A parameter-plane: Various domains of stable limit cycle behavior of period-n, n = 1,2,3,... are marked for experiment and model. The pictures are in excellent agreement: minor differences are due to the effect of experimental noise; also the finiteness of the measurement resolution for the employed parameter values (2-3 digits) contributes to the uncertainty of the comparision.

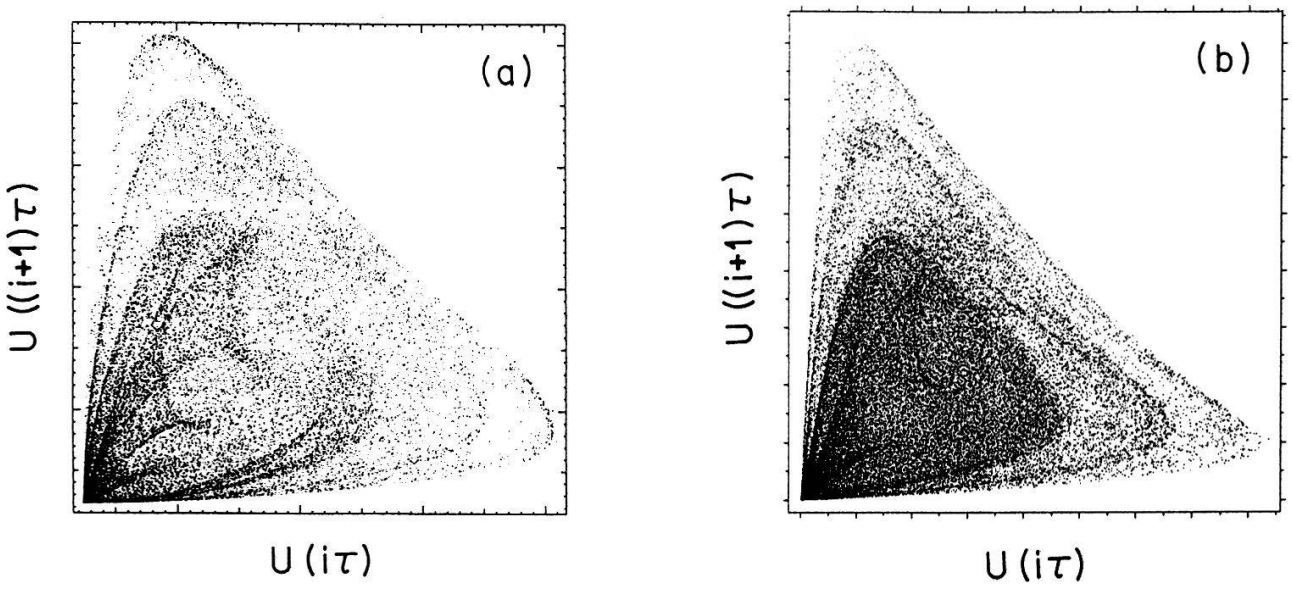

Fig. 1: 2-dimensional embeddings of a strange attractor: (a) experiment, (b) EBL model.

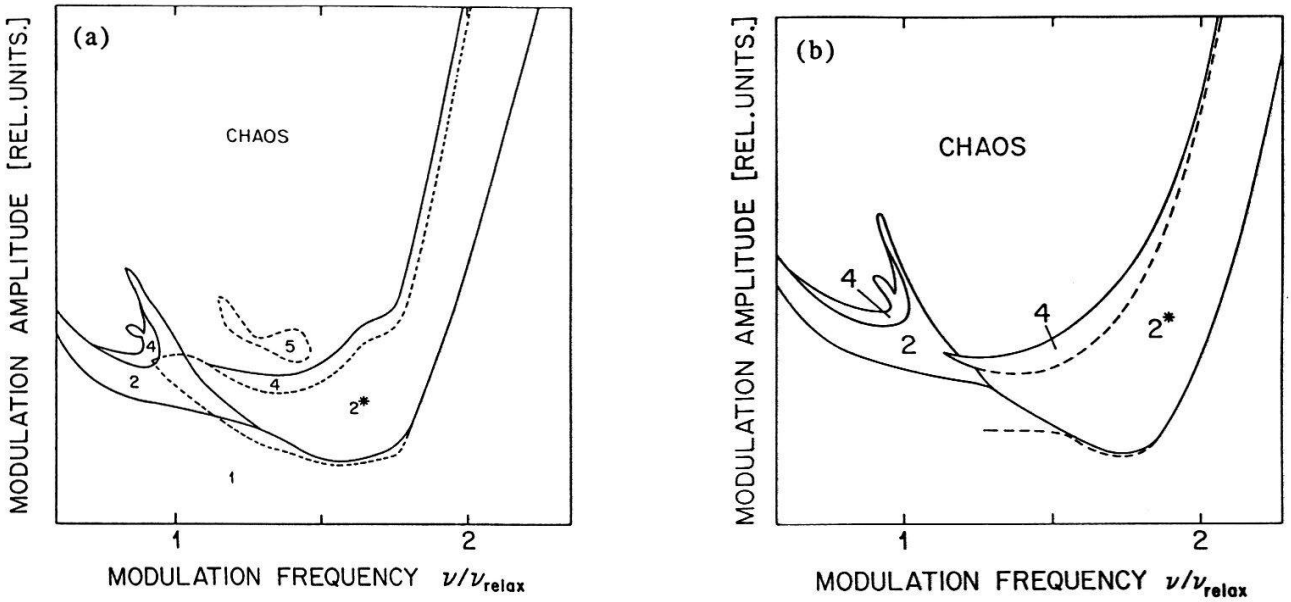

Fig. 2: Regions of existence of the main stable periodic orbits for the NMR-laser in the parameter space ω-A: (a) experiment, (b) EBL model. Two different period-2 (indicated as 2 and 2*) orbits coexist.

In conclusion, the correspondence between model and experiment is also shown by performing a sequence of other tests: comparision between bifurcation diagrams, Poincaré sections and sets of unstable periodic orbits [3].

3. REFERENCES

1. E. Brun, B. Derighetti, D. Meier, R. Holzner and M. Ravani. Observation of order and chaos in a nuclear spin-flip laser. *J. Opt. Soc. Am. B*, 2:156, 1985.

2. L. Flepp, R. Holzner, E. Brun and H.R. Moser. Noise and coherence in NMR-laser dynamics. *Proc. of 25th Congress Ampere*, Stuttgart 1990, (Springer Verlag).

3. M. Finardi, L. Flepp, R. Holzner, R. Badii, G. Broggi and E. Brun, see this issue.

HIERARCHICAL MODELLING OF NMR-LASER ATTRACTORS

M. Finardi*, L. Flepp•, R. Holzner•, R. Badii*, G. Broggi• and E. Brun•
* Paul-Scherrer Institut, LUS, 5232 Villigen PSI
• Physik Institut der Universität, Schönberggasse 9, 8001 Zurich

Abstract: We present a new method for characterizing and modelling experimental chaotic signals, based on a symbolic encoding of the trajectories in embedding space. We apply this procedure to a chaotic time-series generated by an NMR-laser. The validity of a proposed extension of the conventional Maxwell-Bloch equations is demonstrated by showing that they exhibit the same topological structure as the experimental data.

1 Introduction

The procedure for characterizing nonlinear flows and chaotic signals which has been presented in Refs.([1]) is applied to the response of an NMR-laser with a modulated parameter [2,3,4]. A scalar time-series consisting of $N = 8 \cdot 10^5$ 12-bits integers was recorded by sampling the transverse magnetization $M_t(t)$ with a frequency $\nu = 25/T$, where $T = 2\pi/\Omega$ is the period the external forcing term.

The aim of our analysis is the construction of a global model for the dynamics of the system under investigation which includes its most relevant topological features in a hierarchical order of importance. Once the phase-space has been reconstructed by embedding the time-series in a suitable E-dimensional space, relevant dynamical invariants (unstable periodic orbits) are identified by looking at portions of the trajectory which return close to the initial point within a given accuracy ε, in selected time-intervals (chosen around multiples of the period T of the external forcing). The precision ε with which the recurrent orbits shadow the actually periodic ones has been chosen to be proportional to $\sqrt{E}$ and to the local "density" of the points in phase space, and the results have been checked to be consistent throughout the physically meaningful range for E. We have constructed Poincaré sections Σ, by considering embedded points which lie 25 time units apart from each other. Since this procedure can only be applied for externally forced systems, we checked the result against a more general method of construction which also works in the autonomous case. The identification of all unstable periodic orbits, up to a given order, has allowed us to construct an approximation to the generating partition and to map the original continuous flow onto a subshift on a symbolic sequence $S = s_1 s_2 \ldots$. The symbolic

dynamics has been described by a hierarchy of Markov models which records the admissible orbit-to-orbit transitions and reproduces the statistical properties of the actual system with increasing precision.

A straightforward application of the Newton method has allowed us to locate the periodic orbits of the differential model [4].

2 Numerical Results

All unstable periodic cycles up to order 9 have been extracted both from experimental time-series (in embedding spaces of dimension E between 6 and 16) and from the model. Their intersection points with the Poincaré section Σ have then been assigned a different symbolic labelling through a binary partition $\mathcal{D} = \{\Delta_0, \Delta_1\}$. Since a generating partition associates a unique phase-space point to each infinitely long symbolic sequence (among which are the periodic ones), the partition $\mathcal{D}$ is a good approximation to a generating one, since it distinguishes all periodic points up to order nine. Of course, separating periodic points is a necessary but, in general, not sufficient condition for $\mathcal{D}$ to be generating.

The analysis of the symbolic dynamics has been carried out with the unfolding method of Refs.([1]). All points belonging to the subset Δ_0 of the Poincaré section are mapped into Δ_1 in one iteration: the string 00 is the only forbidden sequence, up to the largest investigated sequence length. Therefore, the most compact description of the dynamics is given by full binary tree over the two primitive words $w_1 = 1$, $w_2 = 01$ for both experiment and model. The unstable limit cycle have the following encodings: w_1, w_2, w_2w_1, $w_2w_1^2$, $w_2^2w_1$, $w_2w_1^3$, $w_2^2w_1^2$, $w_2w_1^4$, $w_2^2w_1^3$, $w_2w_1^5$, $w_2^3w_1^2$, $w_2^2w_1^4$, $w_2w_1^6$, $w_2^2w_1^5$, $w_2w_1^7$, where w^n denotes the n-th repetition of word w.

The full coincidence of measured and numerical data shows that the model agrees very well with the experimental observation, up to the available resolution. A more detailed description of the dynamics and of the metric invariants [1] will be presented elsewhere.[4]

References

[1] (a) R. Badii, Europhys. Lett. **13**, 599 (1990); (b) R. Badii, M. Finardi and G. Broggi "Unfolding Complexity and Modelling Asymptotic Scaling Behaviour", in *Chaos, Order and Patterns*, P. Cvitanović et al. Eds., Plenum, New York (1991);

[2] P. Boesiger,E. Brun and D. Meier, Phys.Rev.Lett. **38**, 602 (1977).

[3] E. Brun, B. Derighetti, D. Meier, R. Holzner and M. Ravani, J.Opt.Soc.Am. **B2**, 156 (1985).

[4] L. Flepp, R. Holzner, E. Brun, M. Finardi and R. Badii, (a) to be published; (b) this issue.

Wave Breaking and -Turbulence on the Surface of Superfluid Helium

Peter W. Egolf, Swiss Federal Laboratories for Materials Testing and Research CH-8600 Dübendorf, Switzerland
Daniel A. Weiss, Max-Planck-Institut für Strömungsforschung, D-W-3400 Göttingen, Germany
Jørgen L. Olsen, Swiss Federal Institute of Technology, Physics Departement CH-8093 Zürich, Switzerland

Asymptotic chaotic time behaviour of surface waves on superfluid helium II, is discussed. The investigations of the corresponding spatial patterns show a periodic breaking of the waves at the free liquid boundary. This implies the occurrence of turbulent phenomena. An important advantage of studying turbulence in a superfluid is outlined and explained in terms of experimental observations.

Surface waves on superfluid helium II driven by standing second sound waves in the bulk of the fluid [1] show a Hopf instability and a transition to turbulent motion at higher excitations [2]. This can clearly be observed, when the surface is photographed with short exposure times (figure 1).

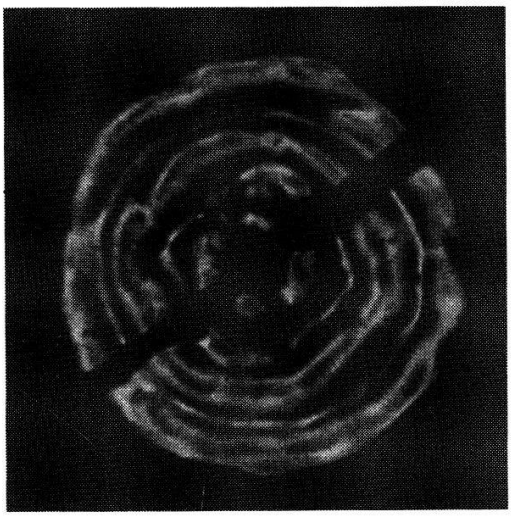

Figure 1: Wave breaking

Wave number of second sound: $k_2 = 1020\ m^{-1}$.
Temperature T=1.58 K.
Exposure time: 1/1000 s.
For the driving intensity of second sound see reference [7].

More or less distinct circle-like structures alternate with very cloudy looking broad patterns. Some further photographs, taken without a change of control parameters, show interchanged positions of these two types of different structures. This can be explained by a periodic building up of waves and breaking of the wave crests.

In research on turbulent phenomena energy-cascade models have become very familiar. Well-known is the Kolmogorov-Obukhov model [3] for fully developed turbulence. It states that the energy contained between the wave numbers k and k+dk is proportional to $k^{-5/3}$. Nowadays there are several theore-

tical predictions of scaling exponents for a broad range of turbulent phenomena [4,5]. S.J. Putterman has recently calculated a $f^{-3/2}$- dependence for the frequency spectrum of weak turbulence in the capillary regime (oral communication).

a)

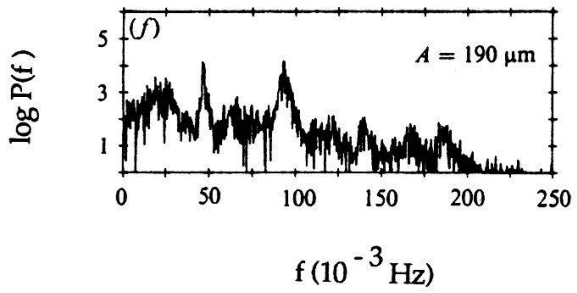

b)

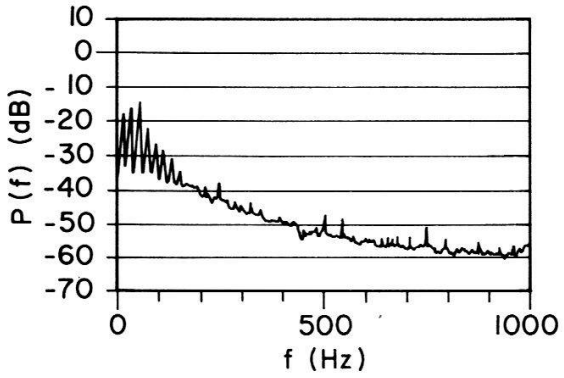

Figure 2: Power spectra

The power spectra of turbulent fluid motion (figure 2a, from ref. [6]) and of second sound induced superfluid motion (figure 2b).

A denotes the amplitude of vibration of a cylindrical vessel containing water and oscillating with a frequency of 16.05 Hz.

In such models energy is expected to be transferred into the system at low wave numbers (first region). In a second domain nonlinearities transport energy from large to small scale structures. It is assumed that this happens in a reversible manner. In a high wave number regime, finally, small structures loose (turbulent) kinetic energy due to molecular friction. In a superfluid with very low viscosity this third region occurs at very high wave numbers and therefore the second domain, where nonlinear interactions are present, is very wide. That is the reason why it is more appropriate to measure such scaling behaviour in a superfluid (figure 2b) than in a normal fluid. Figure 2a shows the power spectrum of water motion in a vibrating tank [6].

References

[1] J.L. Olsen, 1985, J. Low Temp. Phys. **61**, 17
[2] P.W. Egolf, J.L. Olsen, B. Röhricht and D.A. Weiss, 1991, Proc. of the 19th Int. Conf. on Low Temp Physics, Physica B **169**, 217
[3] A.N. Kolmogorov, 1941, Dokl. Acad. Sci. URSS **30**, 301
[4] O.M. Phillips, 1977, Dynamics of the Upper Ocean (Cambridge University Press)
[5] V.E. Zakharov, 1984, Handbook of Plasma Physics/M.N. Rosenbluth and R.Z. Sagdeev, volume 2 (Elsevier, New York)
[6] S. Ciliberto and J.P. Gollub, 1985, J. Fluid Mech. **158**, 381
[7] P.W. Egolf, 1990, PhD thesis, ETHZ, number 9290

SIMULATION OF ION BACKSCATTERING FROM ROUGH SURFACES

M. Wüest

Physikalisches Institut, University of Bern, 3012 Bern, Switzerland

A computer code was developed to simulate ion backscattering from rough surfaces. Simulations show that serrated or random surfaces of certain size and form can reduce scattering of 1 MeV protons drastically.

Electrostatic energy per charge analyzers exhibit the unwanted property that ions can hit the analyzer walls at glancing angles from where they undergo specular reflection. Such ions have a significant probability to pass trough the analyzer despite an incorrect E/Q-ratio and to produce ghost peaks in the detector. A surface coating with a rough surface morphology or a serrated surface significantly reduces specular reflection. A computer code has been developed to simulate backscattering from an amorphous target material with a rough surface in order to understand the influence of the surface roughness on the reduction of specular reflection.

Several ion transport procedures based on the Monte Carlo method have been reported [1]-[3]. Almost all models use a planar surface topology. Recently backscattering from rough surfaces of light ions in the energy range of up to several 100 eV was simulated [4], [5]. In this work the influence of macroscopic surface roughness on the backscattering of ions having an energy of 1 MeV is studied.

The computer program ISOS (Ion Scattering on Surfaces) is based on binary collisions. It is a 3D model for an amorphous target material. The nuclear and electronic energy losses are assumed to be independent from each other. The Ziegler-Biersack-Littmark universal potential with the universal screening length is employed to describe the nuclear energy loss [6]. The electronic energy loss is calculated according to the method given by [2]. The scattering integral is solved using the approximation of Biersack and Haggmark [1]. The maximum impact parameter b_{max} is determined such that the scattering angle in the center-of-mass system is greater than 0.1° and less or equal than the interatomic distance in the target material. The surface structure is single valued and determined by a mesh of triangles. Refraction of the ion path at the surface is taken into account. Comparison of ISOS with TRIM-90 [7] shows very good agreement for planar surfaces.

The number of particles backscattered divided by the total number of incident ions is the particle reflection coefficient R_N. In order to compare the particle reflection coefficient R_N of surfaces of different form and size the root mean square roughness R_q [8] is used.

The following surfaces are compared: The Plane surface is a flat surface without any surface structure. Saw1 and Saw2 are sawteeth surfaces with a maximum amplitude of 9 μm and 2.4 μm and a wavelength of 10 μm and 70 μm respectively. The forward base angles are 83.7° and 67° respectively. The rear base angles are 67° and 2° respectively. Mesh1 is a mesh structure with square holes, a maximum amplitude of 9 μm and a wavelength of 4 μm. The bar width is 1 μm. Random1 is a random surface with a maximum amplitude of 4.5 μm.

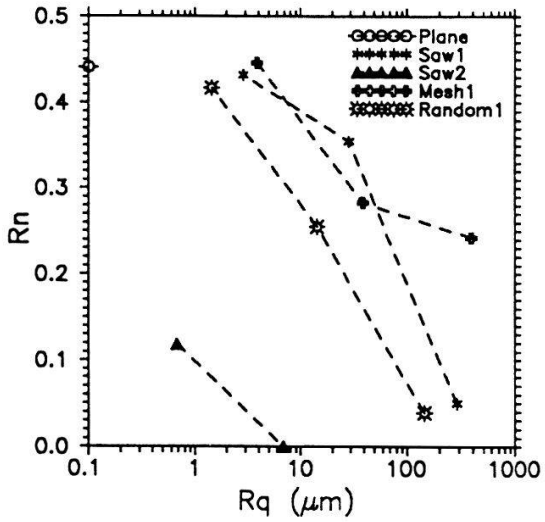

Figure 1: Particle reflection coefficient as function of the root mean square roughness R_q. The surface structures given in the text are also scaled by a factor of 10 and 100 and connected by a line to guide the eye.

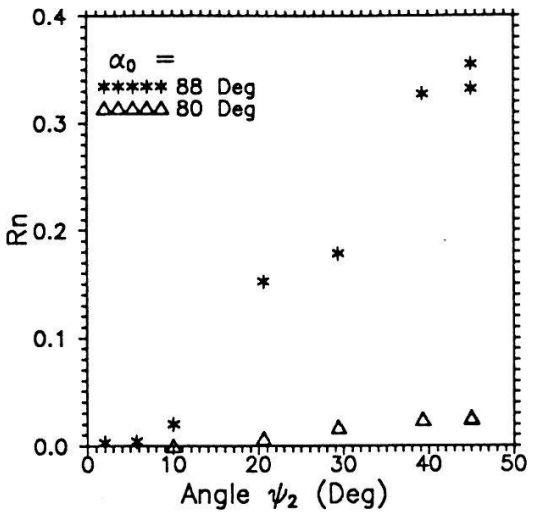

Figure 2: Particle reflection coefficient as function of the rear base angle of serrated surfaces for two different incidence angle α_0. All sawteeth have the same amplitude (9 μm) and same forward base angle (83.7°).

The calculations shown in Fig. 1 and 2 are for 1000 protons of 1 MeV incident energy hitting the surface at an incident angle $\alpha_0 = 88°$ relative to the global surface normal. The target material is copper of density $8.92 \cdot 10^3$ kg/m^3. The number of particles backscattered can be significantly reduced by the presence of a surface structure (cf. Fig. 1). The sawtooth surface Saw2 has the best reduction in particle reflection of the surfaces shown. Particle reflection of sawteeth surfaces is dependent on the rear base angle (cf. Fig. 2).

References

[1] J. P. Biersack and L. H. Haggmark, Nucl. Instr. and Meth., **174**, 257 (1980).

[2] J. F. Ziegler, J. P. Biersack and U. Littmark, *The Stopping and Range of Ions in Solids* (Pergamon Press, New York, 1985).

[3] M. T. Robinson and I. M. Torrens, Phys. Rev. B, **9**, 5008 (1974).

[4] N. N. Koborov, V. A. Kurnaev and V. M. Sotnikov, J. Nucl. Mater., **128/129**, 691 (1984).

[5] D. N. Ruzic and H. K. Chiu, J. Nucl. Mater., **162-164**, 904 (1989).

[6] J. P. Biersack and J. F. Ziegler, in *Ion Implantation Techniques*, edited by H. Ryssel and H. Glawischnig, Springer Series in Electrophysics Vol. 10 (Springer Verlag, Berlin, 1982).

[7] The program is available from J.F. Ziegler, IBM-Research, Yorktown NY 10598 USA.

[8] D. J. Whitehouse, P. Vanherck, W. de Bruin and C. A. van Luttervelt, Annals of the CIRP, **23**, 265 (1974).

Calculation of the molecular final states of tritium–containing alkanes

S. Schafroth, S. Vogel and P. F. Meier

Physik-Institut der Universität Zürich-Irchel, CH–8057 Zürich

In the Zurich neutrino experiment a β–source consisting of tritium–containing alkanes is used. To determine the mass of the $\bar{\nu}_e$ it is essential to know the energy which, after the decay of the tritium, is deposited in the daughter molecule. Excited states of and transition probabilities into the daughter molecule were calculated using Hartree–Fock procedures. Some results for propane ($CH_3 - CHT - CH_3$) are presented.

Tritium–containing alkanes are carbohydrates of the type C_nH_{2n+2}, where some of the hydrogen atoms have been replaced by tritium. Smaller chains ($n = 1 \ldots 4$) with one tritium atom are used to model longer chains with several tritium atoms, which are used as β–source for the measurement of the mass of the electron antineutrino [1] from the endpoint of the β–spectrum. Therefore the endpoint region around $E_{max} = 18.6$keV plays an essential role. A finite neutrino mass would lead to small deviations of the β–spectrum from the one for $m_{\nu_e} = 0$. Since the upper limit of m_{ν_e} is about 20eV, it is important to know how much energy is deposited in the daughter molecule, because it is of the same magnitude.

In the beta decay, the tritium–containing molecule RT transforms into a singly positively charged molecule with a helium nucleus replacing the original tritium nucleus. This happens in such a short time that the new ground state energy can be calculated assuming an instantaneous change of the nuclear charge from $Z = 1$ to $Z = 2$. The electronic structure relaxes leading to a lower energy of the daughter molecule RHe^+. The change of the Hamiltonian is given by:

$$\Delta H = H_T - H_{He^+} = \sum_i \frac{e^2}{|\vec{R}_T - \vec{r}_i|} - \sum_I \frac{Z_I e^2}{|\vec{R}_T - \vec{r}_I|},$$

where i labels the electrons and I the nuclei. This leads to an instantaneous change of energy $\overline{\Delta E} = \langle \Psi_0(RT)|\Delta H|\Psi_0(RT)\rangle$. Since this expression also represents the electrostatic potential at the site of the decaying tritium atom, it is possible to calculate the value of $\overline{\Delta E}$ with one of the usual *Quantum Chemistry Programs* [2].

A separate program was developed to calculate the transition probability W_{00} to the ground state of the daughter molecule. This probability is given by $|\langle \Psi_0(RT)|\Psi_0(RHe^+)\rangle|^2$, where $|\Psi_0(RT)\rangle$ and $|\Psi_0(RHe^+)\rangle$ represent the ground state for the parent and daughter molecule respectively [3].

Because the virtual orbitals of a Hartree–Fock calculation for N electrons are more appropriate for an $N+1$ electron system, they have to be optimized. The calculation of excited states (single excitations) at the Hartree–Fock level can be done by means of the method of

Ref. [4]. By a suitable modification of the Fock operator one obtains a new set of virtual orbitals from which the excited states, $|\Psi_n(RHe^+)\rangle$, and their energies can be calculated and also the corresponding transition probabilities $W_{0n} = |\langle\Psi_0(RT)|\Psi_n(RHe^+)\rangle|^2$.

Here only results of calculations on *T-Propane* are represented. The geometry was defined by covalent radii, tetrahedral angles and using staggered conformation. The values are shown in Table 1. Calculations on longer chains show essentially the same behavior.

The spectra (W_{0n} versus excitation energy) are all very similar. The transition to the ground state of the daughter molecule has the highest probability (about 60%). The majority of the other states lie between 20–40eV and around 60eV with about 35% probability. Most of the missing fraction (5–6%) is due to double and multiple excitations.

Basis	$\overline{\Delta E}$ [eV]	$\overline{\Delta E^*}$ [eV]	W_{00}	$\sum_{n\neq 0} W_{0n}$
4-31G	30.8135	19.9646	0.5978	0.3415
DZ	30.6829	19.9782	0.5970	0.3420
DZP	31.0638	19.9455	0.6038	0.3374
TZ	30.7373	20.1033	0.5956	0.3427
TZP	31.0802	20.0435	0.6029	0.3380

Table 1: Results for T-Propane ($CH_3 - CHT - CH_3$): Instantaneous energy change $\overline{\Delta E}$, average excitation energy $\overline{\Delta E^*}$ and ground state transition probability W_{00}. $\sum_{n\neq 0} W_{0n}$ is the sum over all calculated single electron excitations.

The basis sets mentioned above in the Table are given by the following expressions, where for each atom the type of functions and their number are indicated:

4-31G: [3s2p(C)/2s(H)/4s(T and He)]
DZ: [4s2p(C)/2s(H)/4s(T and He)] DZP: [4s2p1d(C)/2s1p(H)/4s2p(T and He)]
TZ: [5s3p(C)/3s(H)/6s(T and He)] TZP: [5s3p1d(C)/3s1p(H)/6s2p(T and He)]

Basis sets on T and He are a combination of basis sets for H and He in order to have the same basis for the RT and RHe^+ molecule.

The addition of a polarization function to the basis set (i.e. DZ → DZP and TZ → TZP) leads to a more significant change of the results than the use of a bigger basis set of the same quality.

In conclusion we have calculated the transition probabilities and excitation energies encountered in the β–decay of tritium–containing alkanes, extending the results of Kaplan et al. to longer chains. Furthermore we investigated the basis set dependencies of these quantities.

References

[1] M. Fritschi, Dissertation, Phil. Fak. II der Universität Zürich, 1990.
[2] M. Dupuis, HONDO-8 from MOTECC-89, 1989.
[3] I. G. Kaplan and V. N. Smutny, Adv. in Quant. Chem., 19 (1988), 289-348.
[4] S. Huzinaga and C. Arnau, J. of Chem. Phys., 54 (1971) 1948-1951.

LADS, EIN UNIVERSELLER 4π DETEKTOR FÜR DIE UNTERSUCHUNG DER $\pi^{+/-}$ STREUUNG UND ABSORPTION

M. Wildi, Univertsität Basel, für die LADS Kollaboration

Recent measurments on light nuclei showed π absorption modes, where more than 2, mainly 3 nucleons participate. In order to study these multinucleon modes in more detail LADS (**L**arge **A**cceptance **D**etector **S**ystem) was built at PSI. For calibration purpose the well known process $\pi^+ D \rightarrow pp$ was measured at 2 energies (T_π= 121 MeV and 165 MeV). The main components of the detector,of the high pressure gas target and of the data acquisition are discussed. First results from the calibration are presented.

Der totale Wirkungsquerschnitt der Wechselwirkung der π mit Kernen enthält folgende Komponenten : $\sigma_{tot} = \sigma_{el} + \sigma_{inel} + \sigma_{CEX} + \sigma_{abs} + \sigma_{rad}$, (elastisch, inelastisch, Ladungsaustausch, Absorption, Strahlungsreaktionen) Trägt man den Absorptionsquerschnitt als Funktion der Kernladungszahl A auf, so sieht man, dass für Kerne mit A>4 die Daten sehr gut mit einer exponentiellen Funktion beschrieben werden können. Dies gilt aber nicht für die leichtesten Kerne. Diese Differenz hat Anlass für viele Spekulationen gegeben.
Experimente Mitte der 80 iger Jahre haben gezeigt, dass es neben der 2 Nukleon Absorption (2NA), auch echte 3N Absorption gibt. Um diese oder kompliziertere Reaktionen eingehend studieren zu können, wurde 1989, nach einer 1 1/2 jährigen Planungsphase mit dem Bau von LADS am Paul Scherrer Institut (PSI) begonnen.
Um die Daten wirklich interpretieren zu können, ist es notwendig, dass man die Energien und Impulse aller beteiligten Teilchen misst. Dies kann man nur erreichen, indem die Akzeptanz des Detektors den gesamten Raumwinkel einschliesst.
Der Detektor (Fig. 1) besteht hauptsächlich aus zwei Teilen. Zur Energiemessung werden Szintillatoren aus Plastik verwendet. Die Winkel der auslaufenden geladenen Teilchen werden von zwei Drahtkammer gemessen. Teilchenidentifikation erfolgt einerseits mittels einer ΔE-E Messung, andererseits wird die Flugzeit bestimmt und, wie im ersten Fall, gegen die Gesamtenergie aufgetragen. Die zweite Methode ist auch für Neutronen geeignet ist.
Die Szintillatoren sind in drei Gruppe aufgeteilt, der Zylinder und die beiden End Caps, welche den Strahl beim Ein- und dem Austritt umschliessen. Die

Szintillatoren sind in 28, bzw. 14 Sektoren gruppiert. LADS deckt ca. 98.5 % von 4π ab.

Aus geometrischen Gründen war die Installation eines flüssigen Heliumtargets unmöglich. Es wurde daher ein Hochdruckbehälter aus Kohlenstofffasern entwickelt, welcher auf der Innenseite mit einer Cu/Ag Legierung belegt war. Der Arbeitsdruck beträgt um 100 bar, bei einer Wandstärke von nur 0.5 mm. Trotz dieser minimalen Dicken ist das Target heliumdicht. Während der Dauer des Experimentes hat dieses Target ausgezeichnet funkioniert.

Die Daten wurden mit eigenen Programmen, welche auf TANDEM basieren, ausgelesen und auf Band beschrieben.

Die gemessene Enerieauflösung hat mit 2.2 MeV für 100 MeV Protonen die Erwartungen erfüllt (Fig. 2). In den Figuren 3 und 4 sind erste Ergenisse der $\pi^+ D \rightarrow pp$ bzw. $\pi^{+12}\mathrm{C} \rightarrow pp$ dargestellt. Bei Figur 3 handelt sich es um die Energie von Proton 1 aufgetragen gegen Energie von Proton 2. In Figur 4 ist die Winkelkorrelationen der beiden auslaufenden Protonen zu sehen.

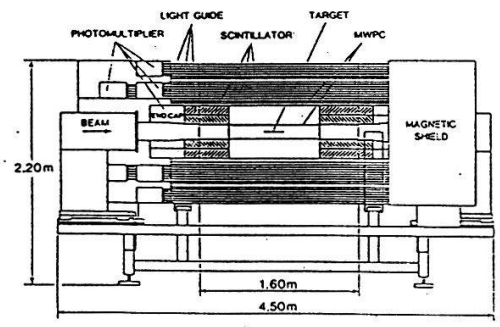

Fig. 1 LADS Längsschnitt

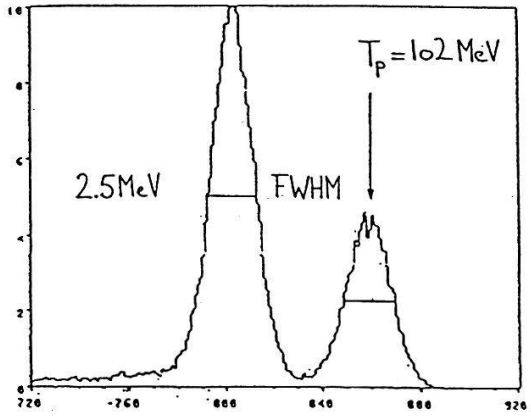

Fig. 2 Energieauflösung

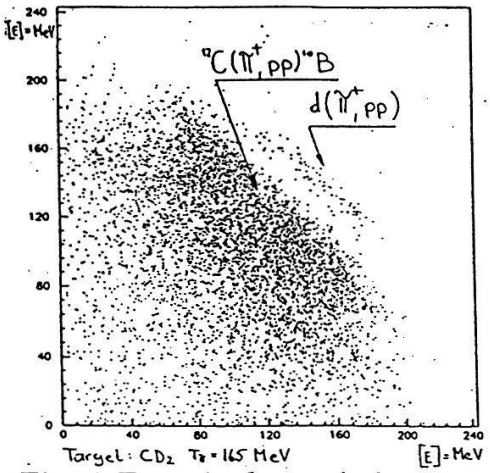

Fig. 3 Energie der emittierten p

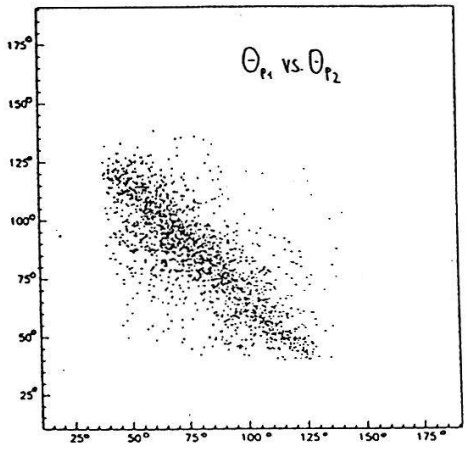

Fig. 4 Winkelkorellation 2p Endzustände

MUON TRANSFER IN H_2 + SO_2 GAS MIXTURES

F. Mulhauser, R. Jacot-Guillarmod, C. Piller, L.A. Schaller, L. Schellenberg and H. Schneuwly

Institut de Physique de l'Université, CH-1700 Fribourg, Switzerland

Abstract : The muon transfer rate to the SO_2 molecule determined from the analysis of the sulphur x-ray time spectra is well reproduced in seven different H_2 +SO_2 gas mixtures. In particular, the unexpected time structure of the oxygen x-rays is present in all measurements.

The muonic hydrogen atom is neutral and so small that it penetrates easily through the electron clouds of atoms and transfers its muon onto muon-atomic orbits of other nuclei. The muon transfer rate can be determined by analysing he time structure of the muonic x-rays following the transfer process [1,2].

In the case of H_2 +SO_2 gas mixtures, the muon can be transferred either to sulphur or to oxygen atoms. The analysis of the time structure of these sulphur and oxygen x-rays should yield the same lifetime of the μp atom in the ground state and the same normalized transfer rate to sulphur dioxide. Actually, one observes a single exponential time structure for the sulphur x-rays and an unexpected double exponential structure for the oxygen x-rays [2,3,4].

During the recent years, we performed seven measurements of muon transfer to sulphur dioxide. The experimental setups were the same [2], but the SO_2 concentration (from 0.2% to 0.6%) and the total pressure of the mixture (from 10 to 15 bar) were varied.

The time distributions of the muonic sulphur x-rays of the Lyman series as well as of the Balmer series had in all mixtures the structure of a single exponential. From their time constant, called τ_S, which corresponds to the lifetime of the μp atom in the ground state, one determines the transfer rate to sulphur dioxide, Λ_{SO_2}, normalized to the atomic density of liquid hydrogen (cf. Table). This reduced transfer rate is well reproduced and its value agrees with theoretical estimates [1,6].

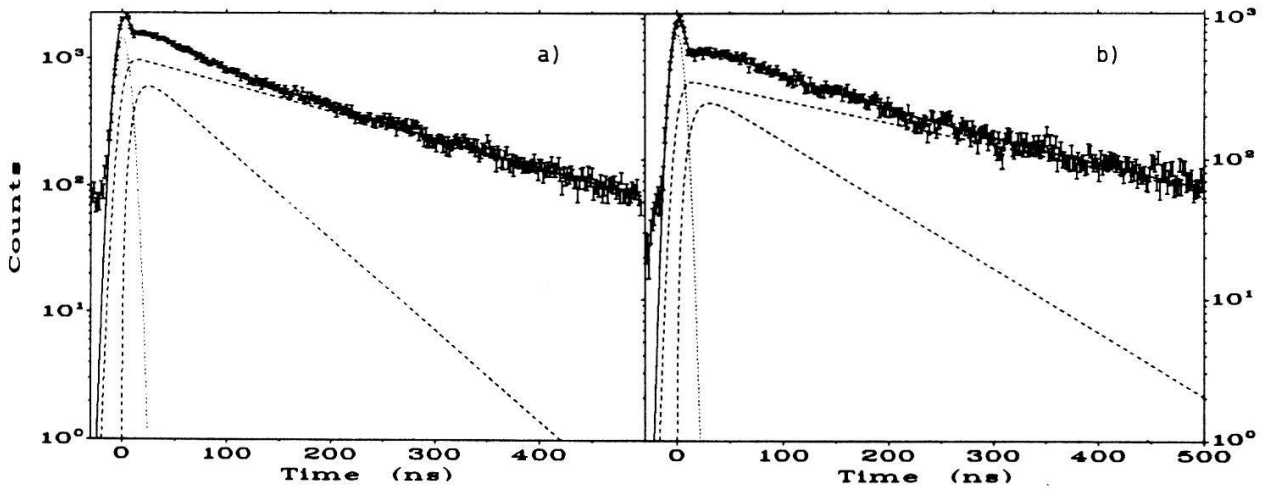

Fig. Measured and fitted time spectra of the muonic 2p-1s transition of oxygen, from the H_2 + 0.2% SO_2 mixture at a) 15 bar and b) 10 bar.

In all seven mixtures, the time spectra of all four observed muonic oxygen x-ray transitions of the Lyman series showed comparable double exponential structures, as illustrated in the figure. The longer of the two decay times, τ_1, corresponded always to the μp lifetime, τ_S, measured in the sulphur time spectra. To fit the oxygen time spectra, a function with three time constants was employed [1], where τ_1 was set equal to τ_S, τ_2 was the shorter of the two decay times and τ_r a rise time. We observed that the fits were better when one used a longer τ_r time for the mixtures at lower pressure (10 bar).

The intensity patterns of both muonic oxygen x-rays, i.e.those corresponding to the normal time constant, $\tau_1 = \tau_S$, and those corresponding to the unexpected time constant τ_2 , are identical and agree with the theoretical prediction for muon transfer from μp atoms in the ground state [7]. Thus, if τ_2 is the lifetime of another kind of μp atom, a corresponding transfer rate Λ^*_O may be determined (cf. Table). One sees that these normalized rates Λ^*_O are the same for given SO_2 concentrations, but decrease with increasing concentration.

The intensity of the unexpected time component of the muonic oxygen x-rays is not small. It does not depend upon the total pressure, but increases with SO_2 concentration from about 25% to more than 50% of the intensity of the normal component (cf. Table).

The problem of the two μp lifetimes, measured in the oxygen x-ray time spectra, and consequently of two or more muon transfer rates, may be correlated with the problem of several classes of muon transfer rates to argon, neon and helium [1,4].

Table : Time constants and reduced transfer rates, measured in H_2 + SO_2 gas mixtures with different SO_2 concentrations and at different pressures. The quoted values result from preliminary analyses.

Conc.	Pressure [bar]	τ_r [ns]	τ_S [ns]	Λ_{SO_2} [$\cdot 10^{11}$ s^{-1}]	τ_2 [ns]	Λ^*_O [$\cdot 10^{11}$ s^{-1}]	Intensity Ratio	Ref.
0.2%	15	7	198.5	2.52	62.7	4.33	.26	[5]
0.2%	10	11	275.7	2.54	91.1	4.27	.29	[5]
0.2%	15	7	198.0	2.55	64.8	4.21	.26	
0.4%	15	9.5	107.0	2.51	40.9	3.42	.42	[1]
0.4%	13.3	9.5	119.0	2.51	48.0	3.25	.52	[1]
0.6%	15	9.5	69.8	2.60	31.9	2.91	.57	
0.6%	10	11	103.0	2.55	45.1	3.01	.56	

[1] F.Mulhauser, H.Schneuwly, R.Jacot-Guillarmod, C.Piller, L.A.Schaller and L.Schellenberg, Muon Catalyzed Fusion **4**, 365 (1989)

[2] R.Jacot-Guillarmod, F Bienz, M.Boschung, C.Piller, L.A.Schaller, L.Schellenberg, H.Schneuwly, W. Reichart and G. Torelli, Phys. Rev. **A.38**, 6151 (1988).

[3] H.Schneuwly, R.Jacot-Guillarmod, F.Mulhauser, P.Oberson, C.Piller and L.Schellenberg, Phys. Lett. **A 132**, 335 (1988)

[4] H.Schneuwly, Muon Catalyzed Fusion **4**, 87 (1989)

[5] F.Mulhauser, R.Jacot-Guillarmod, C.Piller, L.A.Schaller, L.Schellenberg and H.Schneuwly, Hel. Phys. Acta **63**, 545 (1990)

[6] S.S. Gershtein, Sov. Phys.-JETP **16**, 501 (1963)

[7] G. Holzwarth, H.J. Pfeiffer, Z. Phys. **272**, 311 (1975)

NEW CHARGE TRANSFER RATES FROM MUONIC PROTIUM TO NEON

H. Schneuwly*, R. Jacot-Guillarmod*, M. Mallinger**, F. Mulhauser*, C. Piller*, L.A. Schaller* and L. Schellenberg*

*Institut de physique de l'Université, CH-1700 Fribourg, Switzerland
**Centre Universitaire du Luxembourg, Luxembourg

Abstract: New measurements of muon transfer rates to neon confirm only partially earlier ones. This suggests that the phenomena observed in neon might be of the same kind as the unexpected and yet unexplained charge transfer phenomena observed in sulphur dioxide.

During the recent years, we have performed, under very different experimental conditions of pressure and relative concentration, five measurements of the muon transfer rate from hydrogen to argon, and obtained transfer rates, normalized to liquid hydrogen density, that agreed well with each other [1,2]. In seven muon transfer measurements in $H_2 + SO_2$ gas mixtures with various SO_2 concentrations, we observed always the same single exponential time structure of the muonic sulphur x-rays and a more complex time structure of the muonic oxygen x-rays. The muon transfer rates to the SO_2 molecule, deduced from the time distributions of the muonic sulphur x-rays agree all seven with each other [3,4].

From the fact that all these transfer rates have been reproduced under very different conditions of pressure and relative concentration seems to indicate that the dependences of the transfer rates upon the corresponding parameters are well understood, and that background or impurity problems are small.

In our first measurement of muon transfer from muonic protium to neon, we observed a double-exponential structure in the time distribution of the muonic neon x-rays of all five transitions of the Lyman series [5]. These time distributions were similar to those observed in the muonic oxygen x-rays of $H_2 + SO_2$ gas mixtures except that the intensity of the faster of the two time components was only 4%. The muon transfer rate deduced from the faster component agreed well with the rate measured twenty years ago in a triple gas mixture [6]. The slower of the two components yielded an unexpectedly low transfer rate which was about twenty times smaller. This very small transfer rate has however been confirmed in a measurement performed with a triple gas mixture $H_2 + Ne + Ar$ [5]. The time structure method as well as the intensity method, which has also been used by Alberigi Quaranta et al.[6], yielded both this very small transfer rate (cf. Table).

In a second measurement, performed about six months later in a binary gas mixture H_2 + 1.4%Ne, a reduced muon transfer rate higher by about 30% was found (cf. Table), i.e. a transfer rate significantly different from the preceding ones [7]. In addition, the time distributions of the muonic x-rays did no more show the double-exponential structure observed in the first measurement.

Again about six months later and still at the μE4 muon channel of PSI in Villigen, we performed new measurements by using two $H_2 + Ne$ gas mixtures at 15 bar pressure with neon concentrations differing by a factor of about three. The two reduced muon transfer rates to neon obtained without any background correction (as usual) agree well with each other (cf. Table). These new transfer rates agree also with the one measured six months before, but disagree with the ones obtained in the first measurements.

The measurement of the H_2 + 0.7%Ne mixture in December 1989 should have been nothing else than a repetition of the measurement of the H_2 + 0.7%Ne mixture performed one year before. Another measurement, H_2 + 0.2%SO_2, was repeated in parallel and its results have been well reproduced. Why the neon data were not reproduced, is presently an open question.

A more detailed analysis of the four binary neon gas mixtures $H_2 + Ne$ investigated has shown that, whereas in the H_2 + 2%Ne mixture no delayed muonic oxygen x-rays were detected, the three other mixtures contained such oxygen x-rays. However, their intensity does never exceed 10% of the neon intensity. The correction of the transfer rates to neon would, therefore, never

exceed 10%, such that the discrepancies remain. In addition, the time structure of these muonic oxygen x-rays is not always compatible with the time structure of the muonic neon x-rays, such that the corrections were questionable. The uncertainties of the rates listed in the Table take possible corrections due to impurities into account.

Table : Experimental (reduced) muon transfer rates from muonic protium to neon.

Year	Ref.	pressure [atm]	mixture	Λ_{pNe} [$\cdot 10^{11}$ s^{-1}]
1967	[6]	26	H_2 + Ne + Xe	1.16(28)
1990	[5]	15	H_2 + 0.7%Ne	1.15(20)
1990	[5]	15	H_2 + 0.7%Ne	0.062(4)
1990	[5]	15	H_2 + Ne + Ar	0.058(48)
1990	[5]	15	H_2 + Ne + Ar	0.062(5)
1990	[7]	15	H_2 + 1.4%Ne	0.079(4)
1991	present	15	H_2 + 2%Ne	0.081(5)
1991	present	15	H_2 + 0.7%Ne	0.084(8)

The situation created by the incompatibilities among the measured muon transfer rates to neon and the fact, that the data measured in the two H_2 + 0.7%Ne gas mixtures are not reproduced, is uncomfortable. However, comparable problems exist for the muon transfer rates to argon and helium, where most of the data were produced by different experimental groups. The puzzling questions raised by the muon transfer data to sulphur dioxide [2,4,8] seem to increase the complexity of the situation, but might be at the same time a clue to find an explanation for the problem as a whole [9].

[1] R. Jacot-Guillarmod, F. Bienz, M. Boschung, C. Piller, L.A. Schaller, L. Schellenberg, H. Schneuwly, W. Reichart ad G. Torelli, Phys. Rev. **A38**, 6151 (1988).
[2] R. Jacot-Guillarmod, F. Mulhauser, C. Piller, L.A. Schaller, L. Schellenberg and H. Schneuwly, in: *E M Cascade and Chemistry of Exotic Atoms*, eds. L.M. Simons, D. Horváth and G. Torelli (Plenum Press, New York, 1990) in press.
[3] H. Schneuwly, R. Jacot-Guillarmod, F. Mulhauser, P. Oberson, C. Piller and L. Schellenberg, Phys. Lett. A **132**, 335 (1988).
[4] F. Mulhauser R. Jacot-Guillarmod, C. Piller, L.A. Schaller, L. Schellenberg and H. Schneuwly, in: *E M Cascade and Chemistry of Exotic Atoms*, eds. L.M. Simons, D. Horváth and G. Torelli (Plenum Press, New York, 1990) in press.
[5] R. Jacot-Guillarmod, F. Mulhauser, C. Piller and H. Schneuwly, Phys. Rev. Lett. **65**, 709 (1990).
[6] A. Alberigi Quaranta, A. Bertin, A. Matone, F. Palmonari, A. Placci, P. Dalpiaz, G. Torelli and E. Zavattini, Nuovo Cimento B47, 92 (1967).
[7] R. Jacot-Guillarmod,F. Mulhauser, C. Piller, L.A. Schaller, L. Schellenberg and H. Schneuwly, Helv. Phys. Acta **64**, 205 (1991)
[8] F. Mulhauser, H. Schneuwly, R. Jacot-Guillarmod, C. Piller, L.A. Schaller and L. Schellenberg, Muon Cat. Fusion **4**, 365 (1989).
[9] H. Schneuwly, Muon Cat. Fusion **4**, 87 (1989).

Teilchenemission von ^{232}Th(α, f) bei E_α=120 MeV

S. Kopecky, P. Riehs und M. Vana

Institut für Kernphysik der Technischen Universität Wien, Österreich

H.H. Müller, P. Schober, S. Steiner und D. Zimmermann

Physikinstitut der Universität Zürich, Schweiz

In our experiment the energy of protons in coincidence with fission fragments was measured. The reduction of the emission barrier can be explained by the help of a deformation of the fissioning nucleus. The deformation parameter is β=0.64. It is possible to define the minimal life-time of the fissioning nucleus as 3-5.10^{-20}s. Proton emission is understood in terms of cascade model calculations which gave datailed information of neutron emission.

Das Experiment führten wir am Injektor Cyclotron I des Paul Scherrer Institutes durch. Zur Erlangung der Anregungsenergie standen uns ^{4}He mit einer Laborenergie von 120 MeV zur Verfügung. Als Target wählten wir 120μg/cm^2 ^{232}Th, das auf einer Kohlenstoffolie von 20μg/cm^2 aufgedampft war.

Die Spaltbruchstücke wurden durch zwei Si-Detektoren von 60μm Dicke detektiert, die links und rechts des einfallenden Strahles unter 45° in Rückwärtsrichtung montiert waren. Die Teilchenidentifikation erfolgte durch ein Teleskop, das aus drei Si-Detektoren mit 250μm, 2mm und 1mm Dicke bestand und unter 30° in Vorwärtsrichtung befestig war.

Bei dem Vergleich der experimentellen Daten mit einer Modellrechnung, diese Rechnung wurde mit dem Programm ALICE [1] durchgeführt, zeigte sich, daß mit keinem Parametersatz des statistischen Modells befriedigende Übereinstimmung erzielt werden konnte. So lag die Coulombbarriere des Experimentes stets tiefer als jene der Rechnung.

Eine mögliche Erklärung dieser Verschiebung kann in einer Deformation des Emitters gesucht werden. Diese Deformation berücksichtigen wir indem wir die Transmissionskoeffizienten der inversen Reaktion zu tieferen Energien verschieben. Das sollte in erster Näherung die Reduktion des mittleren elektrostatischen Potentials an der Kernoberfläche widerspiegeln. Bei einer Parametrisierung der Kernoberfläche mit

$$R(\theta) = R_0(1 + (\frac{5}{4\pi})^{1/2}\beta P_2(\cos\theta))$$

ergab sich bei einer Verschiebung der Koeffizienten um ca. 1 MeV ein Deformationsparameter β=0.64.

Das Verhältnis des effektiven Trägheitsmoments des deformierten Kernes zu jenem einer volumsgleichen Kugel beträgt $I_k/I_{eff} \simeq 0.8$. Nach Vandenbosch [2] entspricht dieser Wert ungefähr jenem, den ein Kern mit Z^2/A=35.9 am Sattelpunkt besitzt.

Ein Vergleich dieses Deformationsparamters mit Literaturdaten [3], welche alle aus Alphaspektren gewonnen wurden, zeigt, daß unser Wert im oberen Bereich dieser Werte der Schwerionenphysik liegt. Der Grund dafür könnte einerseits in den unterschiedlichen Vorgangsweisen der

Bestimmung des Deformationsparameters oder in der Gewinnung dieses Parameters aus Spektren verschiedener Teilchenarten zu suchen sein. Nach unserer Meinung ist die unterschiedliche Teilchensorte ein Hauptgrund für diese Differenz, wie schon La Rana et al. [4] gezeigt haben. Wobei wir die Ursache dieser Unterschiede in der zeitlichen Entwicklung des Kernes vermuten, doch müßten um dies bestätigen zu können weitere Messungen und Modellrechnungen, welche die zeitliche Entwicklung des Kernes in Betracht ziehen können, durchgeführt werden.

Die Coulombbarriere wird durch die Deformation je nach Emissionsrichtung unterschiedlich sein. Wir erwarten, daß in Richtung der Deformationsachse wegen der größeren Entfernung vom Ladungsschwerpunkt diese Barriere erniedrigt und in Richtung der kürzeren Halbachse erhöht wird. Wenn man nun annimmt, daß die Deformationsachse die Flugrichtung der Fragmente widergibt, werden wir erwarten, daß die Teilchenspektren, die in Koinzidenz mit je einem Spaltdetektor aufgenommen wurden, unterschiedliche Form aufweisen. Durch die Eigendrehung des Emitters sollten diese Differenzen der Spektrenform gemildert werden. Aus der Stärke dieser Verminderung wollen wir daher auf eine Lebensdauer des emittierenden Systems schließen. Die Messung zeigt, daß keine Unterschiede zwischen den beiden Spektren zu sehen sind. Unter Berücksichtigung der Eigendrehung mit $J_{rms}=30.5\hbar$ und der Deformation mit $\beta=0.64$ ergibt sich eine mindeste Lebensdauer des spaltenden Systems von $3\text{-}5.10^{-20}$s.

Ein weiteres Ergebniss unserer Modellrechnung betrifft die Neutronen. Nach Hinde et al. [5] würden wir für ein Compoundsystem wie das unsere ungefähr 5-6 Neutronen vor der Spaltung und 3-4 nach der Spaltung erwarten. Unsere Rechnung jedoch ergab ca. 0.75 Prefission und 11 Postfission Neutronen. Wenn man annimmt, daß für das statistische Modell der Sattelpunkt als entscheidend betrachtet wird, kann man vermuten, daß der größte Teil der Neutronenemission während der Entwicklung vom Sattel- zum Abtrennpunkt erfolgen sollte. Wir können daher vermuten, daß auf die einzelnen Entwicklungsphasen folgende Anzahl von Neutronen emittiert werden.

Vom Erreichen des thermischen Gleichgewichts bis Sattelpunkt	0.75
Zwischen Sattelpunkt und Abtrennpunkt	4-5
Von den Fragmenten	3-4

Wir würden daher aus diesen Werten ebenfalls auf eine lange Entwicklungszeit vom Sattel- zum Abtrennpunkt schließen. Doch auch um diese Vermutung zu bestärken müßten weitere Messungen und Rechnungen durchgeführt werden.

Diese Arbeit wurde vom Fonds zur Förderung der wissenschaftlichen Forschung und vom Schweizerischen Nationalfonds unterstützt.

Referenzen

[1] M. Blann and H.K. Vonach, Phys. Rev C **28**, 1475 (1983)
[2] R. Vandenbosch and J.R. Huizenga, *Nuclear Fission* (Academic Press, New York 1973)
[3] J.M. Alexander, D. Guerreau and L.C. Vaz, Z. Phys. A **305**, 313 (1982)
[4] G. La Rana et al., Phys. Rev. C **35**, 373 (1987)
[5] D. J. Hinde et al., Nucl. Phys. **A452**, 550 (1986)

Massenverteilung bei ^{232}Th(α, f), E_α=120 MeV

M. Vana und P. Riehs

Institut für Kernphysik der Technischen Universität Wien, Österreich

The mass distribution of 120 MeV α induced fission has been measured and calculated with a statistical theory, using the assumption, that the relative probability of different fission modes is proportional to the product of the level densities of the two fragments (P. Fong). Agreement with experimental results is achieved with modified level density parameters a. A maximum shift of 4 MeV^{-1} for a was necessary, and it is not yet clear, whether this modification is compatible with calculations for fissioning nuclei of different masses.

Die Messung wurde in Zusammenarbeit mit dem Physik Institut der Universität Zürich am Paul Scherrer Institut (PSI) durchgeführt. Es wurde eine mit 120 μg/cm^2 ^{232}Th bedampfte Kohlenstoffolie als Target mit α-Teilchen einer kinetischen Energie von 120 MeV beschossen. Um die Spaltbruchstücke zu messen, wurden zwei N_2-gekühlte Spaltdetektoren, Silizium-Detektoren mit 60 μm Dicke und 300 mm^2 aktiver Fläche, die zu beiden Seiten des einfallenden Strahles in Rückwärtsrichtung unter 45° mit 60 mm Abstand vom Target montiert waren, verwendet. Für die Bruchstücke ergab sich eine mittlere kinetische Energie von 85.9 ±1.1 MeV mit einer Halbwertsbreite von 40.2 MeV und einer relativen statistischen Schwankung der Zählrate bei mittlerer Energie von 3.10^{-3}. Hierbei ist eine von einer gaußförmigen Kurve abweichende Asymetrie bei hohen Energien, die bis jetzt noch nicht erklärt werden konnte, auffällig.

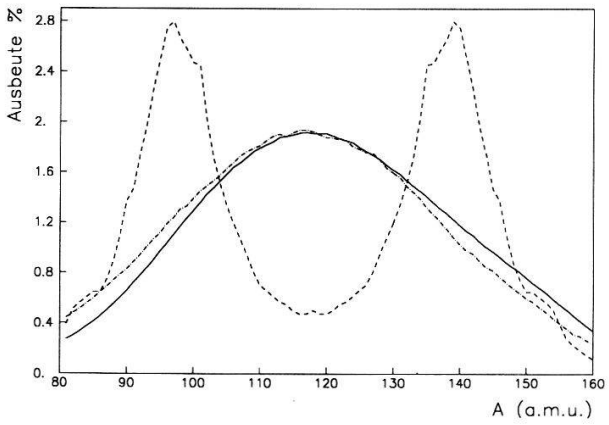

Figur 1. Massenverteilung
——— Experiment $d\sigma/d\Omega$= 1500.2 ±237.3 mb/sr
· · · · Rechnung mit neuen a $d\sigma/d\Omega$=1374.5 mb/sr
- - - - Rechnung mit Werten von Fong [1]

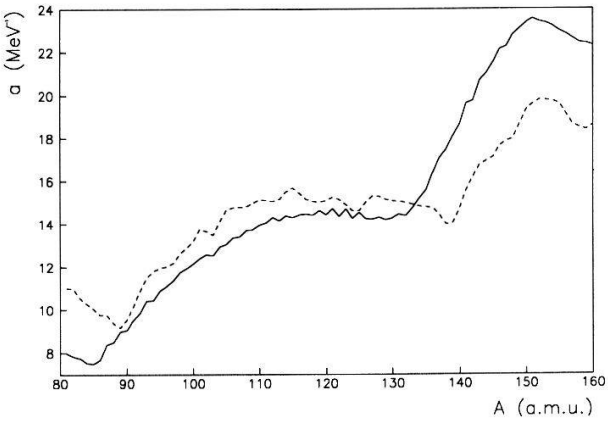

Figur 2. Niveaudichteparameter
——— errechnete a
- - - - a von 0-10 MeV [4]

Das Ziel war, die gemessene Massenverteilung mittels des statistischen Modells unter den Annahmen von Fong et. alt. [1] zu erklären. Es wird postuliert, daß die Wahrscheinlichkeit der Aufteilung in zwei bestimmte Spaltbruchstücke proportional zum Produkt der Niveaudichten dieser beiden Teilchen bei den inneren Energien der Bruchstücke E_1, E_2, die sich aus der

Energiebilanz unter Berücksichtigung der totalen kinetischen Energie der Fragmente ergibt, ist. Um die Dichte der Quantenzustände des Compoundkerns zu erhalten benötigen wir die Niveaudichten. Diese können für beide Fragmente mit Hilfe des Fermigas-Modells berechnet werden, wobei die Anregungsenergie und die jeweiligen Niveaudichteparameter erforderlich sind.

Befinden sich die beiden Kerne im thermischen Kontakt, so läßt sich die gesamte Quantenzustandsdichte des Systems der beiden Spaltbruchstücke mit $E=E_1+E_2$ als

$$\Omega(E) = \int_0^E c_1(E_1)\exp(2\sqrt{a_1 E_1})c_2(E-E_1)\exp(2\sqrt{a_2(E-E_1)}\,dE_1$$

schreiben. Hieraus läßt sich nun durch näherungsweise analytische, oder durch numerische Integration die Massenverteilung berechnen. Beides geschah mittels eines Ergänzungsprogrammes zum Programm ALICE [2], das die Teilchenemission und den energieabhängigen Spaltwirkungsquerschnitt berechnet. Als Eingabeparameter benötigt man die Massen des Compoundkernes und der Spaltbruchstücke [3], die totale kinetische Energie der Spaltbruchstücke, die von früheren Messungen genommen wurde, und die Deformationsenergie [1], sodaß man erhält:

$$E = M^*(A,Z) - M(A_1,Z_1) - M(A_2,Z_2) - TKE - D.$$

P. Fong et. alt. [1] führten diese Berechnung, die reproduziert werden konnten, für Spaltung mit thermischen Neutronen durch, wobei der Niveaudichteparameter a als linear in A angenommen wurde und die Massen nach einem korrigierten Tröpfchenmodell berechnet wurden. Bei höheren Anregungsenergien wird die Massenverteilung allerdings mit diesen Eingabeparametern nicht richtig wiedergegeben (Fig.1). Im Widerspruch zur Messung bleibt bei symetrischer Massenaufteilung das für die asymetrische Spaltung charakteristische Tal erhalten.

Um die richtige symetrische Verteilung bei hohen Energien zu erlangen benötigt man sicher Niveaudichteparameter in Abhähgigkeit von der Masse, die derart strukturiert sind, daß das Tal bei asymetrischer Spaltung, das auf Schaleneffekten beruht, mit höher werdender Energie ausgeglichen wird. Hierbei wurde die Rechnung mit experimentell bestimmten Massen [3] und a- und Δ-Werten [4] durchgeführt. Wobei diese a-Werte für 0-10 MeV gemessen sind. Da das Ergebnis nicht befriedigend ist, liegt der Schluß nahe, falls man das Modell nicht verwerfen will, a zu variieren (eine Variation von Δ ändert wenig und wurde daher unterlassen). Mit den in Fig. 2 dargestellten a(A) konnte mit der Messung gute Übereinstimmung erziehlt werden (siehe Fig. 1). Wobei natürlich nur die Form der Kurve und nicht deren absolute Höhe bestimmt werden kann. Eine mögliche Interpretation wäre, daß die Niveaudichteparameter a von der Anregungsenergie abhängig sind, die angesichts des einfachen Fermigas-Modells, das die Energieabhängigkeit nicht vollständig wiedergibt, durchaus plausibel erscheint. Es wird aber Gegenstand weiterer Rechnungen sein, zu verifizieren, ob dieses Modell mit geänderten Niveaudichteparameter für andere Compoundkerne den physikalischen Tatsachen entspricht.

Diese Arbeit wurde vom Fonds zur Förderung der wissenschaftlichen Forschung unterstützt.

Referenzen

[1] P. Fong, *Statistical theory of nuclear fission*, (Gordon and Breach, Science Publishers, New York, 1969)

[2] M. Blann, H. K. Vonach, Phys. Rev. C **28**, 1475 (1983)

[3] A. Wapstra, G. Audi, R. Hoekstra, Atomic Data and Nucl. Data Tables **39**, 289 (1988)

[4] W. Dilg, W. Schantl, H. Vonach, M. Uhl, Nucl. Phys. **A217**, 269 (1973)

A variational study of the two-impurity Anderson model

L. C. Andreani[a] and H. Beck[b]

[a]IRRMA, PHB-Ecublens, 1015 Lausanne, Switzerland
[b]Institute de Physique, Université de Neuchâtel, 2000 Neuchâtel, Switzerland

The competition between Kondo effect and RKKY interaction is studied by a variational solution of the Anderson model with two spin-$\frac{1}{2}$ impurities. For an interimpurity distance R smaller than $\sim 2.5(k_F)^{-1}$, strong FM correlations between the two impurity spins are found, and the physics becomes that of a spin-1 Kondo effect. For $R > 2.5(k_F)^{-1}$ the physics depends on the ratio between RKKY coupling and Kondo temperature T_K. No anomalous behavior of the susceptibility is found.

The indirect magnetic interaction in rare earth compounds is known to exhibit unusual features when the Kondo effect is present. Magnetically ordered Ce and Yb compounds often have a reduced saturation moment, which indicates a partial Kondo screening. This competition between Kondo effect and RKKY interaction is believed to be described by the Anderson model for localized magnetic impurities hybridized with band electrons.

In this work we report on a zero-temperature study of the Anderson model with two spin-$\frac{1}{2}$ impurities coupled to a free-electron band. The model Hamiltonian is given by

$$H = \sum_{\mathbf{k}\sigma} \varepsilon_k c^\dagger_{\mathbf{k}\sigma} c_{\mathbf{k}\sigma} + \varepsilon_f \sum_{i=1}^{2} \sum_{\sigma} f^\dagger_{i\sigma} f_{i\sigma} + V \sum_{i=1}^{2} \sum_{\mathbf{k}\sigma} (e^{i\mathbf{k}\cdot\mathbf{R}_i} f^\dagger_{i\sigma} c_{\mathbf{k}\sigma} + \text{h.c.}) + U \sum_{i=1}^{2} f^\dagger_{i\uparrow} f_{i\uparrow} f^\dagger_{i\downarrow} f_{i\downarrow},$$

where the index $i = 1, 2$ labels the two impurities. We assume $U = \infty$.

The wavefunction in each spin subspace is expanded variationally in a basis which allows for holes in the Fermi sea but does not include electrons above the Fermi level. The basis includes the states with two holes in the band, which are crucial for the correlated Kondo effect. The RKKY interaction is reproduced by adding a term $-J\mathbf{S}_1 \cdot \mathbf{S}_2$, where $\mathbf{S}_1, \mathbf{S}_2$ are the impurity spins. The neglected states produce mainly a renormalization of the model parameters. The linear equations arising from the variational Ansatz are solved numerically for the ground and excited states. The ground state is always found to have zero total spin.

The study of a finite-size "molecular" model [1] suggested that magnetic correlations between Kondo singlets might develop even if the RKKY coupling is much smaller than the Kondo temperature (which in the present model is given by $T_K = B\exp(\pi\varepsilon_f/(2\Gamma))$, where $\Gamma = \pi|V|^2\rho(\varepsilon_F)$ is the hybridization width and $-B$ is the bottom of the band measured from the Fermi energy). This is confirmed by the results of Fig. 1, where we show the ground-state spin correlation function $\langle \mathbf{S}_1 \cdot \mathbf{S}_2 \rangle$ when the RKKY interaction is set equal to zero. A critical distance $R_c \simeq 2.5(k_F)^{-1}$ is found, which separates two different regimes. For $R > R_c$, the impurity spins are only weakly correlated, with oscillations resembling those of the function $\sin(k_F R)/(k_F R)$. In this region, the binding energy is close to $-2T_K$. For $R < R_c$ instead the impurity spins have strong FM correlations. This is due to the fact that, for $R \to 0$, the screening clouds on the two impurities consist of a hole in the same partial wave state.

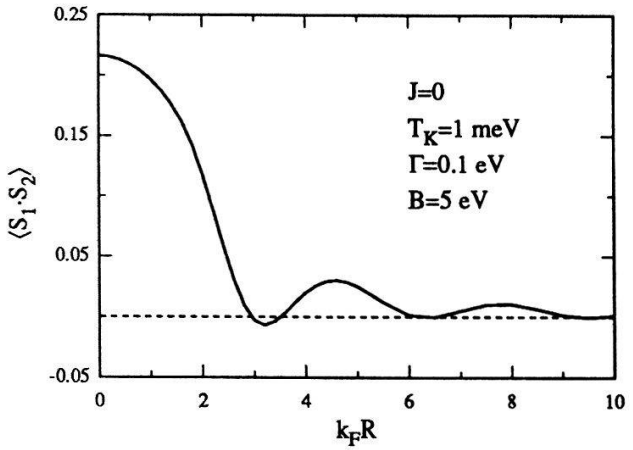

Fig. 1. - Spin correlation function as a function of interimpurity distance for $J = 0$.

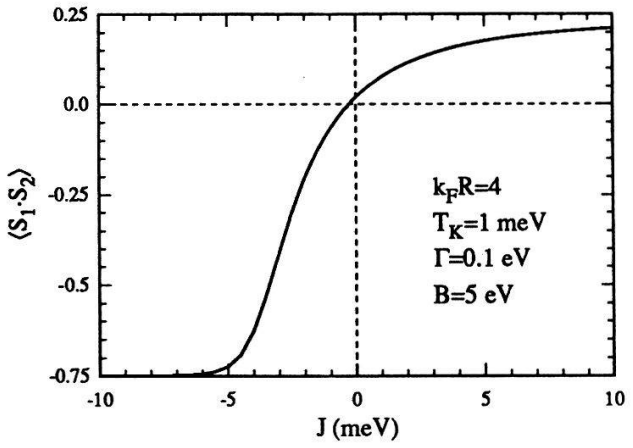

Fig. 2. - Spin correlation function as a function of RKKY coupling for $k_FR = 4$.

For $R \to 0$ the binding energy tends to $\delta = B\exp(\pi\varepsilon_f/(3\Gamma))$. This shows that the physics becomes that of a spin-1 Kondo effect with a characteristic energy $\delta \gg T_K$. This might stabilize the Kondo effect against the RKKY interaction in a Kondo lattice.

In Fig. 2 we show the spin correlation function as a function of RKKY coupling for $k_FR = 4$. We see that the behavior is governed by the ratio J/T_K. For $|J| \gg T_K$ the localized spins have strong magnetic correlations, which are either FM or AFM according to the sign of J. It is worth noticing that the curve of Fig. 2 is smooth, without abrupt transitions. The ground state evolves continuously from the case $J = 0$ to the limiting cases $J \gg T_K$ and $J \ll -T_K$. A curve very similar to Fig. 2 is calculated in the molecular model [1]. We find no singular behavior in the physical quantities (correlation functions, uniform and staggered susceptibility) for any ratio J/T_K. This agrees with the results of Ref. [2] but contradicts those of Ref. [3]. The regime $|J| \sim T_K$, in which the correlation function $\langle \mathbf{S}_1 \cdot \mathbf{S}_2 \rangle$ is intermediate between zero and the limiting values, can be interpreted as a magnetic state with reduced magnetic moments. The second-order transition to an ordered state can of course only be reproduced in a lattice of impurities.

In conclusion, the two-impurity Anderson model in the spin-fluctuation limit is characterized by a critical distance $R_c \simeq 2.5(k_F)^{-1}$. For $R > R_c$ the ground-state properties depend on the ratio J/T_K, yielding magnetism with reduced moments for $|J| \sim T_K$. For $R < R_c$ the RKKY interaction must be compared with a characteristic energy $\gg T_K$, which in the limit $R \to 0$ becomes that of a spin-1 Kondo effect. No singular behavior in the physical quantities is found for any ratio J/T_K.

References

[1] L. C. Andreani, S. Fraizzoli, and H. Beck, Solid State Commun. **77**, 635 (1991).

[2] T. Yanagisawa, J. Phys. Soc. Jpn. **60**, 29 (1991).

[3] B. A. Jones, C. M. Varma, and J. W. Wilkins, Phys. Rev. Lett. **61**, 125 (1988).

Disconnected Cluster Approach for Quantum Monte Carlo Simulations

Matthias Troyer, Fakher F. Assaad and *Diethelm Würtz*
Interdisziplinäres Projektzentrum für Supercomputing, ETH-Zürich
and Insitut für theoretische Physik, ETH-Zürich
CH-8092 Zürich, Switzerland

Abstract: We present a new and efficient disconnected cluster decomposition to perform Monte Carlo Simulations based on the Trotter-Suzuki method for 1-d quantum systems. As opposed to the normal checkerboard world line algorithm this mapping allows one to simulate models with interactions up to next nearest neighbours. Results are presented on the t-J and t-J-J' model. Those types of models are prototypes of strongly interacting fermion systems.

Exact solutions are not available for many of the interesting strongly correlated fermion systems. Perturbation theory and mean field theories fail to calculate properties of these systems. Therefore one has to use exact diagonalisation methods or efficient Monte Carlo techniques. One of the standard methods is the path integral formulation leading to the world line algorithm [1]. Within this approach we have found a new cluster decomposition of the Hamiltonian (figure 1) and a new set of moves to upgrade the world line configurations. For details see [3]. We have compared our decomposition to the standard checkerboard decomposition, which consists of disconnected bonds, for the t-J model [2]. The systematic $0(\Delta\tau^2)$-error arising from the discrete Trotter (time) axis is smaller than with the usual checkerboard decomposition (figure 2, $\Delta\tau$=inverse temperature / number of Trotter slices). This results in higher precision and shorter simulation times and makes the algorithm much more efficient.

We have used the cluster decomposition with the world line algorithm to simulate the one-dimensional t-J-J' model

$$H = -t \sum_{i,\ \sigma=\pm 1/2} \left(P c^{\dagger}_{i,\sigma} c_{i+1,\sigma} P + h.c. \right) + J \sum_i (\vec{S}_i \vec{S}_{i+1} - \frac{1}{4} n_i n_{i+1}) + \alpha J \sum_i (\vec{S}_i \vec{S}_{i+2} - \frac{1}{4} n_i n_{i+2}),$$

where the projector P prohibits double occupancy. The electrons on the lattice are allowed to hop between nearest neighbour sites. They are submitted to a nearest neighbour interaction with strength J, which is frustrated by a next nearest neighbour Heisenberg interaction with strength $J' = \alpha J$. At low values of J/t the model shows the same qualitative behaviour as the $t - J$ model (figure 3). There is a $4k_f$ charge peak and a $2k_f$ spin peak. With growing J/t these peaks are reduced and a cusp develops in the charge structure factor at $2k_f$. At higher values of J/t phase separation occurs. This can be seen by the divergence of the charge structure factors at long wavelengths. Near the phase boundary the system is not totally phase separated into a dimerised island of spins and a sea of holes, but there are still holes in the particle rich phase. The particle rich phase can be caricatured as a gas of next neighbour and next nearest neighbour bound pairs (the solid line in figure 3b is a least square fit of the data for $J/t = 3$ to this caricature). Our results favour the assumption that the model scales to the Tomonaga-Luttinger fixed point. There is a sign problem due to frustration. A low average sign leads to numerical problems due to cancellation. In figure 4 we have plotted the average sign for different values of the band filling ρ(=number of particles / lattice size) and J/t. The sign problem prohibits simulations in the high density region.

References
[1] M. Suzuki, Quantum Monte Carlo Methods, Springer Series in Solid-State Sciences 74
[2] F. F. Assaad and D. Würtz, ETH Preprint (1990), to appear in Phys. Rev. B ; M. Ogata, M. U. Luchini, S. Sorella and F. F. Assaad, ETH preprint (1990), to appear in Phys. Rev. Let.
[3] M. Troyer, Diplomarbeit ETH (1991)

We are grateful for stimulating conversations with T.M. Rice and M. Ogata.

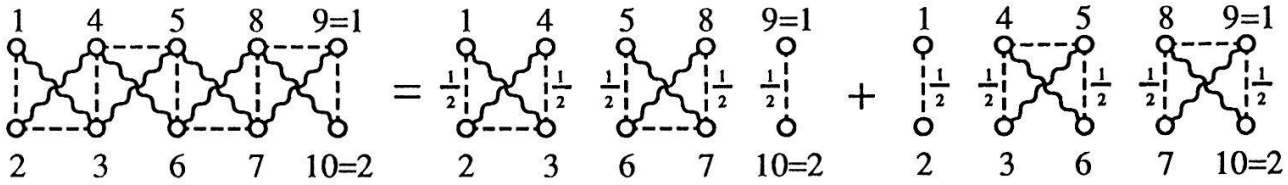

Figure 1

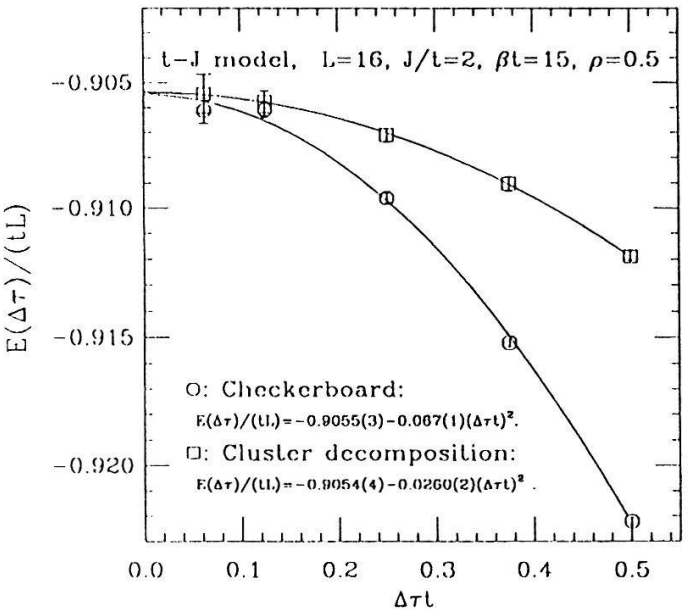

Figure 2

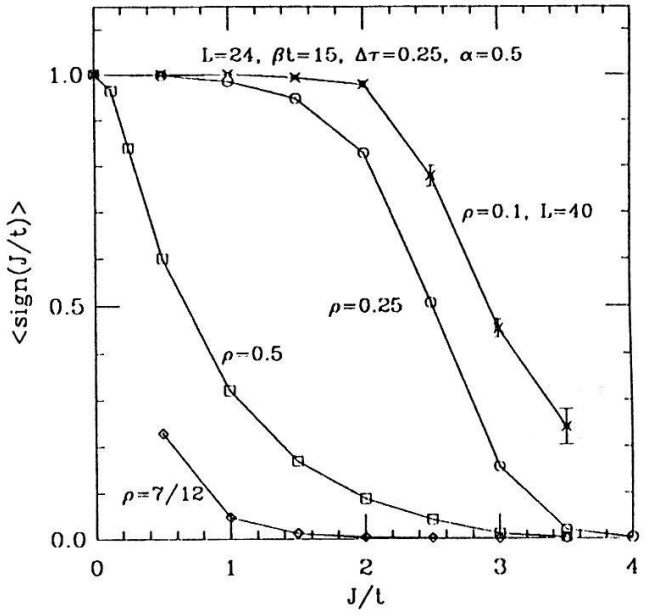

Figure 4

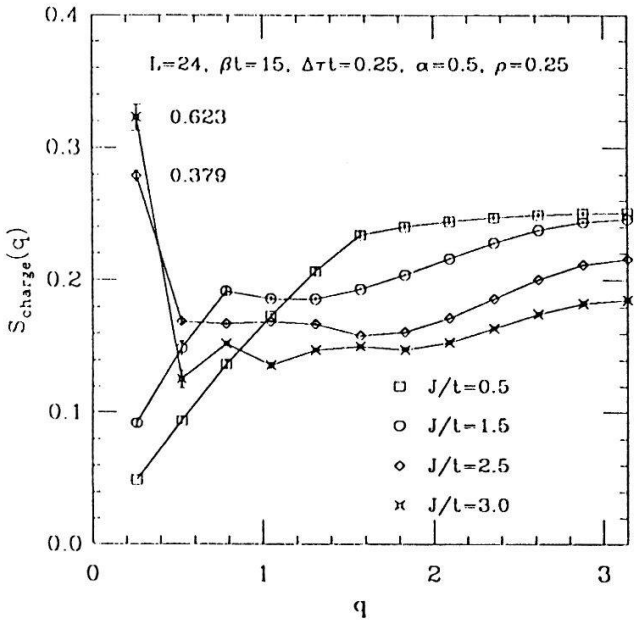

Figure 3a

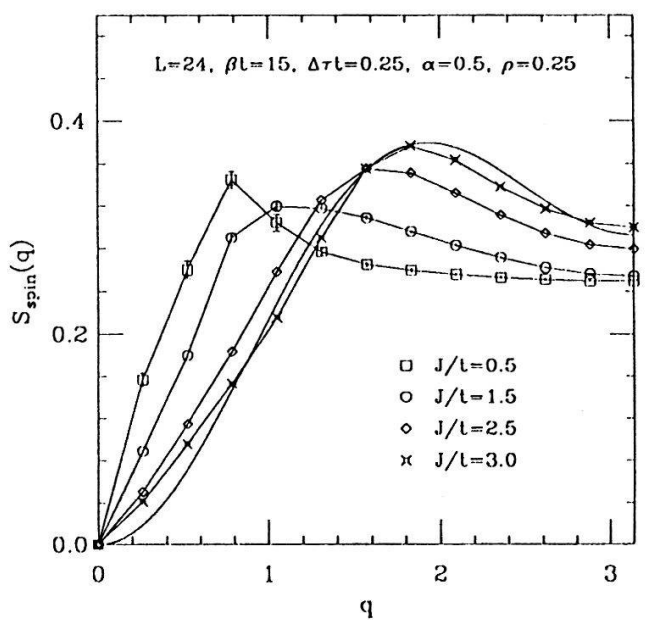

Figure 3b

A New Model on Turbulent Shear Flows

Peter W. Egolf

Swiss Federal Laboratories for Materials Testing and Research
Coordination of Building Energy Conservation Research
CH-8600 Dübendorf, Switzerland

Compared with established semi-empirical closure schemes a non-local theory describing the physics of turbulent momentum transport has some obvious advantages.

The mixing length theory of L. Prandtl [1] is probably the best known theory of practical significance for analytical calculations of fully developed turbulent shear flows. It leads to the following result for the tangential Reynolds stress

$$\rho \overline{u_2' u_1'} = - \varepsilon \frac{d\overline{u_1}}{dx_2} \qquad (1.1)$$

with an eddy viscosity given by

$$\varepsilon = \rho \ell^2 \left| \frac{d\overline{u_1}}{dx_2} \right| \qquad (1.2)$$

that contains the mixing length ℓ. Less-known is a later developed model, also proposed by Prandtl [2], with a somewhat different eddy viscosity

$$\varepsilon = \kappa \rho b (\overline{u_1}_{max} - \overline{u_1}_{min}) \qquad (1.3).$$

Instead of the small mixing length ℓ, now, the width b of the entire turbulent mixing zone appears. κ simply denotes a constant. H. Görtler [3] criticized that this eddy viscosity does not vanish at the boundary of the mixing zone. This may be one reason for the lack of success of this second model. Moreover, not long ago, P.S. Bernard and R.A. Handler [4] argued that one-point models, such as the gradient law, are found to be inherently unsuitable to describe turbulent momentum transport. Their work encouraged me to publish the following (galilei-invariant) mean gradient theory, which I have worked out four years ago.

In the new theory, instead of equation (1.1) and (1.3) we have

$$\rho \overline{u_2' u_1'} = - \kappa \rho \chi_2 \frac{db}{dx_1} (\overline{u_1} - \overline{u_1}_{min}) \frac{\overline{u_1}_{max} - \overline{u_1}}{x_{2\,max} - x_2} \qquad (2.1).$$

The choice of $\chi_2 \in \{b, x_2\}$ follows from symmetry arguments. Maximum quantities of the mean velocity are defined for all values of x_1

$$\overline{u_1}_{min} := \min_{x_1,x_2} \{ \overline{u_1}(x_1,x_2) \} \qquad \overline{u_1}_{max} = \overline{u_1}_{max}(x_1) := \max_{x_2} \{ \overline{u_1}(x_1,x_2) \} \qquad (2.2).$$

The quantities $x_{2\,max}$ are defined implicitly

$$\overline{u_1}(x_1,x_{2\,max}) := \overline{u_1}_{max}(x_1) \qquad (2.3).$$

Studying a wake flow behind a cylinder, we split the mean velocity $\overline{u_1}$ into the undisturbed flow velocity U_G and a small mean velocity disturbance u_1^* pointing upstream: $\overline{u_1}(x_1,x_2) = U_G - u_1^*(x_1,x_2)$. After a delicate limiting procedure ($x_{2\,max} = b$) and some algebraic operations we find

$$\frac{\overline{u_2' u_1'}}{U_G^2} = -\frac{1}{2}\,\frac{x_2}{x_1 + p}\,\frac{\overline{u_1^*}(x_1,x_2)}{U_G} \qquad (3.1).$$

The same result can be obtained by mass and momentum flux considerations [5].

Accounting to equations given in [5] and to the model (2.1) we also can calculate the mean-velocity distribution in the selfsimilar region of a round free jet. In the two limiting cases ($\overline{u_1} = U_G + \overline{u_1^*}$)

$$\frac{\overline{u_1^*}_{max}}{U_G} >> 1 \qquad \text{and} \qquad \frac{\overline{u_1^*}_{max}}{U_G} << 1 \qquad (3.2\,a/b),$$

separating $\overline{u_1^*} = \overline{u_1^*}_{max}(x_1)\, f_1(\eta)$, $\eta = \frac{x_2}{b}$, we obtain the differential equations ($' := \frac{d}{d\eta}$)

$$\eta f_1^2 f_1'' - 2\kappa f_1'^3 - 3\eta f_1 f_1'^2 - f_1^2 f_1' = 0 \qquad 2 f_1 + \eta f_1' + \kappa \frac{1}{\eta} f_1' = 0 \qquad (3.3\,a/b).$$

The solution of (3.3a) is (3.4a). It has been experimentally confirmed by H. Reichhardt [6]. Calculating u_2^* proves, that in the case b there is no entrainment.

$$f_1(\eta) = \exp\left(-\frac{1}{2\kappa}\eta^2\right) \qquad f_1(\eta) = \frac{\kappa}{\kappa + \eta^2} \qquad (3.4\,a/b).$$

A more detailed presentation of this model is planned. For encouragement I wish to thank M. Zimmermann.

References: [1] L. Prandtl, 1925, Z. Angew. Math. Mech. **5**, 136-138
[2] L. Prandtl, 1942, Z. Angew. Math. Mech. **22/5**, 241-243
[3] H. Görtler, 1942, Z. Angew. Math. Mech. **22/5**, 244-254
[4] P.S. Bernard and R.A Handler, 1990, J. Fluid Mech. **220**, 99-124
[5] J.O. Hinze, 1975, Turbulence, 2nd edition, Mc Graw Hill
[6] H. Reichhardt, 1942, VDI-Forschungsheft 414, B/13

Probability Densities for the Noisy Feigenbaum Scenario

P. Reimann and P. Talkner

Paul Scherrer Institut, CH-5232 Villigen and
Institut für Physik, Klingelbergstr. 82, CH-4056 Basel

The influence of noise on the period doubling route to chaos is the subject of many investigations concernig e.g. scaling of the Lyapunov exponent and the appearance of a bifurcation gap at the onset of chaos [1] as well as the determination of the escape rate from attracors [2].

The standard equation describing the noisy Feigenbaum route to chaos reads

$$x_{n+1} = f_r(x_n) + \sqrt{\epsilon}\,\xi_n \tag{1}$$

We assume independent identically distributed Gaussian noise $P(\xi_n \in [\xi, \xi + d\xi]) = \pi^{-1/2} \cdot \exp\{-\xi^2\}\, d\xi$ of strenth ϵ. Further on $f_r(x)$ is supposed to map some finite iterval $I_r = [-x_r, x_r]$ onto itself possessing a single quadratic maximum in I_r and to depend smoothly on the control parameter r. Thus after fixing the of scales by $f_0(0) = 1$ and $f_1(0) = x_1$ the functions $f_r(x)$ are uniquely determined through the recursion

$$f_{\delta \cdot r}(x) = -\alpha\, f_r(f_r(-x/\alpha)) \tag{2}$$

where $\alpha = 2.5029...$ and $\delta = 4.6692...$ are the universal Feigenbaum constants. This definition yields a suitably idealized version of the logistic map with qualitatively identical features. Outside I_r the detais of $f_r(x)$ are of no relevance to our problem and one may simply think of a constant continuation there.

We are interested in the properties of the stationary probability density $W_\epsilon^r(x)$ [3],[4] satisfying

$$W_\epsilon^r(x) = \frac{1}{\sqrt{\pi\epsilon}} \int_{-\infty}^{+\infty} dy\; W_\epsilon^r(y)\; e^{-(x - f_r(y))^2/\epsilon} \tag{3}$$

in the case of weak noise $\epsilon << 1$. Using the WKB ansatz [3],[4]

$$W_\epsilon^r(x) = Z_\epsilon^r(x)\, e^{-\phi_r(x)/\epsilon} \tag{4}$$

an approximate renormalization treatment of Eq.(3) yields the following results

$$2\, W_\epsilon^r(x) = \alpha\, W_{\lambda \cdot \epsilon}^{\delta \cdot r}(-\alpha\, x) \qquad \text{and} \qquad W_\epsilon^r(x) = W_\epsilon^r(f_r(x)) \cdot |f_r'(x)| \tag{5}$$

where the first equation holds for $-x_r < x < x_{\delta \cdot r}/\alpha$ and the second for $x_{\delta \cdot r}/\alpha < x < x_r$. Here $\lambda = 43.81...$ denotes a third universal constant [1] and $x_{\delta \cdot r}/\alpha$ equals the unstable fixed point of $f_r(x)$ in I_r which follows from (2). This scaling behavior of which certain aspects can be found in [1],[5] is compared with the result of a recently introduced numerical method [3] by which $\phi_r(x)$ and $Z_\epsilon^r(x)$ can separately be determined (see Fig.). We find deviations from (5) that depend on x and are rather small both for $\phi_r(x)$ and $Z_\epsilon^r(x)$.

Our renormalization procedure for the generalized potential $\phi_r(x)$ allows one to estimate these deviations analytically in good agreement with the numerical findings. Further one finds analytically some local properties of $\phi_r(x)$ and $Z_\epsilon^r(x)$ as e.g. the behavior of $\phi_r(x)$ in the vicinity of the attractor and the repellors as well as the location, heigth , and width of the most dominant peaks of $Z_\epsilon^r(x)$ [4].

Within the above described limitations the central result (5) is universal in the same sense as the deterministic Feigenbaum scenario: qualitatively it applies for other maps than $f_r(x)$ with quadratic maximum, and for nonvanishing multiplicative noise, too. For non-Gaussian but still white noise different values of the scaling parameter λ may appear.

Finally we note that the qualitative behavior of $\phi_r(x)$ is well understood from the fact that it is a Lyapunov function of the deterministic map $f_r(x)$ [4] and that it obeys the same scaling relation (5) as the probability density $W_\epsilon^r(x)$.

References

[1] J.Crutchfield, J.Farmer, B.Huberman, Phys. Rep. **92**, 45 (1982) and references therein.
[2] F.Arecchi, R.Badii, A.Politi, Phys. Lett. **103A**, 3 (1984); P.Beale, Phys. Rev. A **40**, 3998 (1989); J.Holtfort, W.Möhring, H.Vogel, Z. Phys. B **72**, 115 (1988).
[3] P.Talkner, P.Hänggi, E.Freidkin, D.Trautmann, J. Stat. Phys **48**, 231 (1987); P.Talkner and P.Hänggi in 'Noise in nonlinear dynamical systems', Vol. 2, edited by F.Moss and P.V.E.McClintock, Cambridge University Press 1989.
[4] P.Reimann, P.Talkner, Helv.Phys.Acta **36**, 845, 1990; P.Reimann, P.Talkner, to appear.
[5] R.Graham, A.Hamm, and T.Tél, preprint 1991.

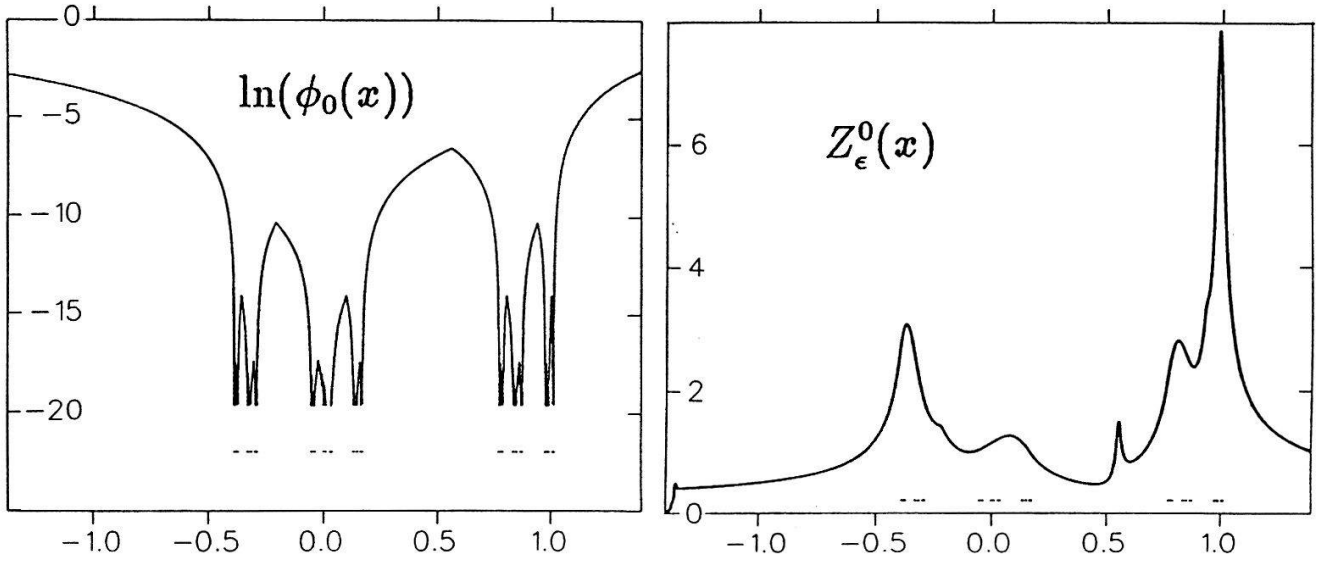

Figure: Logarithm of $\phi_0(x)$ and $Z_\epsilon^0(x)$ at the onset of chaos at $r = 0$ for $\epsilon = 4 \cdot 10^{-4}$. The Feigenbaum attractor is indicated above the x-axis. Deviations from Eq.(5) are beyond graphical resolution.

Signal Processing and Noise Reduction with Connectionist Networks

Claas de Groot and *Diethelm Würtz*
Interdisziplinäres Projektzentrum für Supercomputing, ETH-Zürich
CH-8092 Zürich, Switzerland

Abstract: We report on a parsimonious feedforward connectionist nets approach for the modeling and forecasting of time series. We investigate these nets on the sunspot data which can be considered a "yardstick" of judging new statistical methods. Our results show that the connectionist approach yields at least competitive results. As a second example we study the nets' capability of distinguishing "real" white noise from a (deterministic) mapping with similar properties. Again the nets show their ability to approximate the underlying mapping. This result may be seen as a nonstandard method of noise reduction.

Connectionist Networks (CN) of the "feedforward" type have recently been shown to be universal function approximators [1]. The simplest structures for which these theorems hold are nets with a single hidden layer and nonlinear (sigmoid) transfer functions in this hidden layer only. This theoretical result is accompanied by recent papers which showed experimentally the capabilities of relatively simple CN to approximate nonlinear mappings [2]. These findings encourage the application of CN in the field of (nonlinear) *time series analysis.* In order to examine the abilities of feedforward CN in this field we compared their performance in analysing and predicting the sunspot cycle to other linear as well as nonlinear models on these data. The analysis of sunspot data has a long tradition in the statistical literature. They are used as a "yardstick to compare and judge new statistical modeling and forecasting methods."[3] For our comparison we chose mainly nonlinear models from the literature since the underlying mechanism is generally believed to be nonlinear. Reference to the relevant papers is given in [4] where also a more detailed discussion can be found. Figures 1–3 show the performance of simple nets (25 weights) on the sunspot data in the various fields (see captions). The data for the comparison of the performance is given in table 1. One may conclude from these figures that the CN perform better on these data than the other models cited. Though this result is rather challenging we in fact are quite far apart from a real understanding of the nets' behaviour. Several design problems were solved by *heuristics* or (even worse) by *trial and error.* But our empirical approach showed that the number of parameters for a successful application to real world data may turn out to be comparatively small. We may therefore propose the *principle of parsimony.*

In order to investigate the capabilities of feedforward CN in a more systematic manner we also applied them to an artificial problem. The (fully developed) *logistic parabola* is known to show two characteristics of white noise: a flat spectrum and δ-autocorrelations. Since time series data are usually corrupted by "real" white noise we tested the nets' capabilities of distinguishing the "deterministic" from the "real" noise by presenting a superposition of both to relatively simple nets. In these experiments we also varied the number of parameters and the strength of "real" noise. One characteristic result from these experiments is shown in figures 4 and 5. The nets behave exactly as expected: the functional part of the data is extracted, while the noise is ignored. Though this experiment was set up to help understanding the complex questions involved in designing a net for time series analysis its results may also be interpreted as a nonstandard method of noise reduction. This is due to the fact that the noise reduction is not based on spectral

properties but rather on functional dependencies.
Although these first results are quite surprising they are still not more than preliminary. We are quite far from really understanding time series analysis with CN. Many parameters have to be adjusted — they should be derived from the data to be analysed rather than from empirical analysis of the nets' behaviour.

References

[1] K. Funahashi: Neural Networks 2(1989)183, K. Hornink et al.: Neural Networks 2(1989)359, H. White: Neural Networks 3(1990)535
[2] A. Lapedes, R. Farber: LA-UR87-2662, 1987
[3] A. Izenman: Math. Intelligencer 7(1985)27
[4] C. de Groot, D. Würtz: IPS Research Report No. 90-24, 1990

This work was partially supported by a PhD grant (CdG) given by the Swiss Bank Corporation.

Tab. 1: Performance of models on sunspot data. S/TAR: subset/threshold AR; BL: bilinear model; CN: connectionist net (see [4] for references). p: # parameters; $\hat{\sigma}^2$: residual variance of model; NAIC(')': AIC criterion; $\hat{\sigma}^2_{35/55}$: residual variance of 35 and 55 years 1 step ahead forecast; $\hat{\sigma}^2_F$: residual variance of 55 steps ahead forecast; –: figure too large due to numerical instability of model.

Model	p	$\hat{\sigma}^2$	NAIC(')	$\hat{\sigma}^2_{35}$	$\hat{\sigma}^2_{55}$	$\hat{\sigma}^2_F$
SAR(9)	4	203	5.4	214	286	1804
BL(9,0,8,6)	11	124	4.9	124	–	–
TAR(2,4,12)	19	154	5.0	148	238	1302
CNAR(4,4,1)	25	137	5.1	141	231	2016

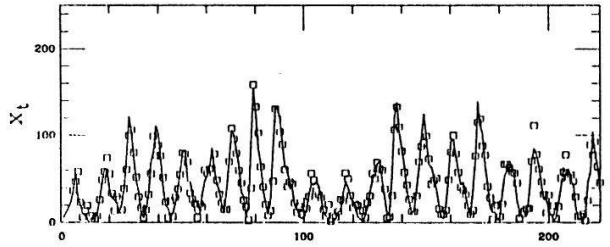

Figure 1: Estimation of sunspots activity time series on the basis of 221 data points: 1700–1920. The straight line connects the original, the squares indicate the estimated data points.

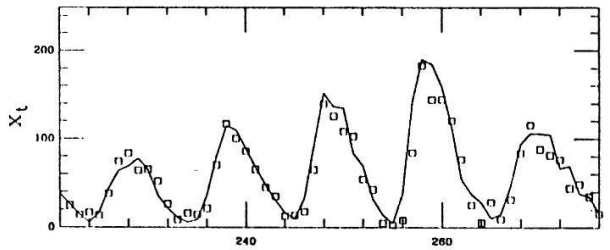

Figure 2: Forecasting 1 step ahead 35 and 55 points of the sunspot time series: 1921–1975.

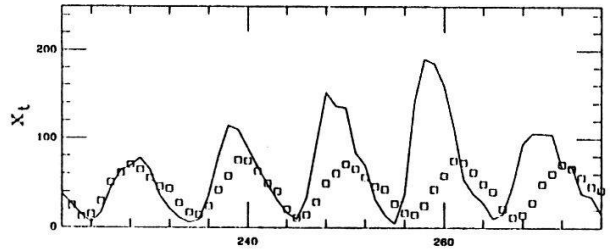

Figure 3: Forecasting 55 steps ahead of sunspot data: 1921–1975.

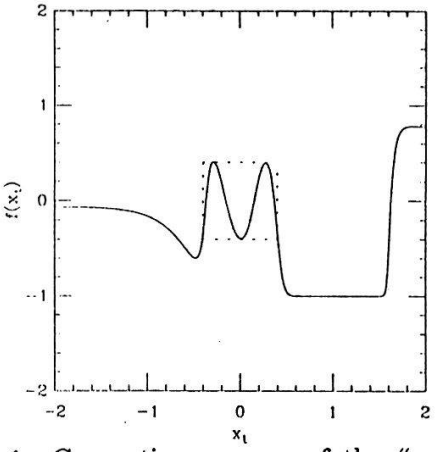

Figure 4: Generating process of the "noise free" logistic mapping.

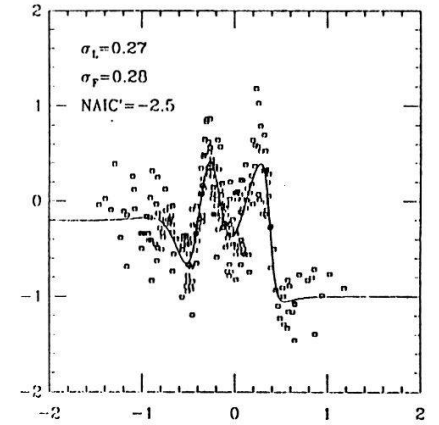

Figure 5: Estimation of the process in fig. 4 for white noise of strength $\sigma = 0.26$. The net has just enough parameters to fit the nonlinear mapping. The least square errors for the learning (L) and forecasting (F) process and NAIC' are given. The underlying structure is nicely recovered.

Convergence Properties for the Evaluation of Invariants from Finite Symbolic Substrings

R. Stoop °, J. Parisi †, and H. Brauchli °

° Institute for Mechanics, Federal Polytechnical University (ETH) of Zurich , CH-8001 Zurich, Switzerland

† Physics Institute, University of Zurich, CH-8001 Zurich, Switzerland

We examine how the scaling functions of fractal dimensions and Lyapunov exponents converge upon increasing the length of the finite substrings investigated. A traditional approach is compared with the more recent cycle expansion of periodic orbits.

Recently, the scaling behavior of a dissipative dynamical system has been elucidated by the help of a generalized entropy representing a function of two variables. In this way, it is possible to reflect the stability properties of the system under iteration of the dynamical map, on one hand, and the distribution of the probability measure on the attractor, on the other hand [1,2,3]. It has been shown that the more specific entropy function of the generalized dimension, $f(\alpha)$, and the analogous function for the Lyapunov exponents, $G_S(\varepsilon)$, can be recovered from the generalized entropy function as restrictions to one-dimensional lines [3].

In our contribution, we assume a three-scale Cantor set with a nontrivial grammar as an appropriate model for a dissipative dynamical system. For the symbols A, B, and C, the length scales and the associated probabilities are specified. Then it is required that a threefold repetition of symbol C cannot occur. Starting from the ensemble of all possible substrings of length n, we calculate the generalized entropy function. Therefrom, we derive the entropy functions $f(\alpha)$ and $G_S(\varepsilon)$, for different lengths n. One observes that, generally, the convergence towards the asymptotic scaling functions is oscillatory, due to the fact that different symbolic substrings could not yet be excluded at the given level n. Furthermore, the convergence is covered in part by the numerical inaccuracy of the computational tools. Nevertheless, it is possible to unveil the remaining invariant properties of the system.

The asymptotic behavior which, in this way, can be approximated for any hyperbolic experimental system is compared with the results obtained from a cycle expansion of periodic orbits [4,5,6]. For our model system, the latter provides exact results [7]. The numerical investigations prove evidence that the most important features of the model system are extractable by the more traditional approach. This indicates that the main problems arising in the evaluation of the scaling behavior of experimental dynamical systems derive from the fact that they are nonhyperbolic.

We believe that the present material makes evident the usefulness of the description of the scaling behavior of a dissipative dynamical system via the generalized entropy function. It, furthermore, demonstrates what changes can be expected, if a hierarchical discovery in the sense described above is being made. The application to nonhyperbolic maps is straightforward and has been worked out already [8,9]. For experimental systems, applications are expected in the future [10]. Finally, we would like to point out the fact that in these most recent developments not only the definition of a chaotic attractor as the closure of its unstable periodic orbits finds its inherent justification, but also a way has been found to incorporate in one representative function all the relevant information of the scaling behavior of a dissipative dynamical system.

References

[1] M. Kohmoto, Phys. Rev. **A37**, 1345 (1988).

[2] T. Tél, Z. Naturforsch. **43** a, 1154 (1988).

[3] R. Stoop and J. Parisi, Phys. Rev. **A43**, 1802 (1991).

[4] D. Ruelle, Statistical Mechanics, Thermodynamic Formalism (Addison-Wesley, Reading 1978).

[5] P. Cvitanović, in Nonlinear Physical Phenomena, Brasilia 1989 Winter School, A. Ferraz, F. Oliveira, and R. Osorio, eds. (World Scientific, Singapore, to be published).

[6] P. Cvitanović and B. Eckhardt, Phys. Rev. Lett. **63**, 823 (1989).

[7] R. Stoop, J. Parisi and H. Brauchli, Z. Naturforsch. a, to be published.

[8] R. Artuso, E. Aurell and P. Cvitanović, Nonlinearity **3**, 325 (1990).

[9] R. Artuso, E. Aurell and P. Cvitanović, Nonlinearity **3**, 361 (1990).

[10] R. Stoop and J. Parisi, work in preparation.